Optical control of individual nitrogen-vacancy centers in diamond

A dissertation presented
by

Emre Ismail Cengiz Togan

to
The School of Engineering and Applied Sciences
in partial fulfillment of the requirements
for the degree of
Doctor of Philosophy
in the subject of

Applied Physics

Harvard University
Cambridge, Massachusetts
December 2011

Thesis advisor

Mikhail D. Lukin

Author

Emre Ismail Cengiz Togan

Optical control of individual nitrogen-vacancy centers in diamond

Abstract

Individual nitrogen vacancy (NV) centers in diamond have recently emerged as a leading candidate for a building block for quantum information processing systems. Individual NV centers have many properties that are desirable for qubits. For example their spin states can be manipulated, initialized and measured even at room temperature. In order to build a quantum information processing system that consists of more than a single NV center, these individual NV centers have to be connected via quantum channels that distribute entanglement and allow quantum state transfer between NV centers. This thesis explores how the optical properties of the NV center can be used and manipulated to form these quantum channels. Likewise we show how the same properties can be used to better control the nuclear spin environment surrounding the NV center.

We first introduce, review and experimentally study the relevant optical properties of the NV center. These quantum optical techniques are then used to experimentally demonstrate spin-photon entanglement between the electronic spin of an individual NV center and a single photon. We next demonstrate quantum interference of two photons produced by NV centers in distinct diamond samples separated by two meters. These two demonstrations pave the way for entanglement generation, leading

to quantum channels, between remote NV centers.

Finally we demonstrate optical cooling, real-time measurement and conditional preparation of the nuclear spin environment around an NV center using all-optical manipulation of its electronic spin. This technique can lead to better control of individual NV centers and thus more robust quantum information processing systems.

Contents

Title Page i
Abstract iii
Table of Contents v
Citations to Previously Published Work viii
Acknowledgments ix
Dedication xii

1 Introduction **1**
1.1 Background 1
1.2 Overview 5
1.2.1 Basic properties 5
1.2.2 Spin-Photon entanglement 6
1.2.3 Indistinguishable single photons from separate NV centers . . 7
1.2.4 All-optical measurement and cooling of the nuclear spin environment of an NV center 8

2 Low temperature optical properties of the NV center in diamond **9**
2.1 Introduction 9
2.2 Basic experimental techniques for isolating single NV centers 13
2.3 A model for the *ae* triplets (orbital excited state) of the NV center . . 16
2.3.1 Electronic states of the NV center 16
2.3.2 Properties of optical transitions 20
2.3.3 The effect of strain 21
2.3.4 Spin-spin interaction and effects of magnetic fields 24
2.4 Absorption spectroscopy 25
2.5 Fluorescence timetraces 29
2.5.1 Applications to ground state spin detection 33
2.6 Rabi oscillations between ground and excited states 35
2.7 Modifying optical properties: electric field tuning of NV centers . . . 37
2.8 Electric environment of NV centers 42
2.8.1 Charge environment under resonant excitation 43

2.8.2 Charge environment under green excitation 46
2.9 Ionization 48

3 Quantum entanglement between an optical photon and a solid-state spin qubit 52
3.1 Introduction 52
3.2 Characterization of NV centers 54
3.3 Experimental demonstration of spin-photon entanglement 57
3.4 Conclusions and outlook 63

4 Quantum interference of single photons from remote nitrogen-vacancy centers in diamond 64
4.1 Introduction 64
4.2 Identical photons from two NV centers 67
4.3 Demonstration of HOM interference from two NV centers 70
4.4 Conclusions and outlook 74

5 Laser cooling and real-time measurement of nuclear spin environment of a solid-state qubit 76
5.1 Introduction 76
5.2 Coherent population trapping with NV centers 78
5.3 Optical cooling and conditional preparation of ^{14}N nuclear spin states 81
5.4 Observation of instantenous Overhauser field from the ^{13}C spin bath . 84
5.5 Measurement-based preparation of ^{13}C spin bath 86
5.6 Conclusions and outlook 90

6 Conclusion and Outlook 92

A Supporting material for Chapter 3 97
A.1 Calculation of entanglement fidelity 97
A.2 Supplementary methods 98
A.2.1 Overview of experimental setup 98
A.2.2 Optical setup 100
A.2.3 Microwave control 101
A.2.4 Experiment control and data acquisition 103
A.3 Spin readout 104
A.4 Verification of polarization selection rules for $|A_2\rangle$ state 111
A.5 Effects of magnetic environment, detunings, and echo 114
A.5.1 Effect of Finite Detuning 115
A.5.2 Spin Echo Sequence 116
A.6 Fidelity estimates 117
A.6.1 Time bin optimization 118
A.6.2 Maximum Likelihood Estimate 119

B Supporting material for Chapter 5 **125**
B.1 Experimental details 125
B.1.1 Sample description 125
B.1.2 Experimental setup 126
B.1.3 Effects of ionization and other forms of spectral drift 127
B.2 Multilevel description of the NV center 128
B.3 Measurement of branching ratios 132
B.4 ^{14}N polarization via optical pumping and measurement based preparation 133
B.4.1 Optical Pumping 133
B.4.2 Details of measurement based preparation 135
B.5 Strain dependence of CPT width 136
B.6 Autocorrelation measurements and spectral density of signal 140
B.7 Nuclear configuration measurements using fast magnetic field ramps . 142
B.8 B_{prep} dependence of the observed width 145
B.9 Lifetime in the absence of optical fields 148
B.10 Discussion 149

Bibliography **152**

Citations to Previously Published Work

Parts of Chapter 2 have have appeared as the supplementary information to the following two papers:

> "Quantum entanglement between an optical photon and a solid-state spin qubit", E. Togan, Y. Chu, A. S. Trifonov, L. Jiang, J. Maze, L. Childress, M. V. G. Dutt, A. S. Sørensen, P. R. Hemmer, A. S. Zibrov & M. D. Lukin Nature **466**, 730734 (2010);
>
> "Laser cooling and real-time measurement of the nuclear spin environment of a solid-state qubit", E. Togan, Y. Chu, A. Imamoglu & M. D. Lukin, Nature **478**, 497501 (2011).

Chapter 3, in its entirety, has been published as

> "Quantum entanglement between an optical photon and a solid-state spin qubit", E. Togan, Y. Chu, A. S. Trifonov, L. Jiang, J. Maze, L. Childress, M. V. G. Dutt, A. S. Sørensen, P. R. Hemmer, A. S. Zibrov & M. D. Lukin Nature **466**, 730734 (2010).

And Chapter 5 appears, in its entirety, as

> "Laser cooling and real-time measurement of the nuclear spin environment of a solid-state qubit", E. Togan, Y. Chu, A. Imamoglu & M. D. Lukin, Nature **478**, 497501 (2011).

Acknowledgments

I'd like to begin by thanking my advisor, Mikhail Lukin, for continuous support, encouragement and patience over the years. His deep knowledge of many fields, intuition and creativity have been a great resource. I feel very lucky to have had him as my advisor.

I was fortunate to have had help from other faculty members both at Harvard and elsewhere. I'd like to thank Fedor Jelezko in particular for helping to get our cryogenic experiments running, and him and Jorg Wrachtrup for sharing their pioneering techniques, and their understanding of the NV centers. Phil Hemmer contributed many useful comments and suggestions that both helped shape the experiments as well as my knowledge of NV centers. It was a great pleasure to work with Atac Imamoglu, from whom I learned a lot even in a very short interaction in Zurich, and he helped to shape the research of the work presented in Chapter 5. Vincent Jacques provided both experimental help, as well as inspiration and ideas for projects that lead to a much better understanding of the NV center, and it was a great pleasure to work with him. I'd also like to thank John Doyle who allowed us to use the space in his labs where a majority of the experimental work presented in this thesis was carried out. Finally I'd like to thank Mikhail Lukin, Federico Capasso, Marko Loncar, and Markus Greiner for being on my committee.

The work presented in this thesis would not have been possible were it not for the extremely talented colleagues whom I had the opportunity to work with. When I started, I was fortunate to work with Gurudev Dutt and Lily Childress. I've learned a lot from both of them and their excellent work made much of what is presented in this thesis possible. Yiwen Chu has played a vital role in all of the work presented

in this thesis. She shared equally the execution of the spin-photon entanglement and coherent population trapping experiments. It was a privilege to have worked with her. I'm grateful to Alexei Trifonov for his great work and sharing his experiences and knowledge. I had the chance to work with Alex Kubanek, Micheal Goldman, and Alp Sipahigil during my last year at Harvard and the experience has been most enjoyable. I'd like to thank them for all their hard work and support.

A close collaboration with many theorists was essential to the success of the work presented in this thesis. In particular I learned a lot from colloborating with Liang Jiang, Michael Gullans, and Adi Pick. I single out Jero Maze who's understanding of the NV center and group theory shaped much of the work presented in this thesis, and it was a pleasure to have worked with him.

I'd like to thank all the members of the Lukin group and the diamond community at and around Harvard in general whom I've had many useful and stimulating discussions over the years and from whom I've recieved much experimental help: Michal Bajcsy, Sasha Zibrov, Jake Taylor, Darrick Chang, Mohammad Hafezi, Vlatko Balic, Philip Walther, Alexey Gorshkov, Matt Eisaman, Jeff Thompson, Liang Jiang, Alexey Akimov, Tommaso Calarco, Anders Sorensen, Ana Maria Rey, Paola Cappellaro, Jonathan Hodges, Philip Walther, Mughees Khan, Sebastian Hofferberth, Peter Rabl, Brendan Shields, Sahand Hormoz, Alex Nemiroski, Aryesh Mukherjee, Peter Maurer, Garry Goldstein, Dirk Englund, Frank Koppens, Shimon Kolkowitz, Norman Yao, Ania Jayich, Nicholas Chisholm, Georg Kucsko, Christian Latta, Quirin Unterreithmeier, Igor Lovchinsky, Alex Sushkov, Tobies Tiecke, Nathalie de Leon, Steve Bennett, Tom Babinec, Birgit Haussmann, Jenn Choy, Patrick Maletinsky, Sungkun

Hong, David Glenn, David Le Sage, My Linh Pham, Paul Stanwix, and Nir Bar-Gill. I'd like to thank Irfan Bulu in particular who very patiently taught me many interesting aspects of nanophotonics.

The experiments benefited greatly from custom machined parts made by Stan Cotreau and the staff at the Scientific Machine Shop led by Louis Defeo. Much of the custom electronics we used for the experiments were developed by Jim MacArthur, who I'd like to thank for being both very patient and resourceful.

The help and support of family and friends was essential to completing this thesis. I'd especially like to thank my parents for their continued support and understanding. This thesis is dedicated to them.

To my parents.

Chapter 1

Introduction

1.1 Background

Techniques for isolation and control of individual quantum systems have recently received considerable interest. These techniques have useful applications in different fields such as metrology[1], fundamental tests of quantum mechanics[2] as well as quantum information[3].

Atomic systems, including individual neutral atoms and individual charged ions, exhibit exceptional controllability of their internal and external degrees of freedom. The properties of their internal states, for example hyperfine sub-levels, and how these internal states interact with the environment are well understood. Moreover standard techniques, using microwave or optical fields, are available to manipulate these internal states [4, 5, 6, 7]. These states can also exhibit exceptionally long coherence times[8] since they can be decoupled from their environment. Numerous techniques are available to control the motional states of atomic systems, for example

ideas of laser cooling or trapping have been developed in this context[9, 10, 11]. Using these techniques individual neutral atoms or ions can be isolated and trapped. Experiments with single neutral atoms or ions have lead to interesting demonstrations ranging from high sensitivity measurements of forces[12] and frequency shifts due to relativity[13], to using these individual systems as qubits for quantum information processing[14, 15].

Interactions between separate, individual atomic systems can be realized by coupling their internal degrees of freedom to common degrees of freedom, such as coupled motional states of several trapped ions. The use of such interactions have lead to demonstrations of multi-particle entanglement[16, 17] in trapped ions. Furthermore, macroscopically separated quantum systems can be entangled using light emitted by these individual systems. In particular, protocols that rely on the detection of a probabilistic event that "heralds" the entanglement of the separate matter qubits[18] have been developed. These protocols have lead to demonstrations of remote quantum entanglement between separate matter qubits[19], bell state violation[2] and teleportation[20].

Combining the exceptional ability to control individual quantum systems with the ability to entangle such systems with high fidelity is a prerequisite for achieving large-scale quantum information processing systems[3, 14, 15]. With the recent set of proof-of-principle experiments, building a large-scale quantum information processing system appears to be within reach with atomic systems. However practical challenges remain in scaling the current proof of principle demonstrations to even larger number of qubits. One of the major challenges is maintaining the long coherence times and

high gate fidelities of earlier demonstrations while controlling the motional degrees of freedom for a larger number of single ions or neutral atoms. For example for scalable architectures with ion traps using miniaturized electrodes, the uncontrolled electric noise at the electrodes causes significant heating of the ions[21], this heating significantly decreases the achievable gate fidelities. One might imagine that some parts of the complexity can be circumvented by taking advantage of solid state systems. For example for defects localized within solid crystals, no additional trapping is necessary once the host crystal is well localized.

Solid state systems are also attractive since, the interaction between nearby quantum systems can be quite large as the solid state systems can be densely packed. For practical applications this allows direct coupling of two separate quantum systems, for example via electric or magnetic dipole-dipole interaction. Unfortunately a solid-state system also interacts strongly with its complex environment, leading to decoherence and generally short coherence times. In fact understanding, engineering, and controlling the interaction of individual solid-state quantum systems with their environment is a very active research area and the main challenge in utilizing solid-state systems for large-scale quantum information processing. As an example of the rapid progress in this area the coherence times of superconducting charge qubits have improved from ns[22] to μs[23] in the past ten years, and most recently to 10s of μs[24] by careful environment and system engineering.

Another advantage of solid-state systems is that advanced nano-fabrication techniques can be applied to control the local environment around a solid-state quantum system. These techniques can controllably change the properties of the solid-state

system. In addition, these techniques, can be used to integrate solid-state quantum systems with external microfabricated structures, for example high Q microwave or optical resonators that are strongly coupled to the solid-state system.

There are many different solid-state systems that can be addressed and isolated individually. These range from the superconducting charge qubits mentioned earlier to donor bound impurities in semiconductors (e.g. [25]). Of the many solid-state systems available this thesis will focus on the negatively charged nitrogen vacancy center in diamond (commonly abbreviated as NV center).

The NV center is an exceptional color center. It has an electronic triplet as a ground state[26]. Hence, electronic spin sub-levels in the ground state can be used as long lived internal states, with coherence times as long as milliseconds[27]. What is exceptional about the NV center is that it has many optical properties that allow for coupling and manipulation of spin degrees of freedom with light. For example, the spin-states of the NV center can be polarized even at room temperature by exciting the NV centers with green light[28]. By working at cryogenic temperatures, individual optical transitions become accessible, and these transitions are closely linked with spin degrees of freedom. Thus the NV center combines many of the advantages of a solid-state system with many similar properties of the atomic systems considered earlier. For example, the optical pumping of the internal spin sub-levels achievable with green light is very similar to the optical pumping of hyperfine sub-levels available in individual ions. It is thus an ideal system for applying some of the concepts developed in the AMO physics community in the solid state.

This thesis focuses on experimental control and manipulation of NV centers in

diamond with the goal of using them in potential applications in quantum information processing. To this end we will take advantage of the optical properties of NV centers at cryogenic temperatures and some of the concepts traditionally used with atomic systems.

1.2 Overview

This thesis consists of three experimental projects each presented in its own chapter, these follow an introductory chapter.

Chapter 2 of this thesis introduces and reviews the basic optical properties of the NV center as well as some basic experimental techniques. Chapter 3 demonstrates entanglement between individual spin states of an NV center and polarization states of a single photon. Chapter 4 demonstrates that photons emitted from separate NV centers can be indistinguishable. Chapter 5 demonstrates how the magnetic nuclear environment around an NV center can be manipulated, measured in real-time, and cooled into desired states using all-optical methods.

1.2.1 Basic properties

Chapter 2 serves as an introduction and a review of the optical properties of the NV center relevant to manipulating and utilizing individual transitions from the NV center's ground states to its orbital excited states. In exploring how the NV center interacts with light fields, the effect of the light field on the environment and charge state of the NV center must also be considered. Chapter 2 introduces basic experimental methods as well as a group-theory based theoretical model for the NV

center's optical transitions between the ground and excited states. The key prediction of the model explains the variation of the optical properties for individual transitions from NV center to NV center, and this is experimentally studied. It is shown that by using the Stark effect one can alleviate the variation between NV centers. The sensitivity to electric fields imply that the uncontrolled electric fields from the charge environment around the NV center also affect the the optical properties, in particular the linewidth of transitions are broadened. This broadening is found to be affected by the light fields that are used to excite the NV center. Finally it is found that the light fields also effect the charge state of the NV center leading to ionization. The properties and models explored in Chapter 2 form the basis for the remaining chapters of this thesis.

1.2.2 Spin-Photon entanglement

The optical properties discussed in the previous chapter lead to a natural way in which single photons can be entangled with long-lived spin states of the NV center. Quantum entanglement is among the most fascinating aspects of quantum theory[3]. Entangled optical photons are now widely used for fundamental tests of quantum mechanics[29] and applications such as quantum cryptography[3]. Several recent experiments demonstrated entanglement of optical photons with trapped ions[30], atoms[31, 32], and atomic ensembles[33, 34, 35], which are then used to connect remote long-term memory nodes in distributed quantum networks[36, 37, 19]. In Chapter 3, we report on realization of quantum entanglement between the polarization of a single optical photon and a solid-state qubit associated with the single electronic

spin of a nitrogen-vacancy center in diamond. Our experimental entanglement verification uses the quantum eraser technique[38, 32]. This new entanglement source can be used in studies of fundamental quantum phenomena and provides a key building block for the solid-state realization of quantum optical networks[39, 40].

1.2.3 Indistinguishable single photons from separate NV centers

The key to building larger quantum optical networks using macroscopically separated NV centers relies on spin-photon entanglement and the ability to obtain indistinguishable single photons from separate NV centers. The interference of two identical photons impinging on a beam splitter leads to perfect photon coalescence where both photons leave through the same output port. This famous effect, known as Hong-Ou-Mandel (HOM) interference[41] can be used to characterize the properties of quantum emitters with high accuracy. This is a particularly useful tool for quantum emitters embedded in a solid state matrix like the NV center because their internal properties, unlike those of atoms in free space, differ substantially from emitter to emitter due to interactions with their environment, particularly the local strain.

In this chapter we demonstrate HOM interference of photons emitted from two single NV centers in diamond that are spatially separated by 2 meters. The frequencies of the photons are controlled by tuning individual optical transitions of associated NV centers via a DC electric field.

1.2.4 All-optical measurement and cooling of the nuclear spin environment of an NV center

While the two previous chapters focused on exploring how the light field emitted by NV centers can be used to build larger scale quantum networks, this chapter focuses on how we can take advantage of the interaction of the NV center's spin degrees of freedom with light fields to better control the NV center and its magnetic environment. Control over quantum dynamics of open systems is among the central challenges in quantum science and engineering. Coherent optical techniques, such as dark resonances associated with Coherent Population Trapping (CPT)[6, 42], are widely used to control quantum states of isolated atoms and ions. In conjunction with spontaneous emission, they allow for laser cooling of atomic motion[43], preparation and manipulation of atomic states[44], and rapid quantum-optical measurements that are essential for applications in metrology[45, 46, 47]. In Chapter 5, we demonstrate that these techniques can be applied to control individual atom-like impurities in solid state and their local environment[48, 49, 50, 51]. Using all-optical manipulation of the electronic spin of an individual Nitrogen-Vacancy (NV) color center in diamond, we demonstrate optical cooling, real-time measurement, and conditional preparation of its nuclear spin environment. These methods enable potential applications ranging from all-optical nano-magnetometry to quantum feedback control of solid state qubits, and may lead to new approaches for quantum information storage and processing.

Chapter 2

Low temperature optical properties of the NV center in diamond

2.1 Introduction

The NV center is a defect in diamond that plays a central role in this thesis. NV centers have been proposed as building blocks for room-temperature quantum computers[52], sensitive magnetic[53, 54, 55] and electric field sensors[56], single photon-sources[57], in-vivo markers for biological cells[58]. These widely different goals are achievable with a single system as the NV center exhibits many unique properties.

In particular, the host material (diamond), that houses the NV center is a wide-bandgap material that has excellent chemical inertness, high thermal conductivity, and is one of the hardest materials on earth[59]. These properties imply an optical transparency over a wide range of wavelengths and an ideal material to base many

solid-state technologies that will be robust in deployment, whether it is inside a cell or as a quantum repeater in a telecommunications system. The fact that diamond can be grown using techniques like CVD with controllable density of nitrogen impurities and NV centers (see e.g. commercially available diamonds from [60]) also means that NV center-based technologies can in principle be fabricated in large numbers. These excellent properties of bulk diamond extends to nano diamonds, where stable emission from single NV centers have been demonstrated in pieces of nano-diamond small as 4 nm in radius[61].

Of the many color centers in diamond[62] the negatively charged NV center has many desirable properties for various applications ranging from single photon sources to biological markers. The NV center's strong optical transition, and the fact NV centers can be individually isolated using standard confocal microscopy techniques make it an ideal single-photon source[57, 63]. Due to the stability of its charge state and charge environment, under continuous excitation the NV center does not exhibit long term blinking or bleaching at room temperature[64]. This photo-stability lead to development of commercial products using NV centers as a single photon sources (see products under [65]). Motivated by the photo-stability and the potential ability to functionalize diamond, NV centers embedded in nanodiamonds have been used as biological markers in live cells[58, 66] and model organisms[67].

The NV center also exhibits phenomenal spin properties even at room temperature. The ground state of the NV center is a spin triplet which has a 2.87 GHz zero field splitting[63, 26]. The triplet spin state can be turned into a pseudo-spin 1/2 system by application of a small magnetic field. By applying a microwave field resonant

with the magnetic dipole allowed transitions within the triplet one can coherently manipulate the single electronic spin associated with the NV center[68], which allows for studies of its coherence properties. The coherence time is limited by the interactions with its magnetic environment. In pure samples, where the magnetic environment is formed by the nuclear spin bath due to 1.1 % ^{13}C concentration, long coherence times ($T_2 \geq 300\,\mu$s) have been demonstrated (for a recent systematic study see [69]). By careful materials engineering, the electronic and nuclear impurities can be decreased. In isotopically purified low defect concentration CVD diamonds coherence times up to $\sim$ 2 ms have been demonstrated[27]. Due to the ease of manipulation and long coherence times, the NV center has been proposed as a qubit candidate.

The magnetic environment can also be used as an advantage. In particular, in samples where the decoherence is limited by the nuclear spins, the interaction of the proximal nuclear spins with the electronic spin can be much greater than the associated decoherence times[70, 71]. The control over the electronic spin can then be extended to these few strongly coupled nuclear spins[68, 72, 73, 74, 75]. The nuclear spins, because of their smaller magnetic dipole moment, interact less with their magnetic environment and hence have longer coherence times. They make ideal systems for storage of quantum information.

For practical applications, the close connection between the optical transitions and the spin states of the NV center is really the key feature that differentiates NV centers from other defect centers. Even though the NV center has an intricate excited level structure and particular selection rules for optical transitions allowed between the ground and excited states, this level structure is inaccessible with optical excitation

directly at room temperatures[76, 77]. In fact room temperature experiments take advantage of the strong vibronic side-bands of the NV center[78] to excite NV centers into their orbital excited states. Even though individual transitions are not accessible a close connection between the spin structure and optical excitation still exists. In particular, 532 nm light that excites the NV center unconditional of the ground state, leads to spin polarization of the defect via decay into the meta-stable singlet and preferential decay from the singlet to the $m_s = 0$ ground state[79]. The same mechanism is also responsible for a transient difference in the fluorescence intensity dependent on the initial spin state. This difference then provides a convenient method to measure the initial spin state at room temperature.

This close connection between the optical transitions and spin properties of the NV center improve even further by working with NV centers at cryogenic temperatures. The effects of the fluctuations of the charge environment and the broadening due to phonon processes can be suppressed[80] by going to lower temperatures. Thus, at temperatures below 20 K, coherent driving of specific optical transitions between the ground state and the optically excited states become possible[81, 82]. These optical transitions then allow for interfacing between the phenomenal spin properties of the NV center and optical fields. In doing so techniques established in the AMO community can be used. Not only does the application of these well established tools enable experiments previously only possible with atomic systems (Chapters 3 and 4), but has additional interesting properties due to the solid state environment (Chapter 5).

This chapter provides a review of the basic properties of low temperature optical

transitions between the ground state triplet and the orbitally excited state triplets as well as introducing simple experimental methods for verifying and modifying these properties. First, an experimental apparatus is presented, that will be used to explore the optical properties of the NV center, and general properties of the emission and absorption of light from the NV center will be discussed. Then a model is introduced which forms the basis of all of the work in this thesis, and different levels and transitions are introduced. This is followed by demonstration of simple optical techniques where the model is verified. Some simple applications, where appropriate, of the experimental techniques are also provided. A mechanism based on the Stark effect for controlling the individual properties of the NV center is provided, and a discussion of the effect of the uncontrolled electrical environment follows. Finally a short section reviews how the optical excitation changes the charge state of the NV center that is relevant for low temperature NV center related experiments.

2.2 Basic experimental techniques for isolating single NV centers

A home-built confocal microscope with the diamond sample in a cryogenic environment forms the basic experimental apparatus for most of the work presented in this thesis. Details of the confocal microscope, widely used to study single fluorescent emitters, have been applied to working with NV centers by many groups. Hence a rough description of the experimental apparatus will be provided for completeness

here[1].

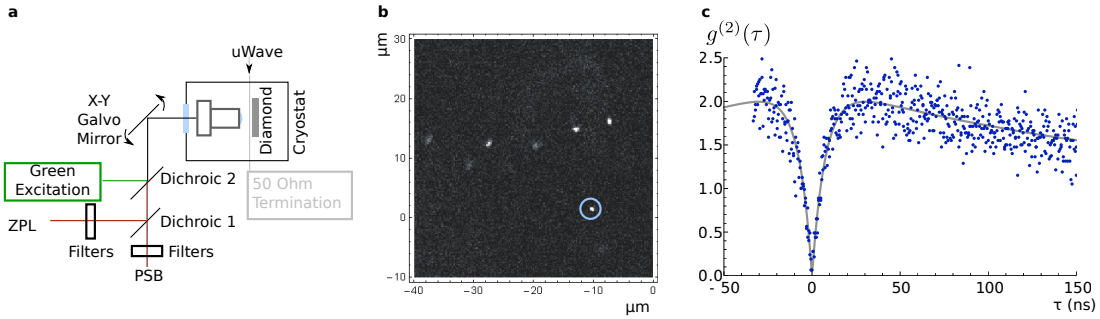

Figure 2.1: Confocal microscopy and isolation of single NV centers. **a**. Simplified schematic optical setup. The diamond sample housing NV centers is kept at low temperature (< 10 K) by an ST-500 (Janis) helium flow cryostat. Microwaves are brought in close proximity to NV centers using a 15 μm copper wire that stretches across the diamond. A high NA objective, kept in vacuum, is used to individually address NV centers and optical access is through a window on the vacuum chamber. The X-Y galvo in the Fourier plane allows for raster scanning of the focus at the image plane. Different spectral beams are spatially overlapped with dichroic filters, and additional filters are used to further spectrally isolate each channel. Green excitation is accomplished using a green laser that is modulated with an AOM. Phonon Side Band (PSB) channel is either directly connected to an APD via a single mode fiber or via a single mode fiber-beam splitter to two APDs forming a Hanbury Brown-Twiss (HBT) setup, which allows us to infer the autocorrelation of the collected light from an NV center. Zero Phonon Line (ZPL) channel is used either for resonant excitation or collection in the ZPL (see text for details). **b**. A typical confocal image of a high purity synthetic IIa diamond (electronic grade from E6). False color scale ranges from 0 counts per second (black) to 25000 counts per second (white). Each of the localized bright spots is an NV center. **c**. Measurement of the autocorrelation of light in the PSB ($g^{(2)}(\tau)$) of the NV center in light-blue circle in b. The measured data (blue dots) show clear anti-bunching behavior at zero time delay. The gray curve is a fit to a three level model[57].

An NV center can be excited using a wide range of excitation wavelengths[78] due to a strong vibronic side-band in excitation. In particular, shining a green (532 nm doubled-YAG) laser leads to excitation of the NV centers from the ground state to the vibronic states which quickly decay to the orbital excited state. The resulting

[1]For more details and particular equipment used see Appendix A.

fluorescence when the orbital excited state decays can be spectrally isolated and sent to single photon counting avalanche photo diodes (APDs). By using a high NA microscope objective, the excitation laser can be focused to a spot whose size is on the order of the wavelength cubed, and emission from the same volume can be collected. Figure 2.1b shows a typical false-color plot of the collected fluorescence intensity when the excitation and collection focal spots are raster scanned with a galvo mirror. Each of the bright spots is an NV center, and the density is typical for high purity (Electronic Grade) synthetic diamonds commercially available[60]. A measurement of the inferred autocorrelation of the light emitted from one of the spots shows the typical anti-bunching expected from single photon emitters (Figure 2.1c).

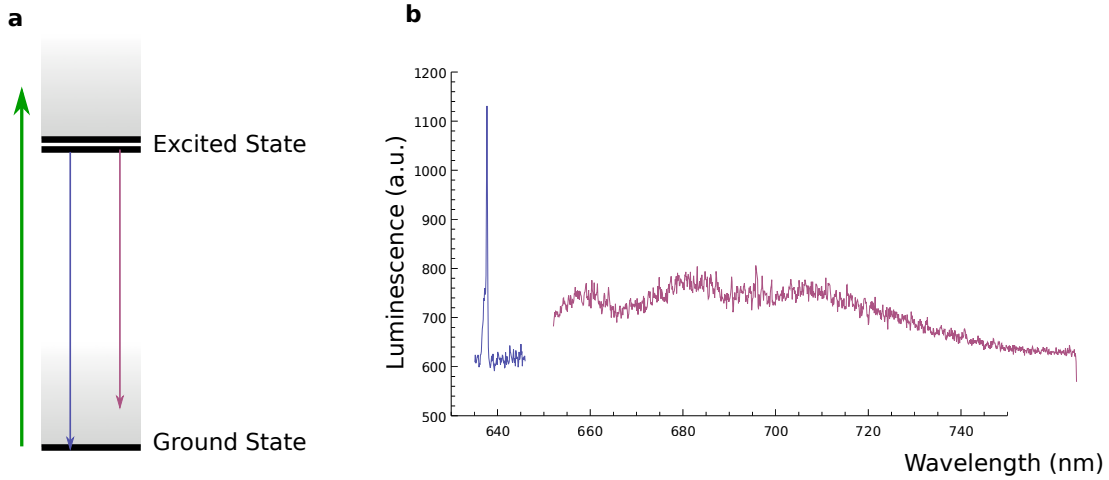

Figure 2.2: Optical emission from a single NV center under CW green illumination. **a**. Simplified schematic of the relevant transitions. Emission into the ZPL (blue arrow) and PSB (red arrow) are separated using dichroic and spectral band-pass filters (see Figure 2.1). Vibronic levels are indicated by gray gradients. **b**. A typical emission spectrum from a single NV center measured on a spectrometer. Blue shows the emission into the ZPL channel and red shows the emission into the PSB channel measured separately. Region which is affected by the spectral filters (647-653 nm) has been removed.

The low temperature emission spectrum from one of these NV centers is shown in

Figure 2.2, and indicates the existence of Zero-Phonon-Line (ZPL) and the wide-band Phonon-Side-Band (PSB), where 96 % of the emission is to the PSB. The names are used to indicate that emission of photons in PSB are accompanied by phonon emission while no phonons are emitted in the ZPL. The wide-band emission from the PSB has the advantages that it can be easily spectrally isolated from excitation lasers and it provides a distinct signature of NV center's emission and its charge state. In particular, we will take advantage of the PSB and collect fluorescence while exciting the NV center resonantly on the ZPL. But for most of this work we will be concerned with the properties of the ZPL. To explore the structure within the ZPL we next explore a group-theory based model of the orbital excited states.

2.3 A model for the ae triplets (orbital excited state) of the NV center

Using group theory and the C_{3v} symmetry of the potential associated with the NV center powerful predictions about the level structure of an NV center can be made. For this section we follow the main results presented in a recent publication[83] that are relevant to the orbital excited states of the NV center. This model forms the theoretical basis for all of the experimental work that was carried out in this thesis.

2.3.1 Electronic states of the NV center

The negatively-charged NV defect has six electrons, two from the nitrogen, three from the three carbons surrounding the vacancy, and one from the environment.

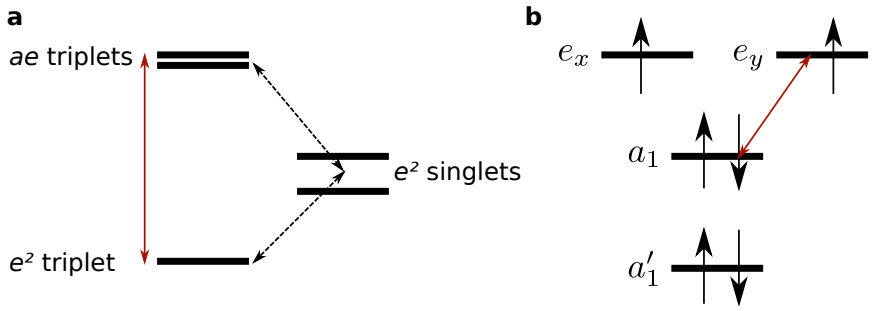

Figure 2.3: Sketch of the relevant levels and transitions for the NV center. **a**. Optical transitions linking the ground state (e^2 triplet) to excited state (ae triplets) are shown in red (identical to Figure 2.2 blue arrow). Non-radiative transitions to the e^2 singlets shown in dashed arrows. **b**. Schematic diagram of relative energies of the different orbital levels and their occupancy for one possible configuration of the e^2 triplet. The red arrow indicates an optical transition to the ae triplet (analogous to the red arrow in (a)).

They occupy the orbitals a_1', a_1, e_x, e_y whose symmetries are imposed by the nuclear potential. These orbitals transform as the irreducible representations of the C_{3v} group and have been extensively used by many authors[84, 85, 86, 71]. A cartoon of the relative ordering of these orbitals are shown in Figure 2.3 b. The a_1' and a_1 are lowest in energy and for the ground state are therefore filled by four of these electrons. The remaining two electrons occupy the degenerate orbitals e_x and e_y. The orbitals e_x and e_y can be viewed as p-type orbitals and $e_+ = -e_x - ie_y$, $e_- = e_x - ie_y$ are analogous to p states with definite orbital angular momentum. Lowest occupation energy of these orbitals give rise to the triplet ground state

$$\left|{}^3A_2\right\rangle = |E_0\rangle \otimes \begin{cases} |+1\rangle \\ |0\rangle \\ |-1\rangle \end{cases} \tag{2.1}$$

where $|\pm 1\rangle, |0\rangle$ correspond to the $m_s = \pm 1, 0$ states, respectively. $|E_0\rangle = |e_x e_y - e_y e_x\rangle$, refers to the orbital state with 0 orbital angular momentum projection along the NV

axis. A_2 denotes the orbital symmetry of the state, which is determined by the symmetries of the e_x and e_y orbitals. Note that this state can be modeled with two holes in each of the orbital e states, so we will call the ground state triplet the e^2 triplet. From now on we will refer to the different spin sub-levels of the e^2 triplet with their m_s quantum numbers, i.e. $|\pm 1\rangle$ and $|0\rangle$ for $m_s = \pm 1$ and $m_s = 0$.

The relevant excited state for the optical transitions in the ZPL is another pair of triplets which arises from the promotion of one of the electrons occupying the orbital a_1 to the e_x or e_y orbitals [85] (illustrated by red arrow in Figure 2.3). In the two hole picture this state can be modeled by one hole in the orbital e and another hole in the orbital a_1, i.e. a triplet in the ae electronic configuration. A total of six states can be formed in this configuration and their symmetries are determined by a group theoretical analysis[83],

$$\begin{aligned}
|A_1\rangle &= |E_-\rangle \otimes |+1\rangle - |E_+\rangle \otimes |-1\rangle \\
|A_2\rangle &= |E_-\rangle \otimes |+1\rangle + |E_+\rangle \otimes |-1\rangle \\
|E_x\rangle &= |X\rangle \otimes |0\rangle \\
|E_y\rangle &= |Y\rangle \otimes |0\rangle \\
|E_1\rangle &= |E_-\rangle \otimes |-1\rangle - |E_+\rangle \otimes |+1\rangle \\
|E_2\rangle &= |E_-\rangle \otimes |-1\rangle + |E_+\rangle \otimes |+1\rangle
\end{aligned} \tag{2.2}$$

where we have named the first four states as A_1, A_2, E_x and E_y according to their symmetries and named the last two states as E_1 and E_2 since they also transform according to the irreducible representation E. Here, $|E_\pm\rangle = |ae_\pm - e_\pm a\rangle$ and $|X(Y)\rangle = \left|ae_{x(y)} - e_{x(y)}a\right\rangle$.

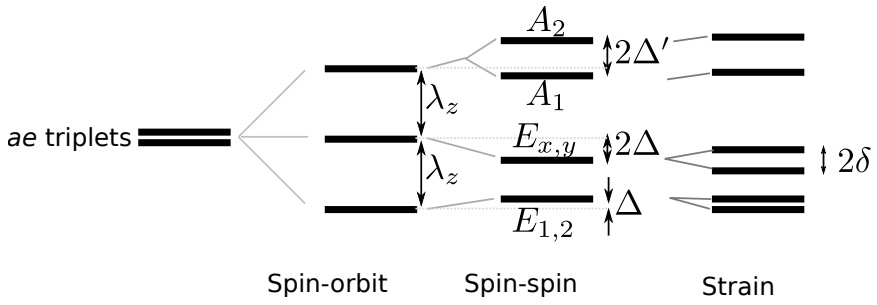

Figure 2.4: Hierarchy of interactions for *ae* triplets, typical for a low-strain NV center. Six states (see text) are split under spin-orbit ($\lambda_z \sim 5.5$ GHz), spin-spin ($\Delta \sim \frac{1}{3}1.42$ GHz and $\Delta' \sim 3.3$ GHz) and small non-axial strain (δ) leading to six individual, separately addressable levels.

As spin-spin and spin-orbit interactions are invariant under any operation of the C_{3v} group, the states given in equation (2.2) are eigenstates of the full Hamiltonian including these interactions in the absence of any perturbation such as magnetic field, crystal strain and/or electric field. Consider the following Hamiltonian for the excited state manifold:

$$H = H_{ss} + H_{so} + H_{strain} \tag{2.3}$$

where the spin-orbit and spin-spin [86, 87, 83] Hamiltonians are given by

$$H_{so} = \lambda_z S_z L_z + \lambda_\perp (LS)_\perp \tag{2.4}$$

$$\begin{aligned} H_{ss} = {} & \Delta \left(|A_1\rangle\langle A_1| + |A_2\rangle\langle A_2| + |E_1\rangle\langle E_1| + |E_2\rangle\langle E_2| \right) \\ & -2\Delta \left(|E_x\rangle\langle E_x| + |E_y\rangle\langle E_y| \right) + \Delta' \left(|A_2\rangle\langle A_2| - |A_1\rangle\langle A_1| \right) + H'_{ss} \end{aligned} \tag{2.5}$$

where L and S are the orbital angular momentum and spin operators,$3\Delta \approx 1.42$ GHz and $\Delta' \approx 1.55$ GHz characterize the spin-spin induced zero-field splittings, $\lambda_z \approx 5.5$ GHz is the axial spin-orbit interaction, and $\lambda_\perp$ is the non-axial spin-orbit interaction. The term H'_{ss} leads to mixing between the states with E symmetry, since its small

it will initially be ignored. Initially we will also ignore the H_{strain} term. Figure 2.4 illustrates the typical strengths and effects of the various interactions in H for the states considered.

In summary in the absence of any external fields (strain, magnetic, electric), the six levels in the *ae* triplets can be categorized in two groups. First group consists of two degenerate states ($|E_x\rangle$, $|E_y\rangle$) that have 0 electronic spin projection along the NV axis. The second group consists of 4 levels that are entangled states of orbital angular momentum and spin. Two of these states ($|E_1\rangle$, $|E_2\rangle$) are degenerate, while the remaining two ($|A_2\rangle$, $|A_1\rangle$) are at distinct energies that are determined by the symmetry of the defect (spin-spin and spin-orbit interaction).

2.3.2 Properties of optical transitions

Once the wavefunctions are known, it is possible to calculate the selection rules of optical transitions between the *ae* triplets (excited state) and the e^2 triplet (ground state). The dipole moment between the ground and excited states is produced by the hole left in the a orbital under optical excitation. As expected from symmetry arguments, the expectation values of the matrix elements $\langle a|\, \hat{x} \cdot r\, |e_x\rangle$ and $\langle a|\, \hat{y} \cdot r\, |e_y\rangle$ are non-zero, where $\hat{x}$ and $\hat{y}$ represent the linear polarization of the involved photon. We can then calculate the selection rules for transitions between every pair of ground and excited states, as shown in Table 2.1.

The allowed optical transitions and their polarization properties again indicate two distinct groups. The states $|E_x\rangle$ and $|E_y\rangle$ are coupled to the $m_s = 0$ ground state with opposite linearly polarized light fields and have no coupling to the other two ground

Table 2.1: Selection rules for optical transitions between the triplet excited state (ae) and the triplet ground state (e^2). Linear polarizations are represented by $\hat{x}$ and $\hat{y}$, while circular polarization are represented by $\hat{\sigma}_\pm = \hat{x} \pm i\hat{y}$. As an example, a photon with σ_+ polarization is emitted when the electron decays from state A_2 to state $|-1\rangle$.

Pol	A_1	A_2	E_1	E_2	E_x	E_y
$\|-1\rangle$	$\hat{\sigma}_+$	$\hat{\sigma}_+$	$\hat{\sigma}_-$	$\hat{\sigma}_-$		
$\|0\rangle$					$\hat{y}$	$\hat{x}$
$\|+1\rangle$	$\hat{\sigma}_-$	$\hat{\sigma}_-$	$\hat{\sigma}_+$	$\hat{\sigma}_+$		

states. In short, transitions associated with these two states are *cycling* transitions. While the remaining four states are coupled to both the $m_s = +1$ and $m_s = -1$ ground states with opposite circular polarization. These states form Λ type transitions. For the $|A_1\rangle$ and $|A_2\rangle$ states, the Λ type transition properties are relatively robust against perturbations, because of the spin-spin and spin-orbit interactions that separate these states from each other, and other states in energy. The $|A_1\rangle$ state is coupled non-radiatively to a metastable singlet state (shown as ae singlets in Figure 2.3), which then decays to the ground state $|0\rangle$ and results in leakage out of the ideal Λ system consisting of the $|A_1\rangle$ state and the $|\pm 1\rangle$ states. Thus, we find that the $|A_2\rangle$ state provides a *closed* Λ scheme (indicating that the ground state never escapes to the $m_s = 0$ state) while the $|A_1\rangle$ state forms an *open* Λ scheme.

2.3.3 The effect of strain

In order to understand possible imperfections caused by deviations from the ideal case, we now discuss the effect of local strain on the properties of the optical transitions. This perturbation splits the degeneracy between the orbitals e_x and e_y and results in their mixing. We've already covered the zero strain limit. In the limit of

high strain (larger than the spin-orbit splitting), the excited state manifold splits into two triplets, each with a particular well defined spatial wavefunction. Orbital and spin degrees of freedom separate in this regime and transitions are excited by linearly polarized light. From now on we will refer to NV centers that have a strain splitting smaller or larger than the spin-spin and spin-orbit interactions as NV centers with small or low strain, or large or high strain respectively.

For a more quantitative description we turn to the Hamiltonian given in Equation 2.3 and the strain Hamiltonian is given by [87, 83]

$$H_{strain} = \delta_1 \left(|e_x\rangle\langle e_x| - |e_y\rangle\langle e_y|\right) + \delta_2 \left(|e_x\rangle\langle e_y| + |e_y\rangle\langle e_x|\right) \tag{2.6}$$

where δ_1 and δ_2 are parameters describing the strength of the crystal strain respectively along and perpendicular to the mirror axis of the defect. Figure 2.5 shows an example of how δ_1 strain splits and mixes the excited states, and as a result changes the transition frequencies and polarization properties of the optical transitions.

To see how the Λ type transitions are affected by strain, consider the $|A_2\rangle$ state as an example. The δ_1 strain mixes it with the $|E_2\rangle$ state. For δ_1 much smaller than spin-spin and spin-orbit interactions the effect of the mixing is negligible, and $|A_2\rangle$ state maintains the character for no-strain case. For δ_1 much bigger than spin-spin and spin-orbit interactions as described earlier, the states $|E_2\rangle$ and $|A_2\rangle$ are mixed such that the spin and orbital wavefunctions are separable. A similar effect occurs for δ_2 strain, where $|A_2\rangle$ is mixed with $|E_1\rangle$.

Since the strain Hamiltonian only splits and mixes the otherwise degenerate e_x and e_y states, its effect on the cycling transitions is to produce the eigenstates that are superpositions of the $|E_x\rangle$ and $|E_y\rangle$ states. The transitions from these eigenstates

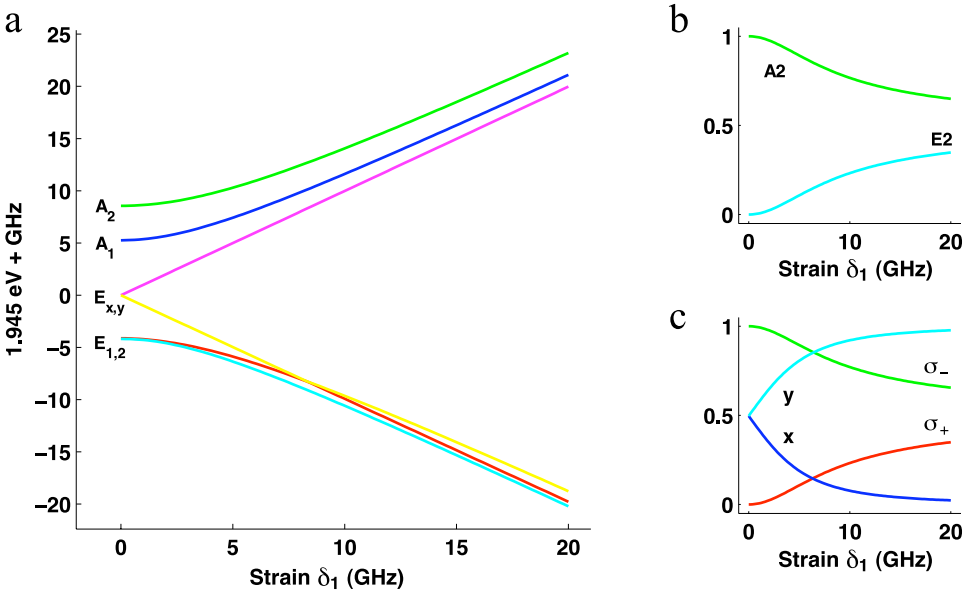

Figure 2.5: Effect of strain on the properties of the NV center. **a.** Energies of the excited states as a function of strain, expressed in units of the linear strain induced splitting between the $|E_x\rangle$ and $|E_y\rangle$ states. **b.** Strain induced mixing of the $|A_2\rangle$ and $|E_2\rangle$ states, showing the fraction of A_2 and E_2 character of the highest energy excited state. **c.** Polarization character of the optical transition between $|A_2\rangle$ state and the ground state $|+1\rangle$ as a function of strain. As strain increases, the polarization changes from circularly to linearly polarized. The transition between $|A_2\rangle$ and $|-1\rangle$ shows the same behavior, except with σ_- and σ_+ switched. Therefore, at high strain, decay from the $|A_2\rangle$ results in a separable state of the photon polarization and spin rather than an entangled state.

to the ground state $|0\rangle$ are linearly polarized along and perpendicular to the strain direction. The energy splitting between these two orthogonal linearly polarized transitions gives a measurement of the magnitude of the strain perpendicular to the NV axis at the location of the NV center.

It is worth mentioning that while the excited state configuration is highly affected by strain, the ground state configuration is unaffected to first order due to its anti-symmetric combination of e_x and e_y orbitals. It is also protected by the large optical energy gap between the ground and excited state to second order perturbation in strain.

2.3.4 Spin-spin interaction and effects of magnetic fields

So far the interactions considered for the *ae* triplets do not mix the $m_s = 0$ spin levels with $m_s = \pm 1$. But a careful analysis of the spin-spin interaction[83] predicts a term that mixes different states that transform as the irreducible representation E_1:

$$H'_{ss} = \Delta'' \left(|E_1\rangle \langle E_y| + |E_y\rangle \langle E_1| - i\,|E_2\rangle \langle E_x| + i\,|E_x\rangle \langle E_2| \right)$$

where Δ'' is believed to be small ($\Delta'' \sim 0.2$ GHz) [87]. This interactions mixes different spin sub-levels causes, for example, the cycling transitions ($|E_x\rangle$, $|E_y\rangle$) considered have a finite branching ratio into the $|\pm 1\rangle$ ground states.

Finally we note that the *ae* triplets are susceptible to magnetic fields. The g factor for the excited state is the same as for ground state[76], but for the work presented in this thesis the applied magnetic fields will be much smaller compared to the strain, spin-spin and spin-orbit interactions, hence any effect of the magnetic field will be neglected in the excited state.

In summary, the model for the *ae* states predict that the behavior of different NV centers probed could be vastly different depending on the local strain at the NV center. Not only could the transition frequencies be different from NV center to NV center, but the associated selection rules could be different also. This fact generally complicates the interpretation of ensemble experiments with NV centers as the strain is generally not homogeneous across the probed volume of a sample. We will next consider experimental tools applicable to single NV centers that allow us to study the predictions of the above model.

2.4 Absorption spectroscopy

Once an individual NV center has been isolated with confocal microscopy, the energy splitting between different levels predicted in the model can be tested experimentally by scanning a resonant laser across the relevant transitions.

The resonant laser coherently drives population from the ground state to the relevant excited state for an allowed transition and, consequently, NV center decays from the excited state both via the zero-phonon-line (ZPL) and the the phonon-side-band (PSB). The excitation laser and the fluorescence from the NV center can easily be separated using dichroic filters, hence a plot of fluorescence in the PSB as a function of laser frequency is easy to obtain.

The particular spectral features that are visible in such an absorption spectroscopy plot depend on both the properties of the NV center being used and the exact conditions under which the experiment is carried out (illustrated in Figure 2.6). Specifically, the polarization, power, and duration of the resonant laser, and the state that the NV

center is in before the resonant laser is turned on all play a role. For the experiments shown below a single linearly polarized laser with 2 μW of peak power is turned on for 5 μs. The relatively short duration ensure the dynamics associated with finite branching ratio out of particular states are minimally effecting the spectra measured. To suppress any optically-induced coherent effects (e.g. coherent population trapping) in the ground state a magnetic field $\sim$ 10 G is applied to split the the $|\pm 1\rangle$ states. The peak power used and the intrinsic linewidth of the transitions determines the width of the transitions observed in the absorption spectra..

If the NV center is initialized in a particular state before being probed by the laser, the absorption spectra will show spectral features associated with transitions that are allowed from that initial state. In particular for a typical "low-strain" NV center, if the NV center is prepared in the $|0\rangle$ state, only two transitions (from $|0\rangle$ to $|E_x\rangle$ and $|E_y\rangle$) are visible (illustrated in Figure 2.6b). To observe all spectral lines all spin ground state spin levels need to be populated. Two methods are illustrated in Figure 2.6a, one uses microwave and the other uses two lasers to keep some population in all ground-state spin levels . The resulting spectra shown in Figure 2.6c-d now show all associated and expected transitions for the NV center.

The fact that we can selectively observe different spectral lines with the appropriate state preparations allow us to unambiguously assign each spectral feature with a particular transition. Once spectral lines are identified, the relative energy splitting in the excited state can be calculated using the known energy splittings of the ground state (illustrated in Figure 2.6e). As the frequency difference between the $|0\rangle$ to $|E_x\rangle$ and $|E_y\rangle$ transitions gives a direct measurement of the strain splitting we can plot

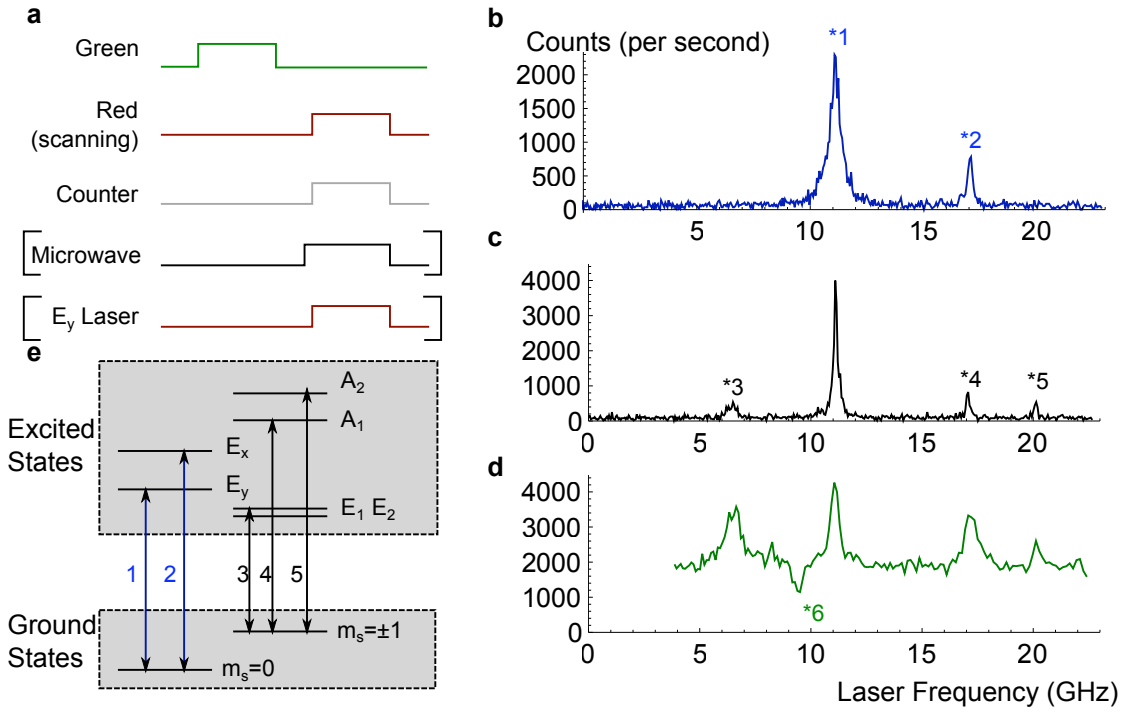

Figure 2.6: Probing energy spectrum of an NV center using absorption spectroscopy. **a.** Different pulse sequences used to obtain absorption spectra. A 1 μs pulse of green laser is used to initialize the NV center into the $|0\rangle$ state. Next, a red laser of varying frequency is turned on for 5 μs, and the counts accumulated in the PSB during the red laser pulse are plotted as the frequency of the laser is linearly varied. The sequence is repeated 200 times at the same laser frequency before moving onto the next point in the frequency ramp. The plots shown are averages of 40 such linear ramps. For panel c a microwave resonant to the $|0\rangle \leftrightarrow |\pm 1\rangle$ transition at 2.87 GHz is driven by a mW of RF power, continuously 1 μs before and during the red laser. For panel d a 1 μW laser resonant to the $|0\rangle \leftrightarrow |E_y\rangle$ transition is kept on with the scanning laser. Both of these methods ensure that all possible ground states are occupied. **b.** Results of an absorption scan after initializing the NV center into the state $|0\rangle$. Two transitions are visible (labeled $*1$ and $*2$ corresponding to the $|0\rangle \leftrightarrow |E_y\rangle$ and $|0\rangle \leftrightarrow |E_x\rangle$ frequencies respectively). **c**. Using the microwave to maintain population in all ground states leads to new spectral features to appear ($*3$, $*4$, $*5$) corresponding to $|\pm 1\rangle$ to $|E_{1,2}\rangle$, $|A_1\rangle$ and $|A_2\rangle$ respectively. The transitions $E_{1,2}$ are under the same spectral peak $*3$. The transition frequency of $|\pm 1\rangle \leftrightarrow |A_1\rangle$ is accidentally the same as that of $|0\rangle \leftrightarrow |E_x\rangle$, hence both are identified under spectral feature $*4$ (note though the change in the lineshape of $*4$). **d.** A laser tuned to the $|0\rangle \leftrightarrow |E_y\rangle$ transition maintains some population in $|\pm 1\rangle$ in addition to the $|0\rangle$. Transitions that deplete the population in $|0\rangle$ are then shown as peaks with a negative peak (*6). (*6) corresponds to transitions from $|\pm 1\rangle$ to $|E_y\rangle$. **e.** Approximate level structure for the NV center being probed. Transitions from the ground state to the excited state are shown in solid lines and are labeled by numbers corresponding to the spectral features identified on other panels.

the relative energy splitting within the *ae* triplets for a given strain. Figure 2.7 shows datapoints obtained for such a measurement and compares it to the predictions of the model discussed earlier (similar to [88]).

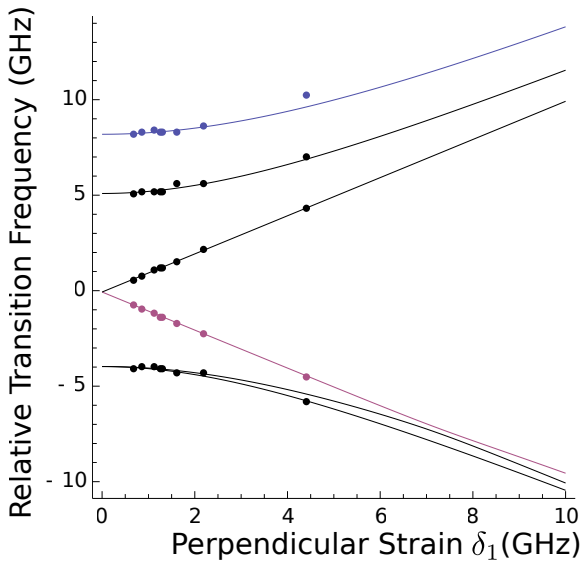

Figure 2.7: A plot of the relative energy levels of the *ae* triplets vs strain (same as in Figure 2.5) with data points (solid points) for NV centers measured in a natural type-IIa diamond using absorption spectroscopy. The spectra was measured using an identical sequence to those used to obtain Figure 2.6c. For the absorption spectra measured the E_x, E_y splitting is used to calibrate the magnitude of the strain perpendicular to the NV axis and the relative frequency splittings are inferred from the known splittings between different energy levels in the ground state (illustrated in Figure 2.6).

As Figure 2.7 illustrates the predicted behavior of the model fits extremely well with the measured parameters. We also note that the parameters for the model were measured with a separate piece of diamond[88], no adjustments of the model parameter was done for the figure.

Absorption spectroscopy also allows one to extract the polarization properties of each transition. Characterization of polarization selection rules have been carried out to identify that the $|0\rangle$ to $|E_x\rangle$ and $|0\rangle$ to $|E_y\rangle$ transitions are orthogonally linearly

polarized[89]. In chapter 3 it will be shown that for low-strain NV centers the $|A_2\rangle$ to $|\pm 1\rangle$ transitions are circularly polarized.

In summary, the absorption spectroscopy is useful in characterizing the energy spacing of levels within the *ae* triplets. This level spacing can be used to predict the properties of the appropriate transitions using the model introduced earlier.

In principle, by carefully preparing the NV center in a particular state and observing the changes with power and duration of the laser pulse in the lineshape and the strength of the spectral features, one can also extract the appropriate branching ratios for each of the states. These branching ratios are a result of the excited states being mixed, and are predicted with our theoretical model. As the dynamics associated with the multiple level system can be quite complex, it is much easier to extract the branching ratio information by looking at the time-traces of fluorescence while resonantly exciting a single transition.

2.5 Fluorescence timetraces

If a laser is tuned to a particular transition between the ground state and the excited states, the long-time (longer than $1/\gamma$ where γ is the lifetime of the excited state) fluorescence from the excited state will be independent of any coherences between the ground and excited states, and the changes in the fluorescence intensity will be limited by the dynamics associated with possible decay channels out of the states being driven. In particular, if a transition is perfectly cycling one can expect to observe no change in the fluorescence intensity as a function of time after the excited state lifetime has damped initial coherent oscillations. In the case where there is a

branching out of the excited state to a state that is "dark" for the excitation, for instance because the associated transitions out of those states are far detuned, the fluorescence intensity will decrease over time until all of the population is pumped to the dark state. The timescale associated with this decay will be given by the rate at which the optical excitation occurs as well as the branching ratio into the dark state. This pumping mechanism can be used to prepare the emitter in the dark state which can, for example, be a well-defined spin sub-level of the ground state.

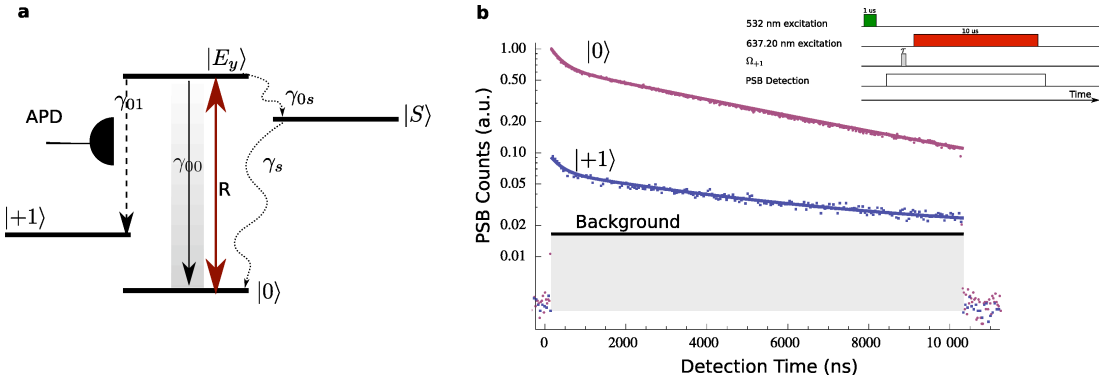

Figure 2.8: Decay of fluorescence under resonant excitation. **a** Model used to simulate the dynamics of optical transitions leading to fluorescence time traces shown in (b). R gives the optical pumping rate of the $|0\rangle \leftrightarrow |E_y\rangle$ transition. From the $|E_y\rangle$ state, γ_{00} and γ_{01} are decay rates to the $|0\rangle$ and $|\pm 1\rangle$ states, respectively. γ_{0s} and γs are the non-radiative decay rates into and out of the metastable singlet state $|S\rangle$. **b** Histograms showing time traces of fluorescence as recorded in the PSB following spin initialization to either the $|0\rangle$ (red) or $|1\rangle$ (blue) state. Solid lines show simulated fluorescence from the NV center using the model shown in (a) and described in the text. Two other similar data sets at different laser powers were used to determine the branching ratio of $|E_y\rangle$ to $|\pm 1\rangle$ and the spin polarization. Inset shows the pulse sequence used to obtain the recorded time traces.

For the levels in the *ae* triplets there are three decay channels that need to be considered. Figure 2.8a illustrates these decay channels for the E_y state. The timescales associated with these decay channels are generally distinct such that a bi-exponential

fit can generally model the change in flourescence intensity while driving a particular transition.

To characterize the branching ratios associated with these decay channels for an NV center with 3 GHz frequency difference between the $|E_x\rangle$ and $|E_y\rangle$ states, we record time traces of the fluorescence during the resonant excitation where the state is initialized either in $|0\rangle$ or $|1\rangle$ using the pulse sequence shown in Figure 2.8b (inset). These are then compared to a model of the NV center dynamics similar to the one discussed in [79] and illustrated in Figure 2.8a. The model involves the $|0\rangle$ and $|\pm1\rangle$ ground states, the $|E_y\rangle$ state, and a metastable singlet state $|S\rangle$. The branching ratios from $|E_y\rangle$ state to $|0\rangle$, $|\pm1\rangle$, and $|S\rangle$ are related to the decay rates $\gamma_{00} = 1/12$ns, γ_{01}, and γ_{0s}, respectively. γ_{00} is determined by lifetime measurements, and the singlet decay rate to $|0\rangle$ is set to $\gamma_s = \gamma_{00}/33$, as given in [79]. We then simulate the evolution of the system under a continuous optical pumping of the $|0\rangle \rightarrow |E_y\rangle$ transition at a rate R, starting with some initial spin population for the two cases of initialization in $|0\rangle$ or $|1\rangle$. To estimate the values of γ_{01}, γ_{0s}, R, and the spin polarization, these parameters are varied to fit the simulation to the data by eye. This was done for three different laser powers. Using this method, we estimate the branching ratio out of the system of $m_s = 0$ states to be $0.92 \pm 0.16\%$ ($\gamma_{01} \sim \gamma_{00}/109$) and $\gamma_{0s} \sim \gamma/20$, and the imperfection in spin preparation to be $7.2 \pm 1.8\%$.

The same method can be applied to measure the branching ratios for other states in the *ae* triplets also. For example for an NV center with 3.5 GHz $|E_x\rangle$ and $|E_y\rangle$ splitting associated time traces of $|A_1\rangle$, $|A_2\rangle$ and $|E_y\rangle$ are shown in Figure 2.9. Analogous to the pulse sequence in Figure 2.8b, we first prepare the NV center in either

the $|\pm1\rangle$ or $|0\rangle$ state via optical pumping, and excite the $|\pm1\rangle \leftrightarrow |A_{1,2}\rangle$ or $|0\rangle \leftrightarrow |E_y\rangle$ transitions individually while collecting fluorescence as a function of time. For Λ type transitions, coherent population trapping in the ground state affects the fluorescence dynamics. For these experiments a magnetic field along the NV axis of about $B =\sim$ 5 G is applied to split the $|\pm1\rangle$ states by $\delta = 2g\mu_B B$ to ensure coherent effects in the ground state due to the optical excitation are minimized in the measured data (see Appendix B for details). Figure 2.9 shows double-exponential fits to data from NV center for all three transitions.

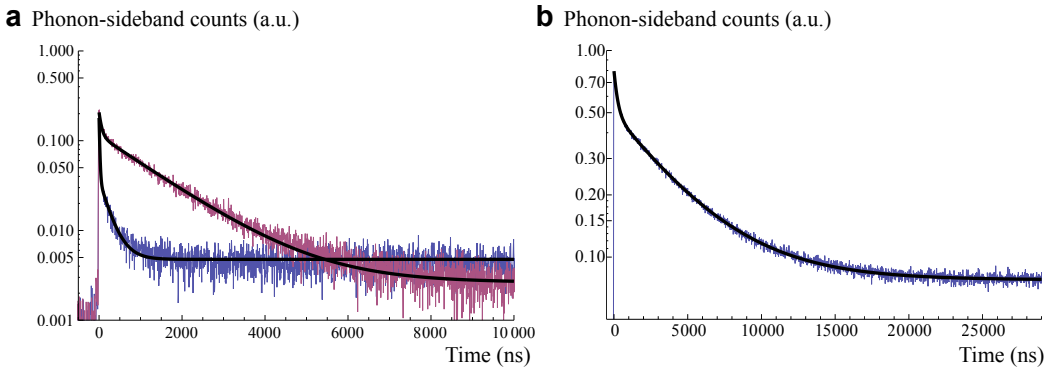

Figure 2.9: Fluorescence decay of **(a)** $|A_1\rangle$ (blue), $|A_2\rangle$ (red), and **(b)** $|E_y\rangle$ states with fits to double exponential decays (black lines).

For the $|A_2\rangle$ state, the short timescale correspond directly to the timescale of optical pumping to the electronic dark state of the $|\pm1\rangle$ states, and is governed by the optical excited state lifetime γ. Given a finite δ, this process should lead to a steady state fluorescence rate. The presence of a second long timescale then indicates a decay out of the three level system into the singlet and subsequently the $m_s = 0$ manifold. For the $|A_1\rangle$ state, we expect the fast decay into $|0\rangle$ via the metstable singlet to give rise to a short timescale. Following this fast process, the remaining

population in the electronic dark states escape due to δ and gives rise to another longer time scale. Therefore, we find the decay rates into the metastable singlet to be $\gamma_{s1} \sim 1.6\gamma$ and $\gamma_{s2} \sim 130\gamma$, for the $|A_1\rangle$ and $|A_2\rangle$ states respectively, where γ is the direct decay rate back into the ground state. For the $|E_y\rangle$ state we find $\gamma_{01} \sim \gamma_{00}/105$ similar to the earler NV center.

We note that even though the combination of the rate equations with fluorescence time traces gives an accurate estimation of the different branching ratio parameters, in our knowledge, this (or other) techniques have not been applied to a systematic test of how these branching ratios change with the perpendicular strain. The systematic study would be essential to pinning down the exact mechanism of mixing in the excited, which might also be affecting the polarization selection rules[89]. The branching ratios extracted here will be used in other chapters where the branching ratios are needed to characterize the behavior of the NV centers under resonant excitation.

2.5.1 Applications to ground state spin detection

It is possible to use the cycling transition and the fluorescence decay curves obtained so far to accurately measure the population in the $|0\rangle$ spin sub-level in the ground state. Spin readout is achieved through resonant laser excitation tuned to the $|0\rangle \leftrightarrow |E_y\rangle$ transition[88]. As the $|0\rangle \leftrightarrow |E_y\rangle$ transition is cycling for low strain and is isolated in frequency from other transitions, the fluorescence collected in the presence of the resonant laser field should be proportional to the population in the $|0\rangle$ state.

Figure 2.5.1(a) shows microwave Rabi oscillations detected using the resonant readout scheme. Following a polarization step carried out with a green laser, a mi-

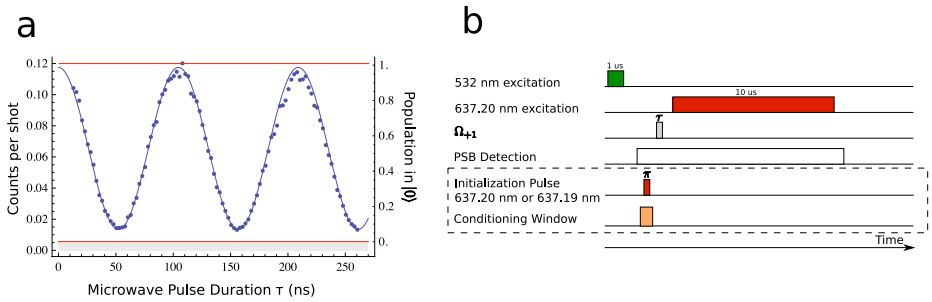

Figure 2.10: **Spin readout via resonant excitation a** Microwave Rabi oscillations (in blue) recorded using the pulse sequence given in (b). Left vertical axis shows the average number of counts received for a particular length of microwave pulse duration (τ). Right vertical axis shows the normalized population in the $|0\rangle$ state for the same pulse duration. The red lines are maximum and minimum readout levels obtained using the technique described in Appendix A. **b** Pulse sequence used for part (a). In the unconditioned case, 532 nm light is turned on for 1 μs to polarize the electronic spin to $|0\rangle$ state. After 6 μs, a microwave pulse resonant to the $|0\rangle \leftrightarrow |+1\rangle$ of varying duration is applied. Finally a 10 μs light pulse resonant to the $|0\rangle \leftrightarrow |E_y\rangle$ transition is turned on 1 μs after the microwave pulse and counts in the PSB are recorded in this interval. The boxed section is described in Appendix A.

crowave pulse of varying length and resonant to the $|0\rangle \leftrightarrow |1\rangle$ transition is applied and the resulting state is read out using the resonant excitation. In an ideal preparation and readout scenario, the $|0\rangle$ state would be bright while the $|\pm1\rangle$ states would be completely dark. The high level of fluorescence achieved for the $|0\rangle$ state is limited by the branching ratio between the $|E_y\rangle \rightarrow |0\rangle$ and $|E_y\rangle \rightarrow |\pm1\rangle$ transitions (~99 % as measured above) and the collection efficiency to about 0.11 counts per shot. Thus multiple repetitions of the experiment are needed to build up enough statistics for an accurate estimation of the initial state. When the NV center is nominally prepared in the $|+1\rangle$ state, we observe counts above the background level, which may be due to imperfect spin polarization or additional fluorescence from the $|+1\rangle$ state.

The pulse error associated with a square pulse of finite Rabi frequency (around 10

MHz) is estimated to be about 3 %. The error is mostly due to the presence of the hyperfine interaction with the nuclear spin of ^{14}N associated with the NV center[90]. We thus estimate the spin polarization after the green excitation to be $96 \pm 1.9\%$.

Appendix A presents further calibration of these results that will be essential to results presented in Chapter 3.

In summary, we find that resonant excitation is an exceptionally useful tool for spin readout of the NV center. Not only can we use it to extract information about populations in relatively few repetitions, but it allows us to fully characterize various procedures related to the spin manipulation of the NV center, for example spin polarization achieved or pulse errors, with very few assumptions. In an impressive demonstration, Robledo, et al. [75], have shown that by improving the collection efficiency by using Solid Immersion Lenses and using NV centers with lower strain (better "cycling" transitions) it is possible to determine the spin-state of the NV center in a single shot.

Having used the long time behavior ($> 1/\gamma$) of florescence under resonant excitation to characterize various predictions of our theoretical model, we next turn to demonstration of coherent oscillations between the ground and excited states.

2.6 Rabi oscillations between ground and excited states

Coherences between ground and excited states are essential to rapid (as fast as a few ns) and state-selective transfer of population from the ground state to the

excited state. The study of the coherences provide information about the dynamics of environment around the NV center that affect the optical transition and lead to decoherence. Motivated by potential applications of the study of coherences between the ground and optically excited states here we demonstrate coherent Rabi oscillations similar to demonstrations carried out with NV centers in [91, 92].

After a 1 μs green laser pulse initializes the NV center in the $|0\rangle$ state a strong (40 μW) resonant excitation tuned to the $|0\rangle \leftrightarrow |E_y\rangle$ transition is turned on. A waveguide based EO modulator (Guided Color Technologies) with a 1 ns rise-time allows the creation of short pulses of variable length. Figure 2.11 a (gray trace) demonstrates a 40 ns drive pulse that was used for this experiment. This strong excitation begins to coherently drive the NV center between the ground state and the excited state with a frequency given by $\Omega = \vec{\mu} \cdot \vec{E}$, where $\vec{\mu}$ is the dipole moment and $\vec{E}$ is the electric field oscillating at the resonant frequency. This drive leads to oscillations in the excited state population. These oscillations are apparent for the first 10 ns of the trace shown in Figure 2.11. The spontaneous decay from the excited state allows us to continuously monitor the excited state population in the excited state via the fluorescence emitted by the NV center, but it also damps the oscillations. The oscillations appear damped also because of power fluctuations in the laser, the relative drift between the laser and the NV center transition frequency, as well as any additional dephasing process that might be taking place in the excited state. The excited state population then reaches a steady state value where no further oscillations are observed. Finally, when the excitation laser is switched off, the population in the excited state decays with the spontaneous decay rate of $1/\gamma = 11.8 \pm 0.3$ ns.

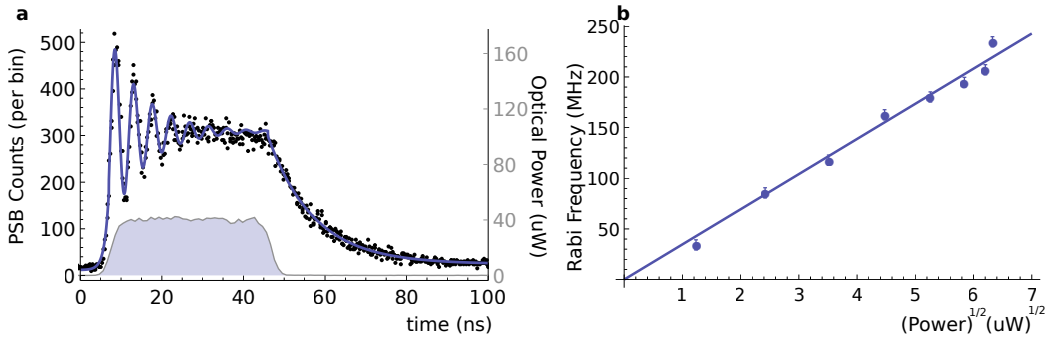

Figure 2.11: Rabi oscillations between $|0\rangle$ ground state and $|E_y\rangle$ excited state. **a** Time trace of the excited state population under a strong coherent drive (black points, blue line and left axis). The population in the excited state is measured using the spontaneous decay from the excited state to the phonon side band. Gray trace shows the applied pulse shape with a peak power of 40 μW (the right axis). **b** Power dependence of the measured Rabi frequency. The fitted line agrees with the expected $(\text{Power})^{\frac{1}{2}}$ behavior.

The processes that lead to dephasing of these coherent oscillations will be further studied in Section 2.8 and Robledo, et al. [92] have studied the causes of decoherence in the context of Rabi oscillations between the ground and excited states. To explore the causes of decoherence we will first consider how we can controllably change the level structure of a single NV center using the Stark effect.

2.7 Modifying optical properties: electric field tuning of NV centers

Controllably modifying the optical properties of the NV center is an important tool for exploring and using NV centers in a quantum optics perspective. For example, controllably tuning two NV centers to have the same transition frequencies allow for demonstrations of indistinguishable single photons from separate NV centers (see

Chapter 4). The *ae* triplets exhibit DC stark shifts due to static electric fields. This allows us to change the transition frequency and the associated properties of the optical transitions by applying static electric fields.

Strain and electric field affect the *ae* level structure in a very similar way. In fact, the electric field can be modeled either as directly causing changes because of the permanent electric dipole associated with the orbital wavefunctions, or it can also be explained through the reverse-piezo electric effect[83], where electric field changes the local strain around the NV center and the strain affects the associated states. As the two effects are inseparable at this point, we will take the permanent electric dipole picture as it is much more intuitive to work with. The similarity between the effect strain and electric field means the behavior of the transitions are sensitive to the effective field that is made up of the built-in strain as well as the applied electric field [93, 94, 95]. In a phenomenological model[2] we can modify H_{strain} to include electric fields also[83, 94, 95]:

$$\begin{aligned} H_{strain} + H_{stark} &= (\delta_1 + f_x)\left(|e_x\rangle\langle e_x| - |e_y\rangle\langle e_y|\right) + (\delta_2 + f_y)\left(|e_x\rangle\langle e_y| + |e_y\rangle\langle e_x|\right) \\ &+ f_z\left(|e_x\rangle\langle e_x| + |e_y\rangle\langle e_y|\right) \end{aligned} \tag{2.7}$$

where f_i is used to designate the strength of the electric field in the i direction in frequency units. The symmetry plane sets the x axis in an identical way to how the e_x and e_y states are defined[83]. Based on the work by Tamarat, et al., [93], f_i have a

[2]For simplicity we provide the phenomenological model where the effect of the electric field is considered to only affect the e_x and e_y orbitals. In reality the affect of the z component of the electric field is due to the difference in the dipole moments in the ground and excited states, thus $f_z = (\mu_{E,\parallel} - \mu_{G,\parallel})E_z/h$ where $\mu_{i,\parallel}$ refers to the dipole moment of either the (E)xcited or (G)round states, E_z is the electric field in the z direction and h is the Planck's constant. In our experiments where the vector electric field control is imprecise it is hard to distinguish the exact value of the components of $\mu_{i,\parallel}$ or $\mu_{i,\perp}$, so we model the difference as a smaller f_z component, similar to work carried out by Bassett, et al. [95].

scaling coefficient of 6.3 GHz/ (MV m^{-1}), corresponding to about 1 Debye. We now turn to an experimental demonstration of the electric field tuning of NV centers.

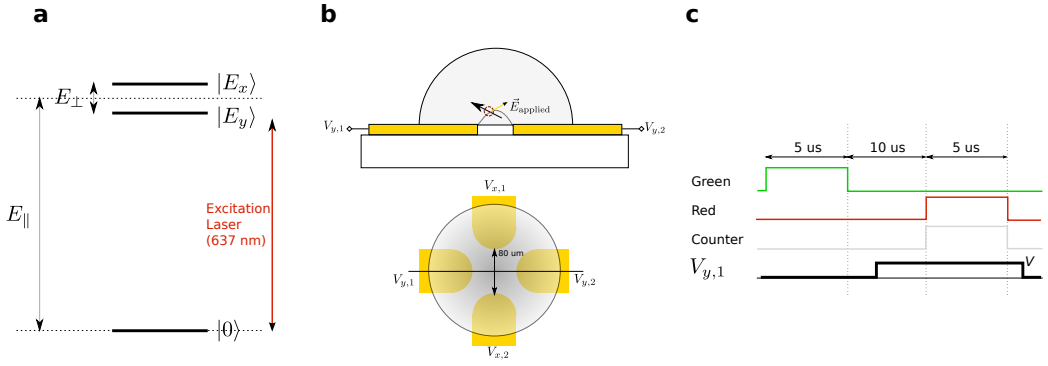

Figure 2.12: Electric field tuning of NV centers. **a** Effect of components of electric field, in the absence of strain, on the two cycling sub-levels of *ae* triplets ($|E_x\rangle$ and $|E_y\rangle$). The electric field vector perpendicular to the NV axis ($E_\perp = \sqrt{f_x^2 + f_y^2}$) changes the relative detuning between the two states while the electric field parallel to the NV axis ($E_\parallel = f_z$) changes the relative frequency between the ground state and the two excited states simultaneously. **b** Schematic of the experimental setup used to test electric field tuning of NV centers. **c** Pulse sequence used to probe the effect of electric fields.

A schematic of the experimental setup used is shown in Figure 2.12. The diamond containing the NV centers, shaped as a hemisphere to increase collection efficiency, is placed on a silicon substrate with gold electrodes (30 nm thick) defined using photolithographic techniques. Four electrodes, separated by 80 μm, are defined to control the direction of the electric field, but since the position of the NV center inside the diamond is hard to control, we find that only a single electrode makes a significant difference in the transition frequencies. The remaining three electrodes are grounded for this experiment ($V_{y,1} = V$ and $V_{x,1} = V_{y,2} = V_{x,2} = 0$).

In addition to the complication of the placement of NV centers relative to the electrodes, the presence of the strain adds a built-in field that is oriented indepen-

dently from the applied field. In fact, if there is little control over the direction of the electric field and if the field applied field is changed by changing a single potential, the change in the frequency of transitions can have linear or quadratic behavior versus the applied field[93]. As noted in other works [94, 95], this behavior is captured by Equation 2.7. For a single electrode we can write the electric field at the NV center as $\vec{f} = \alpha V\,(v_x, v_y, v_z)$. Where v_i are the unit vectors in the symmetry coordinates of the NV center of the electric field due to the potential V applied to the gate and α is the proportionality constant. If we assume the applied field is only in the x direction eigenvalues of $H_{strain} + H_{stark}$ are given by:

$$\alpha V v_z \pm \sqrt{(\delta_1 - \alpha V v_x)^2 + (\delta_2)^2} \tag{2.8}$$

We will consider the $|E_x\rangle$ and $|E_y\rangle$ states only, and to first order superpositions of these states are then eigenstates of the $H_{strain} + H_{stark}$ Hamiltonian. This approximation holds as long as Δ'' is small compared to the energy spacing between the $|E_y\rangle$ and $|E_1\rangle$ and $|E_2\rangle$ levels (i.e. for both small strain and large strain). For the purpose of demonstrating electric field tuning, in experiments, we will initialize the NV center into the $|0\rangle$ state and carry out absorption spectroscopy while changing the electric field (illustrated by the pulse sequence in Figure 2.12c).

As Figure 2.13b illustrates that the change in the center frequency of the transitions matches the predictions from the above model. We note though that the data does not match the model perfectly. Green light induced changes that rectify the applied field[95] are probably causes of the difference between the model and experimental data. Further Figure 2.13b shows that the width of the lower branch is broad when the branch separation is between $\sim$ 13- 22 GHz, corresponding to the lower

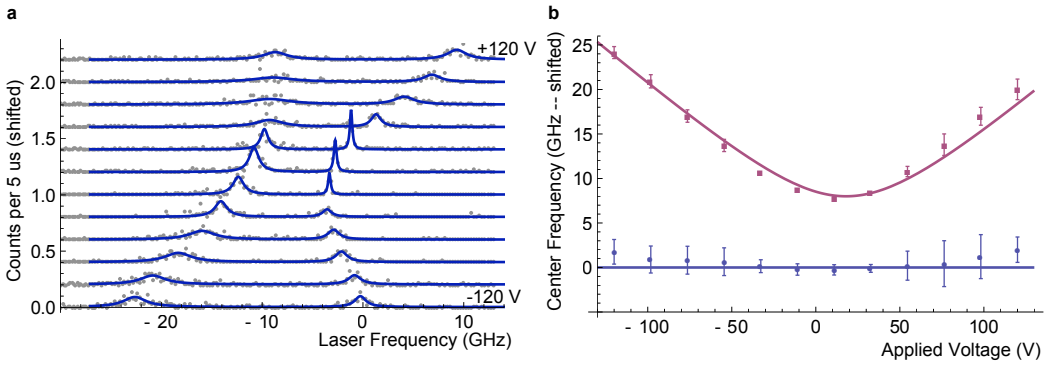

Figure 2.13: Demonstration of electric field tuning of NV centers. **a** Absorption spectroscopy based on the pulse sequence shown in Figure 2.12c, where for each line a different V is applied. For each line the V changes by 12.5 V where the maximal values of the applied voltage are noted on the margin. **b** Plot of the center frequencies (dots) where the fit value for the transition of the lower frequency branch has been subtracted from the center frequencies plotted and the widths (error-bars) of the transitions as a function of applied voltage V. Solid lines are a fit to Eqn. 2.8 where $\alpha = 0.1$ GHz/V, $\delta_1 = 0.7$ GHz, $\delta_2 = 6$ GHz, $v_x = 0.5$, $v_y = 0$, $v_z = 0.9$.

branch level crossings shown in Figures 2.5. The width measured is effected by the complicated level structure around the level crossing, and is not direct measurement of the electric field induced fluctuation of the levels (for a dataset where tuning does not induce broadening see Chapter 4).

In summary, as Figure 2.13 demonstrates, even with a single electric field gate it is possible to change the frequencies of transitions of an NV center. Moreover the relative splitting between the two transitions can be adjusted meaning an NV center can be tuned to an arbitrary point on Figure 2.7 to have desired selection rules. Basset, et al. [95], have carried out experiments with better control over the electric field direction where they have demonstrated the strain splitting between the $|E_x\rangle$ and $|E_y\rangle$ levels can be removed by applying the appropriately oriented electric fields.

Finally we note that the dependence of the optical transitions to the instanta-

neous electric field indicates that the optical properties and transition frequencies are sensitive to fluctuations in the local electric environment around the NV center. We next explore the effects of broadening of the optical transitions that are caused by the uncontrolled fluctuations of the local electrical environment around the NV center.

2.8 Electric environment of NV centers

The utility of the optical properties of the NV center discussed so far take advantage of the narrow individual lines and the fact that they can be addressed and driven coherently. For many quantum optics applications in the solid state the actual linewidth of the transitions also play a significant role. For the NV centers considered so far, absorption scans indicate that an average linewidth on the order of $\sim$ 100 MHz is typical. This is roughly 4 times the lifetime limited linewidth observed by Tamarat, et al., [93].

The process that leads to the broadening of the absorption lines is believed to be the charge fluctuations around the NV center. Specifically the nitrogen impurities, that are deep donors around 1.9 eV from conduction-band-minimum[96] are believed to be optically excited to the conduction band with the excitation lasers. The charge configuration around the NV center is believed to fluctuate as the donors loose and gain their charges under the optical excitation. These changes in the configuration effect the optical transition via the Stark effect discussed previously. This mechanism needs to be confirmed fully, but it provides a good working picture, which we will follow. Instead of referring specifically to nitrogen impurities we will refer to possible other optically ionizible impurities all as the charge environment.

With this picture, there are two key aspects of the charge environment that affect optical transitions of an NV center. First is the average linewidth caused by the magnitude of fluctuations associated with charge traps re-configuring. Second is the time it takes for the charge environment to reconfigure. If the "correlation" time of the electric field at the NV center is long to enough to determine if the electric field corresponds to a particular configuration, either post-selection techniques or active feedback can be applied to compensate for the fluctuations of the charge environment.

We can hope to use methods similar to those used successfully to explore spin dynamics in the ground state to obtain the correlation time of the charge environment, for example by using echo or Ramsey type interference techniques. Although these techniques are powerful they are difficult to implement as they require very precisely timed pulses that have very good extinction, and are state selective. Naively they also only provide information regarding the charge dynamics within the excited state lifetime. Instead we show that absorption spectroscopy and measurement of the emission linewidths can provide information regarding both the timescales as well as the average linewidth associated with the charge environment of the NV center.

2.8.1 Charge environment under resonant excitation

First we note a significant difference in power between the resonant excitation used (generally $< \mu$W for 637 nm) and the green excitation (generally $\sim$mW for 532 nm). In the charge fluctuations picture provided above, it is expected that the stronger green excitation should induce more significant changes simply because it will be able to efficiently excite more charge traps. With this observation, a naive expectation

is that a low-power resonant excitation can be used as a probe of the environmental configuration while a pulse of green excitation prepares the charge environment to a new configuration.

By completing absorption scans between successive pulses of green light, we can check if the transition frequencies of the NV center remains constant. We note similar experiments have been carried out by both the Fu, et al.,[80] and Robledo, et al.,[92]. Figure 2.14a shows a pulse sequence where spin initialization of the NV center is carried out with resonant light, and green laser is only applied after a laser frequency scan taking a few seconds is completed.

Observed absorption scans (Figure 2.14b) indicate a single narrow Lorentzian peak that remains at a fixed frequency until a new green laser pulse changes the central frequency of the absorption lineshape. The average full-width once the spectral shift due to excitation with green light has been accounted for (26 $\pm$6 MHz) is very close to the expected lifetime limit ($1/\pi/(12\,\mathrm{ns}) = 27$ MHz). This indicates that between green illuminations life-time limited photons can be obtained from NV centers. Moreover the correlation time of the charge environment is greater than a few seconds in the absence of green illumination.

It is not clear at this point whether the green illumination plays a direct role in re-configuring the charge environment around the NV center, or whether the ionization of the NV center itself triggers the re-configuration.

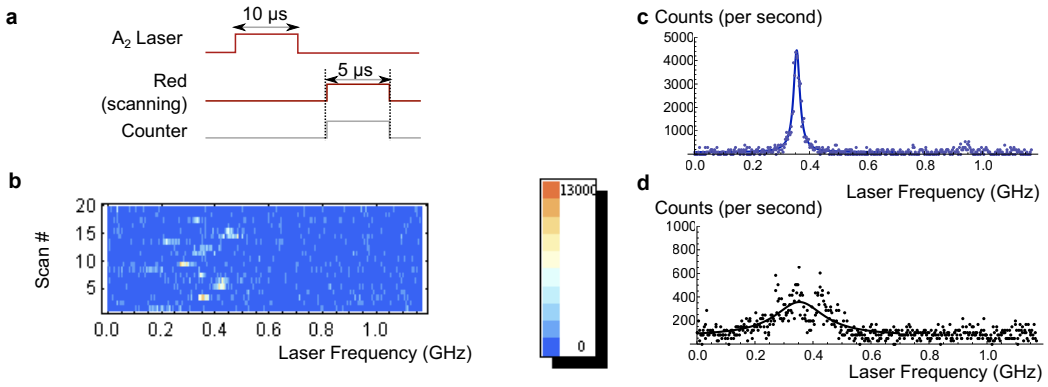

Figure 2.14: Resonant absorption scans illustrating the effect of the green laser on NV center's transition frequency. **a**. Pulse sequence applied to obtain each point in subsequent scans. The laser tuned to $|\pm 1\rangle$ to A_2 transition is used to optically pump the NV center into the $|0\rangle$ state, replacing the initialization used with green laser in earlier figures. The counts are collected during the next 5 μs where a resonant laser is turned on for the 5 μs. The frequency of the second laser is scanned linearly through the indicated range, and counts as a function of the frequency of the second laser are plotted. At any given frequency of the second laser the pulse sequence is repeated 200 times to improve the signal to noise. After the laser frequency returns to its beginning value (indicated as 0.0 GHz on the plots) a green laser pulse at saturation is turned on for 1 s. **b**. Results of individual line scans of the absorption spectrum. Illustrating the narrow lineshapes obtained between pulses of green light. For some scans, where no counts are obtained, the NV center is assumed to be ionized. **c**. Analysis of the data shown in b where a Lorentzian is fitted to each scan / lineshape in b and the frequency axis of each line is shifted so the centers of the different scans coincide. The data shown on this panel is then an average over the data shown in b after compensating for the jumps of the center frequency between scans. The FWHM is 26 $\pm$ 6 MHz. **d**. Analysis of the data shown in b where an average over the different scans is carried out without shifting the data. The FWHM is 200 $\pm$ 20 MHz.

2.8.2 Charge environment under green excitation

To characterize the properties of the charge environment under strong excitation by green light we will look at the emission spectrum from the NV center. The spectrum of the emitted photons are expected to represent the instantaneous charge configuration. By measuring the spectrum of the emitted photons, we can easily obtain an average emission linewidth under excitation by a green laser.

Coherence length measurements under with NV centers have previously been carried out with electron irradiated nanodiamonds[97]. These measurements, under continuous green illumination, indicate a coherence length on the order of millimeters, which is extremely short and hence indicates a very wide spectral emission. For applications using coherent emissions from NV centers, it is important to know whether the absorption spectroscopy gives an adequate estimate of the emission bandwidth under strong green excitation in pure samples where the absorption linewidths are hundreds of MHz.

To characterize the emission spectrum, we use a confocal cavity of finesse ~ 150 to spectrally measure the width of the emitted lines on the ZPL. Figure 2.15 illustrates the experimental setup used for the emission spectrum measurements. By using the linear polarization selection rules associated with $|0\rangle$ to $|E_x\rangle$ and $|E_y\rangle$ transitions, we use a polarizer to select out a single linearly polarized emission for the given NV center[78, 80]. The emission spectrum is shown (over time) in Figure 2.15b and the average over many scans (consisting of 10 minutes of data acquisition) is shown in Figure 2.15c. The FWHM (~ 80 MHz) of the emission is comparable to the measured FWHM of the absorption (~ 100 MHz).

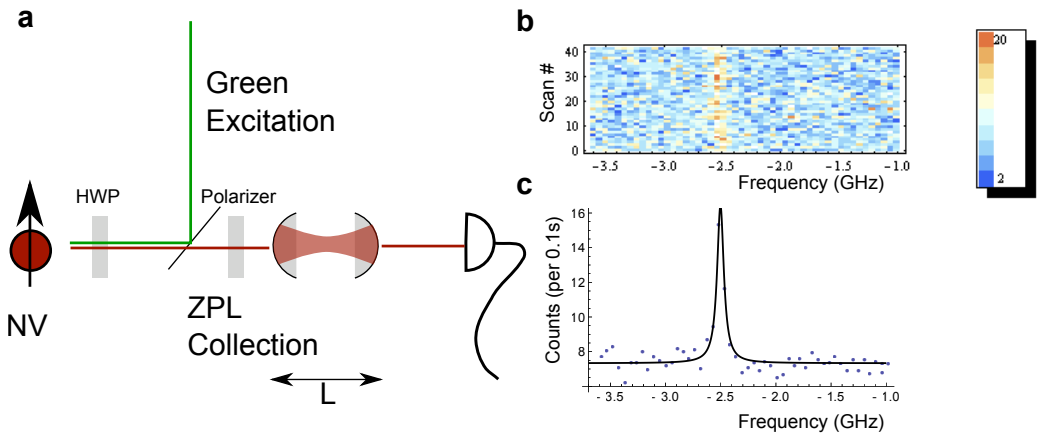

Figure 2.15: Emission spectrum measurement using a confocal cavity. **a**. Experimental setup, where the emission from an NV center is filtered in the ZPL using a dichroic and narrow-band-pass filters (15 nm). The emission is sent to a confocal cavity (Thorlabs) with a FSR of 10 GHz and a finesse of 150. The transmission through the cavity is detected as the cavity mirror spacing is changed by applying a voltage to the piezo that controls the separation of the cavity mirrors. **b** Color density plot of individual transmission spectra. For each line the cavity separation is ramped linearly to cover the given frequency interval and then ramped back to the initial point. Only one side of the scans are shown. Frequency is calibrated to applied voltage using the known value of the FSR. Counts per 0.1 s are plotted for multiple scans. **c** Average of 40 scans, fitted with a Lorentzian lineshape, indicating an emission FWHM of $\sim$ 80 MHz.

In summary we note that the frequency of the transitions of an NV center remains static under resonant excitation. The frequency of the transitions jump to a random value within the absorption spectrum after a pulse of green excitation. At the moment we do not have enough information as to the timescale in which the charge environment around the NV center reconfigures under green illumination. We find the absorption spectrum measured where intermediate pulses of strong green excitation are used at each repetition of the sequence provides a "worst-case" estimate of the bandwidth of the transition frequencies of the NV center.

2.9 Ionization

For the final section of this chapter we will describe how light fields can change the charge state of the NV center. So far in our exploration of the NV center we only considered the negatively charged (six-electron) states associated with the NV center. This configuration is highly stable, but under continuous optical excitation the NV center can ionize[98, 99]. The level structure is quite different for the neutral configuration of the NV center (NV^0)[100], for example the ZPL is at 575 nm. The low-temperature studies are particularly prone to influence of the different charge states as resonant excitation is charge selective.

As illustrated in Figure 2.16 a time-trace from the NV center under resonant illumination over long times exhibits an exponential decay of the fluorescence. For optical excitation rates above saturation, the decay time is linearly dependent on the optical excitation power[92]. This behavior is consistent with the NV center ionizing by being excited from the orbital excited state to the conduction band, where the

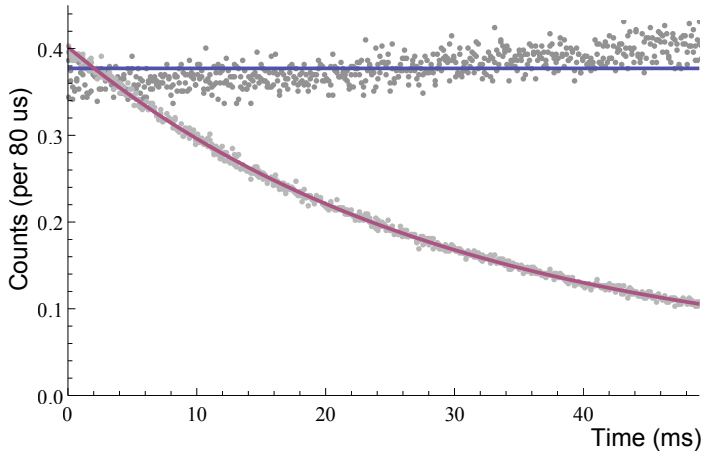

Figure 2.16: Timetrace of the fluorescence from an NV center for long times. The NV center is excited with two lasers resonant to the $|0\rangle$ to $|E_y\rangle$ (1 μW), $|\pm 1\rangle$ to $|A_1\rangle$ (50 nW) under 3 G field to make sure no dark states related to ground state spin levels exist. The fluorescence obtained from the NV center is binned to 80 μs intervals and an average trace of the fluorescence is shown (light gray data points). Red solid line is an exponential fit with a time constant of 29 ms. Dark gray data points and blue solid line are from the same dataset, except post-selection for charge state has been carried out (for details see B).

fluorescence decay indicates the rate of ionization. Once an NV center has gone dark (as a result of the optical drive), it remains in the dark state for many seconds, and only a strong illumination with green light (e.g. saturation power of about 1 mW for 10 μs) seems to bring it back to a configuration that makes sure it responds to the resonant excitation again. This distinct behavior for red and green lasers have been utilized to selectively ionize the NV center even for room temperature experiments[101, 102].

Many low-temperature experiments now include a step that confirms the charge state of the NV center after the experiment is completed (e.g. see Chapter 5,[75],[92]). Data is post-selected and analyzed so that only those experimental runs where fluorescence from the NV center is collected in a time period when excited by resonant lasers. The effect of such a post-selection step is illustrated in Figure 2.16, which removes the exponential decay. This post-selection is also sensitive to frequency fluctuations, mechanical instabilities and other drifts in the system and generally boosts the signal to noise of the experiments, and also selects cases where the NV center gets brighter over time, yielding an overall rise in the counts.

As a final remark we point out that ionization does set an upper limit to the time in which an NV center can be used in a particular transition frequency. As the NV center will ionize after a finite amount of time, a strong green excitation pulse is necessary to bring it back to the correct charge state. The same pulse, or the fact that the NV center has ionized, also effects the charge environment as described in Section 2.8.

This concludes the introductory chapter to the optical properties of the NV center

in diamond. In the subsequent chapters we will use the ideas and tools developed in this chapter to demonstrate spin-photon entanglement, to show quantum interference of single photons from two NV centers and to measure and cool the nuclear spin environment around an NV center.

Chapter 3

Quantum entanglement between an optical photon and a solid-state spin qubit

3.1 Introduction

A quantum network[39] consists of several nodes, each containing a long-lived quantum memory and a small quantum processor, that are connected via entanglement. Its potential applications include long-distance quantum communication and distributed quantum computation[103]. Several recent experiments demonstrated on-chip entanglement of solid-state qubits separated by nanometer[74] to millimeter[104, 105] length scales. However, realization of long-distance entanglement based on solid-state systems coupled to single optical photons[106] is an outstanding challenge. The nitrogen-vacancy (NV) center, a defect in diamond consisting of a substitutional ni-

trogen atom and an adjacent vacancy, is a promising candidate for implementing a quantum node. The ground state of the negatively charged NV center is an electronic spin triplet with a 2.88 GHz zero-field splitting between the $|m_s = 0\rangle$ and $|m_s = \pm 1\rangle$ states (from here on denoted $|0\rangle$ and $|\pm 1\rangle$). With long coherence times[27], fast microwave manipulation, and optical preparation and detection[107], the NV electronic spin presents a promising qubit candidate. Moreover, it can be coupled to nearby nuclear spins that provide exceptional quantum memories and allows for the robust implementation of few-qubit quantum registers[74, 72]. In this work we demonstrate the preparation of quantum entangled states between a single photon and the electronic spin of a NV center:

$$|\Psi\rangle = \frac{1}{\sqrt{2}}(|\sigma_-\rangle\,|+1\rangle + |\sigma_+\rangle\,|-1\rangle), \tag{3.1}$$

where $|\sigma_+\rangle$ and $|\sigma_-\rangle$ are orthogonal circularly polarized single photon states.

The key idea of our experiment is illustrated in Figure 3.1a. The NV center is prepared in a specific excited state ($|A_2\rangle$ in Fig 3.1a) that decays with equal probability into two different long lived spin states ($|\pm 1\rangle$) by the emission of orthogonally polarized optical photons at 637 nm. The entangled state given by Eq. 3.1 is created because photon polarization is uniquely correlated with the final spin state. This entanglement is verified by spin state measurement using a cycling optical transition following the detection of a 637 nm photon of chosen polarization.

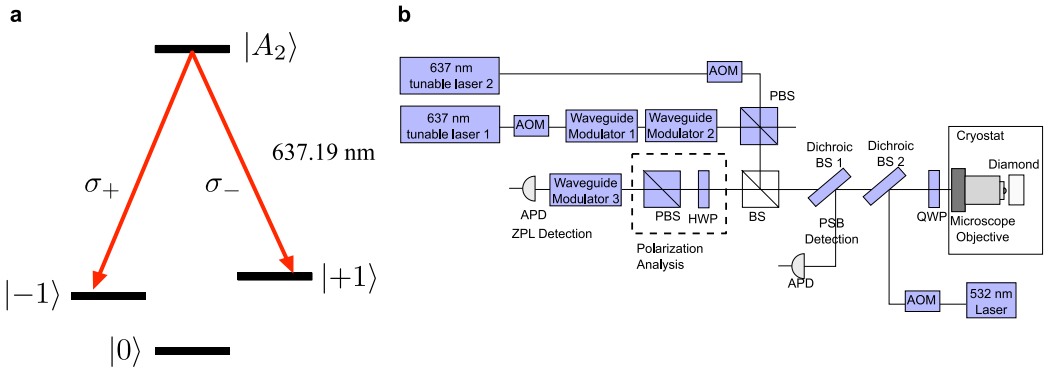

Figure 3.1: Scheme for spin-photon entanglement. **a.** Following selective excitation to the $|A_2\rangle$ state, the Λ system decays to two different spin states through the emission of orthogonally polarized photons, resulting in spin-photon entanglement. **b.** Schematic of the optical setup. Individual NV centers are isolated and addressed optically using a microscope objective. Two resonant lasers at 637 nm and an off resonant laser at 532 nm address various optical transitions. Fluorescence emitted from the NV center is spectrally separated into PSB and ZPL channels, and are detected with APDs. The latter channel contains entangled photons and is sent through a polarization analysis stage.

3.2 Characterization of NV centers

Understanding and controlling excited state properties is a central challenge for achieving such a coherent interface between spin memory and optical photons. In contrast to isolated atoms and ions, solid state systems possess complex excited state properties that depend sensitively on their local environment[94]. Non-axial crystal strain is particularly important to the present realization because it affects the optical transitions' selection rules and polarization properties[108].

In the absence of external strain and electric or magnetic fields, properties of the six electronic excited states are determined by the NV center's C_{3V} symmetry and spin-orbit and spin-spin interactions (shown in Figure 3.2a)[108]. Optical transitions between the ground and excited states are spin preserving, but could change electronic

orbital angular momentum depending on the photon polarization. Two of the excited states, labeled $|E_x\rangle$ and $|E_y\rangle$ according to their orbital symmetry, correspond to the $m_s = 0$ spin projection. Therefore they couple only to the $|0\rangle$ ground state and provide good cycling transitions, suitable for readout of the $|0\rangle$ state population through fluorescence detection. The other four excited states are entangled states of spin and orbital angular momentum. Specifically, the $|A_2\rangle$ state has the form

$$|A_2\rangle = \frac{1}{\sqrt{2}}(|E_-\rangle\,|+1\rangle + |E_+\rangle\,|-1\rangle), \tag{3.2}$$

where $|E_\pm\rangle$ are orbital states with angular momentum projection ± 1 along the NV axis. At the same time, the ground states ($|0\rangle$, $|\pm 1\rangle$) are associated with the orbital state $|E_0\rangle$ with zero projection of angular momentum (for simplicity the spatial part of the wavefunction is not explicitly written). Hence, due to total angular momentum conservation, the $|A_2\rangle$ state decays with equal probability to the $|-1\rangle$ ground state through σ_+ polarized radiation and to $|+1\rangle$ through σ_- polarized radiation.

The inevitable presence of a small strain field, characterized by the strain splitting (Δ_s) of $|E_{x,y}\rangle$, reduces the NV center's symmetry and shifts the energies of the excited state levels according to their orbital wavefunctions. For moderate and high strain, the excited states are separated into two branches and there is mixing between levels[109]. In the upper branch, an energy gap protects $|A_2\rangle$ against low strain and magnetic fields, preserving the polarization properties of its optical transitions. A group theoretical analysis of the excited states and polarization properties of the transitions is detailed in Section 2.3.

To ensure that $|E_y\rangle$ is a good cycling transition and $|A_2\rangle$ acts as an entanglement generation transition as required for the current study, we select a NV center with

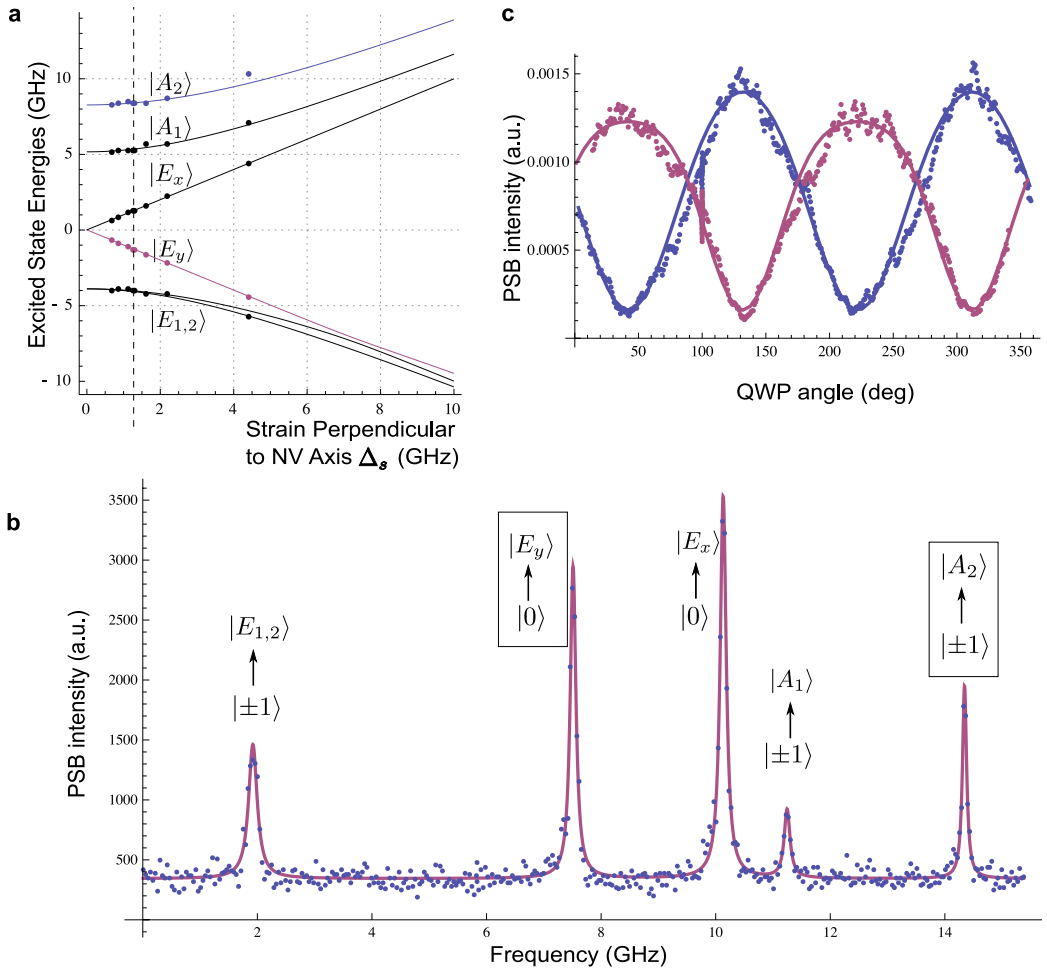

Figure 3.2: Characterization of NV centers. **a.** Energy levels of the NV center under strain. Solid lines are based on a theoretical model from [94] and dots are data from seven NV centers. The dashed line indicates the NV center used in this paper. **b.** Excitation spectrum of the NV center under CW microwave radiation. **c.** Polarization properties of the $|\pm1\rangle \rightarrow |A_2\rangle$ transition in absorption. The system is initially prepared in $|+1\rangle$ (blue) or $|-1\rangle$ (red). We then apply a laser pulse of varying polarization to the $|A_2\rangle$ state while collecting fluorescence. Oscillations with visibility $77 \pm 10\%$ indicate that the transitions linking $|\pm1\rangle$ to $|A_2\rangle$ are circularly polarized and mutually orthogonal (see Appendix A for details).

relatively small strain splitting ($\Delta_s \sim 2 \times 1.28$ GHz). Figure 3.2b presents its excitation spectrum, while Figure 3.2c demonstrates the desired polarization properties of the $|\pm 1\rangle \leftrightarrow |A_2\rangle$ transitions via resonant excitation.

3.3 Experimental demonstration of spin-photon entanglement

We now turn to the experimental demonstration of spin-photon entanglement. Our experimental setup is outlined in Figure 3.1b and described in Appendix A. To create the entangled state, we use coherent emission within the narrow-band zero phonon line (ZPL), which includes only 4% of the NV center's total emission. The remaining optical radiation occurs in the frequency shifted phonon side band (PSB), which is accompanied by phonon emission that deteriorates the spin-photon entanglement[89]. Isolating the weak ZPL emission presents a significant experimental challenge due to strong reflections of the resonant excitation pulse reaching the detector. By exciting the NV center with a circularly polarized 2 ns π pulse that is shorter than the emission timescale, we can use detection timing to separate reflection from fluorescence photons. A combination of confocal rejection, modulators, and finite transmittivity of our optics suppresses the reflections sufficiently to clearly detect the NV center's ZPL emission in a 20 ns region (Figure 3.3).

For photon state determination, ZPL photons in either the $|\sigma_\pm\rangle$ or $|H\rangle = \frac{1}{\sqrt{2}}(|\sigma_+\rangle + |\sigma_-\rangle)$, $|V\rangle = \frac{1}{\sqrt{2}}(|\sigma_+\rangle - |\sigma_-\rangle)$ basis are selected by a polarization analysis stage and detected after an optical path of ~ 2 m. Spin readout then occurs after a 0.5 μs spin

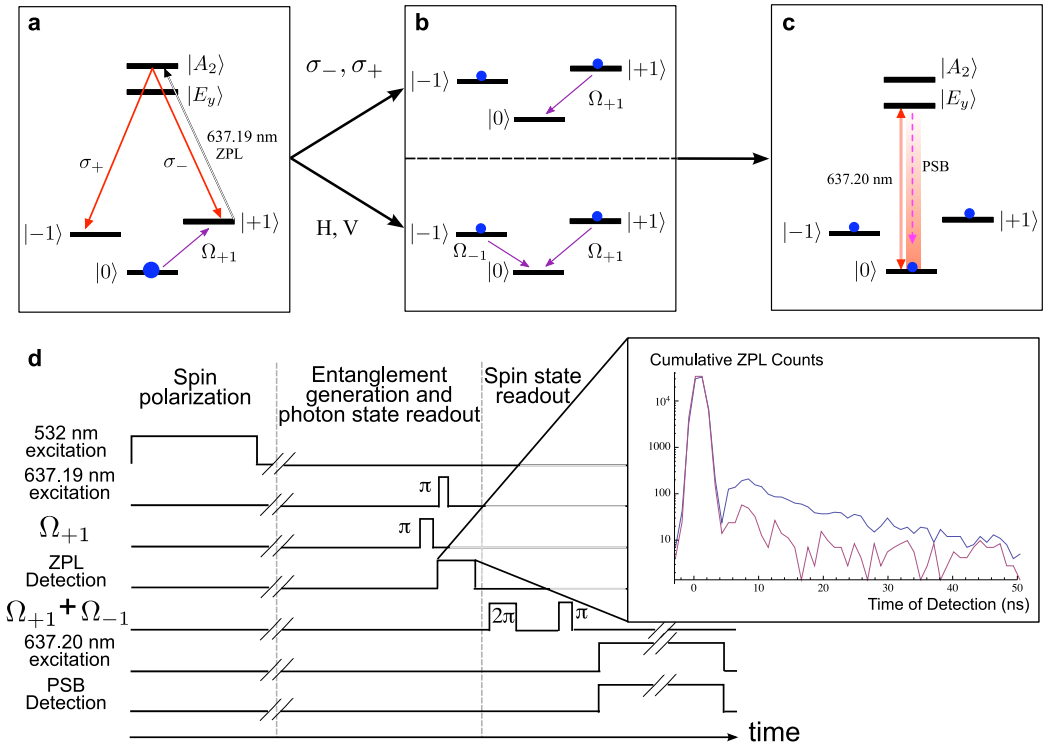

Figure 3.3: Experimental procedure for entanglement generation. **a.** After spin polarization into $|0\rangle$, population is transfered to $|+1\rangle$ by a microwave π pulse (Ω_{+1}). The NV is excited to $|A_2\rangle$ with a 637.19 nm π pulse and the ZPL emission is collected. **b.** If a σ_+ or σ_- photon is detected, the population in $|+1\rangle$ or $|-1\rangle$ is transferred to $|0\rangle$. If a $|H\rangle$ or $|V\rangle$ photon is detected, a $\tau - 2\pi - \tau$ echo sequence (see Appendix A) is applied with Ω_{+1} and Ω_{-1}, followed by a π pulse which transfers the population in $|M\rangle$ (see text) to $|0\rangle$. **c.** The population in $|0\rangle$ is measured using the 637.20 nm optical readout transition. **d.** Pulse sequence for the case where a $|H\rangle$ or $|V\rangle$ ZPL photon is detected (time axis not to scale). If a $\sigma_\pm$ photon is detected instead, only a π pulse on either Ω_{+1} or Ω_{-1} is used for spin readout. Inset: Detection time of ZPL channel photons showing reflection from diamond surface and subsequent NV emission (blue) and background counts (purple).

memory interval following photon detection by transferring population from either the $|\pm 1\rangle$ states or from their appropriately chosen superposition into the $|0\rangle$ state using microwave pulses $\Omega_{\pm 1}$. The pulses selectively address the $|0\rangle \leftrightarrow |\pm 1\rangle$ transitions with resonant frequencies $\omega_{\pm}$ that differ by $\delta\omega = \omega_+ - \omega_- =$122 MHz due to an applied magnetic field. For superpositions of $|\pm 1\rangle$ states an echo sequence is applied before the state transfer to extend the spin coherence time (see Appendix A). The transfer is followed by resonant excitation of the $|0\rangle \leftrightarrow |E_y\rangle$ transition and collection of the PSB fluorescence. We carefully calibrate the transferred population measured in the $|0\rangle$ state using the procedure detailed in Appendix A.

Figure 3.4a shows the populations in the $|\pm 1\rangle$ states, measured conditionally on the detection of a single circularly polarized ZPL photon. Excellent correlations between the photon polarization and NV spin states are observed.

To complete the verification of entanglement, we now show that correlations persist when ZPL photons are detected in a rotated polarization basis. Upon detection of a linearly polarized $|H\rangle$ or $|V\rangle$ photon at time t_d, the entangled state in Eq.3.1 is projected to $|\pm\rangle = \frac{1}{\sqrt{2}}(|+1\rangle \pm |-1\rangle)$, respectively. These states subsequently evolve in time (t) according to

$$|\pm\rangle_t = \frac{1}{\sqrt{2}}\left(e^{-i\omega_+(t-t_d)}|+1\rangle \pm e^{-i\omega_-(t-t_d)}|-1\rangle\right). \tag{3.3}$$

In order to read out the relative phase of superposition states between $|+1\rangle$ and $|-1\rangle$, we use two resonant microwave fields with frequencies ω_+ and ω_- to coherently transfer the state $|M\rangle = \frac{1}{\sqrt{2}}\left(e^{-i\omega_+ t}|+1\rangle + e^{-i(\omega_- t - (\phi_+ - \phi_-))}|-1\rangle\right)$ to $|0\rangle$ (see Figure3.3b), where the initial relative phase $\phi_+ - \phi_-$ is set to the same value for each round of the

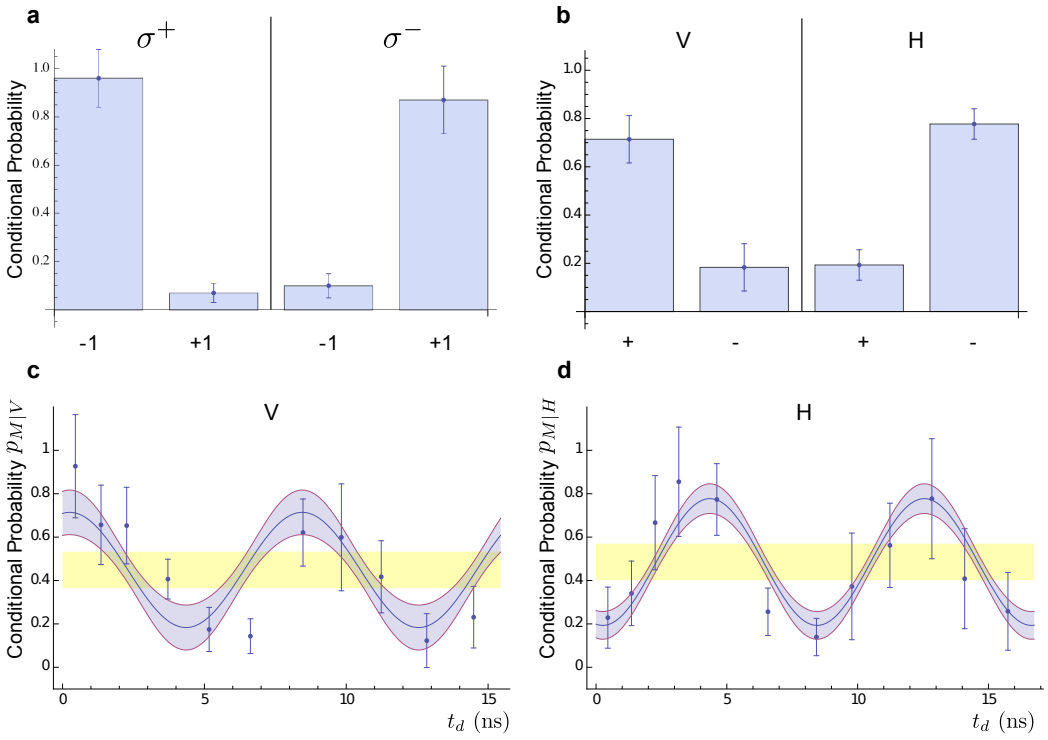

Figure 3.4: Measurement of spin-photon correlations in two bases. **a.** Conditional probability of measuring $|\pm 1\rangle$ after the detection of a $\sigma+$ or $\sigma-$ photon. **b.** Conditional probability of measuring $|\pm\rangle$ after the detection of a H or V photon, extracted from a fit to data shown in (c) and (d). **c&d.** Measured conditional probability of finding the electronic spin in the state $|M\rangle$ after detection of a V (c) or H (d) photon at time t_d. Blue shaded region is the 68% confidence interval for the fit (solid line) to the time-binned data (see Appendix A). Errors on data points are one STD. Combined with the data shown in Figure 3.4(a), oscillations with amplitude outside of the yellow regions result in fidelities greater than 0.5. The visibility of the measured oscillations are 0.59 ± 0.18 (c) and 0.60 ± 0.11 (d).

experiment. Thus, the conditional probability of measuring the state $|M\rangle$ is

$$p_{M|H,V}\left(t_d\right) = \frac{1 \pm \cos\alpha\left(t_d\right)}{2}, \tag{3.4}$$

where $\alpha\left(t_d\right) = \left(\omega_+ - \omega_-\right) t_d + \left(\phi_+ - \phi_-\right)$. Eq. 3.4 indicates that the two conditional probabilities should oscillate with a π phase difference as a function of the photon detection time t_d. This can be understood as follows. In the presence of Zeeman splitting ($\delta\omega \neq 0$) the NV center's spin state is entangled with both the polarization and frequency of the emitted photon. The photon's frequency provides which-path information about its decay. In the spirit of quantum eraser techniques, the detection of $|H\rangle$ or $|V\rangle$ at t_d with high time resolution (~ 300 ps $\ll 1/\delta\omega$) erases the frequency information[38, 32]. When the initial relative phase between the microwave fields $\Omega_{\pm 1}$ is kept constant, the acquired phase difference $(\omega_+ - \omega_-)t_d$ gives rise to oscillations in the conditional probability and produces an effect equivalent to varying the relative phase in the measured superposition, allowing us to verify the coherence of the spin-photon entangled state.

The detection times of ZPL photons are recorded during the experiment without any time gating, which allows us to study spin-photon correlations without reducing the count rate. The resulting data are analyzed in two different ways. First, we time-bin the data and use it to evaluate the conditional probabilities of measuring spin state $|M\rangle$ as a function of $|H\rangle$ or $|V\rangle$ photon detection time (Figures3.4c,d). Off-diagonal elements of the spin-photon density matrix are evaluated from a simultaneous fit to the binned data (see Appendix A). The time bins are chosen to minimize fit uncertainty as described in Appendix A. The resulting conditional probabilities are used to evaluate a lower bound on the entanglement fidelity of $F \geq 0.69 \pm 0.068$,

above the classical limit of 0.5, indicating the preparation of an entangled state.

We further reinforce our analysis using the method of maximum likelihood estimate. As described in Appendix A, this method is applied to raw, un-binned ZPL photon detection and spin measurement data and yields a probability distribution of a lower bound on the fidelity. Consistent with the time-binned approach, we find that our data are described by a near Gaussian probability distribution associated with a fidelity of $F \geq 0.70 \pm 0.070$ (see Figure A.6.2 in Appendix A). Significantly, the cumulative probability distribution directly shows that the measured lower bound on the fidelity is above the classical limit with a probability of 99.7 %.

Several experimental imperfections reduce the observed entanglement fidelity. First, the measured strain and magnetic field slightly mixes $|A_2\rangle$ state with the other excited states. Based on Figure 3.2b, we estimate that $|A_2\rangle$ state imperfection and photon depolarization in the setup together reduce the fidelity by 12 %, the latter being the dominant effect. Imperfections in readout and echo microwave pulses decrease the fidelity by 3 %. Other error sources include finite signal to noise in the ZPL channel (fidelity decrease 11 %), as well as timing jitter (another 4 %). The resulting expected fidelity (73 %) is consistent with our experimental observations. Finally, the entanglement generation succeeds with probability $p \sim 10^{-6}$, which is limited by low collection and detection efficiency as well as the small probability of ZPL emission.

3.4 Conclusions and outlook

Entanglement of pairs of remote quantum registers is one important potential application of the technique described in this Letter[19]. This can be done by coincidence measurements on a pair of photons emitted by two remote NV centers. The key figure of merit for such an entanglement operation over a distance L is proportional to $p^2\frac{\gamma T}{1+\gamma\tau}$, where $\gamma \sim 2\pi \times 15$ MHz is the spontaneous decay rate of the NV center, $\tau = L/c$ is the photon travel time, and T is the memory lifetime. A large figure of merit is critical for applications such as quantum repeaters and entanglement purification protocols. The 0.5 μs spin memory interval in our experiments can be extended to several hundred microseconds using spin echo techniques. Furthermore, by mapping the electronic spin state onto proximal nuclei, T can be extended to hundreds of milliseconds[72]. The key limitation in attaining a large figure of merit is low p. It can be circumvented if optical cavities are utilized, which simultaneously enhances emission into the ZPL and improves collection efficiency through integration with appropriate waveguides. For example, by using a photonic crystal nanocavity[110, 111, 112], the potential rate for spin-spin entanglement generation can be about a MHz for $\tau < 1/\gamma$ and a few Hz for τ corresponding to $L \sim 100$ km, resulting in $p^2\frac{\gamma T}{1+\gamma\tau} \geq 1$. Beyond this specific application, our ability to control interactions between NV centers and quantum light fields demonstrate that quantum optical techniques, such as all-optical spin control, nonlocal entanglement[19] and photon storage[42], can be implemented using long-lived solid-state qubits, paving the way for a wide variety of potential applications in quantum optics and quantum information science.

Chapter 4

Quantum interference of single photons from remote nitrogen-vacancy centers in diamond

4.1 Introduction

The interference of two identical photons impinging on a beamsplitter leads to perfect coalescence where both photons leave through the same output port. This fundamental effect, known as Hong-Ou-Mandel (HOM) interference [41], is a consequence of bosonic statistics for indistinguishable particles. HOM interference has been demonstrated using single photon pairs from parametric down-conversion [113] and delayed photons from a single photon source [114, 115, 116]. HOM interference

has recently drawn attention as a resource for entanglement generation between distinct single-photon emitters and for quantum information science. The effect has been observed for photons emitted by pairs of atoms [117] and trapped ions [118], and has been used for entanglement generation of remote trapped ions [19]. While isolated atoms and ions, which are nominally identical, are a natural source of indistinguishable photons, extending these ideas to condensed matter systems can be challenging since two solid-state emitters are generally distinguishible by effects of their different local environments. This chapter demonstrates quantum interference of two photons produced by nitrogen-vacancy (NV) impurities in distinct diamond samples separated by two meters. Complementing the recent work involving other material systems [119, 120, 121], the present solid-state realization is particularly significant, since electronic and nuclear spins associated with NV centers can be used as a robust solid-state qubit memory, yielding potential scalable architectures for quantum networks [40, 72]. Specifically, in combination with a recent demonstration of spin-photon entanglement [122], the present work paves the way for entanglement generation between remote solid state qubits.

Unlike those associated with atoms in free space, the optical properties of NV centers embedded in a solid state vary substantially from emitter to emitter, especially in distinct samples. This variation is due to the small perturbations in local environment of NV centers and, in particular, due to the local strain. Furthermore, coincidence experiments are limited by the efficiency with which one can collect emission from a single quantum emitter. While a wide variety of approaches are currently being explored to enhance the collection efficiency [123, 124, 125, 126], we here uti-

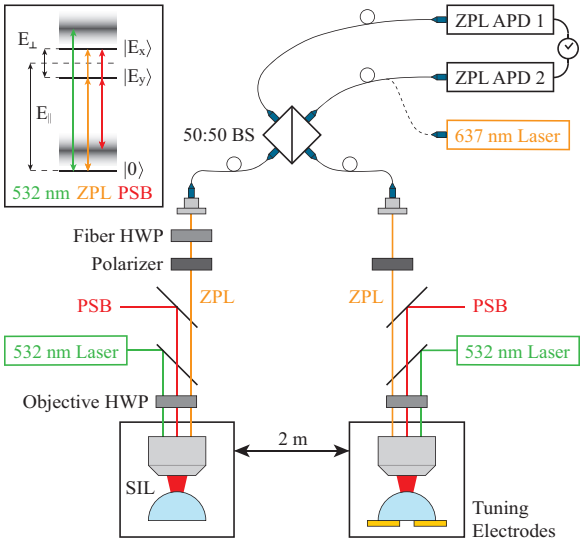

Figure 4.1: Schematic of the apparatus. Two diamond SILs are housed in continuous helium flow cryostats 2 m apart. Each SIL is addressed by a separate confocal microscopy setup, which includes an arm for excitation at 532 nm, a collection arm for the phonon sideband (PSB), and a collection arm for the zero-phonon line (ZPL). The ZPL collection arm is coupled through a half-wave plate (HWP) into a polarization-maintaining optical fiber, which is integrated into a 50:50 fiber beamsplitter. The two beamsplitter output arms are connected to a pair of avalanche photodiodes (APDs), completing the Hanbury Brown and Twiss detection setup. An excitation laser at 637 nm is connected in place of ZPL APD 2 to acquire the absorption scan spectra. Electrodes for electric field tuning are installed in one cryostat. The inset shows a simplified level structure, including non-resonant excitation into the excited state PSB at 532 nm, emission into the ground state PSB, and resonant excitation and emission into the ZPL at 637 nm.

lize solid immersion lenses (SILs) fabricated from bulk diamond [127] to facilitate the efficient collection of narrowband photons with identical properties from distant diamond samples. the SILs improve the collection efficiency in the relevant frequency range by an order of magnitude by minimizing total internal reflection at the air-diamond interface due to the high refractive index ($n_d = 2.4$) of the diamond host. Very recently, microfabricated SILs have been used to observe HOM interference from two NV centers separated by roughly 20 μm on the same diamond chip [128].

In our experiment, we use two 1.0-mm diameter SILs that are fabricated from bulk electronic grade diamond and cut along the (100) crystal plane. The SILs are placed in continuous flow helium cryostats that are separated by two meters, as shown in Fig. 4.1. By performing resonant excitation with an external-cavity diode laser at 637 nm, linewidths in the range of 50-250 MHz were obtained for individual transitions of NV centers in both SILs. These are comparable to narrowest linewidths observed in both synthetic and natural bulk diamond samples.

4.2 Identical photons from two NV centers

To obtain spectrally identical photons from two NV centers, the NV centers need to have transitions that are spectrally overlapping, and the emission from these individual transitions for each NV needs to be isolated. By performing simultaneous absorption scans on NV centers in the two SILs with a single laser, we can directly measure the relative detuning of their optical transitions. In our experimental sequence we use a 5 μs pulse of green light to initialize the NV center into the $|m_s = 0\rangle$ electronic spin sublevel ($|0\rangle$). Therefore, the resonant laser only excites the transitions to the $|\mathrm{E_x}\rangle$ or $|\mathrm{E_y}\rangle$ states, as shown in inset of Fig. 4.1 [83, 88]. We select a pair of NV centers such that either transition in one is nearly resonant with either transition in the other.

For the HOM measurement, we want to collect emission only from the selected pair of resonant transitions and filter emission from the other non-resonant transitions. Since green excitation polarizes the NV center into the $|0\rangle$ state, only the $|0\rangle \leftrightarrow |\mathrm{E_x}\rangle$ and $|0\rangle \leftrightarrow |\mathrm{E_y}\rangle$ transitions need to be considered [79, 28]. The linear and orthogonal

polarization selection rules of the $|0\rangle \leftrightarrow |\mathrm{E_x}\rangle$ and $|0\rangle \leftrightarrow |\mathrm{E_y}\rangle$ transitions allow us to select the emission from one of these transitions by inserting linear polarizers into the ZPL collection arms and setting the Objective HWPs, shown in Fig. 4.1, to the correct angles [78, 80, 89]. Because the ZPL collection used to measure the HOM interference and the resonant excitation used to perform the absorption scans follow the same optical path, we can use the absorption scans to set the correct polarization angle for the ZPL collection. Therefore, we can selectively collect photons emitted from the desired transitions under non-resonant excitation with green light.

We next demonstrate control over the optical properties of NV pairs to compensate for strain-induced spectral inhomogeneities. We make use of the DC Stark effect to actively tune the selected transitions into resonance [93, 95]. Electric fields perpendicular to the NV axis vary the splitting between $|\mathrm{E_x}\rangle$ and $|\mathrm{E_y}\rangle$ states and parallel fields shift both transitions together, as shown in the inset of Fig. 4.1. This allows complete control over the optical transition frequencies [83, 95]. In order to apply the desired electric field, we deposited four electrodes, comprised of 40 nm Au on a Cr sticking layer, on silicon in one of the setups. The gate geometry is shown in Fig. 4.2(a). We applied a bias voltage, V_{app}, on one of the electrodes while keeping the other three grounded. In Fig. 4.2(b), the $|0\rangle \leftrightarrow |\mathrm{E_x}\rangle$ transition of NV1 (blue) is tuned across the $|0\rangle \leftrightarrow |\mathrm{E_x}\rangle$ transition of NV2 (red) by varying the applied voltage V_{app} from -30 V to 50 V. At $V_{\mathrm{app}} = -2.9$ V, shown in Fig. 4.2(c), the detuning between the two transitions is reduced to 25 MHz from an initial value of 270 MHz. We measured linewidths of 85 MHz for NV1, which was tuned, and 217 MHz for NV2, which was not tuned. Similarly, we did not observe a systematic change of the linewidths with

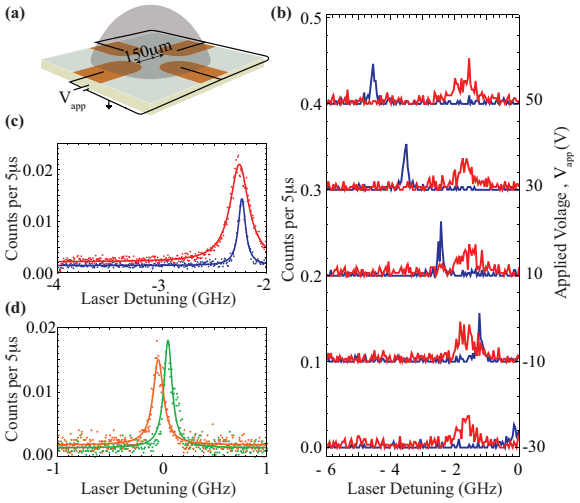

Figure 4.2: Electric field tuning of optical transitions. (a) Four Cr/Au gates deposited on silicon. The central gap has a diameter of 150 μm. In this experiment, only one of the gate voltages was swept while the others were kept grounded. (b) Absorption scans for different applied gate voltages. The gate voltage V_{app} is varied from -30 to 50 V for NV1. The $|0\rangle \leftrightarrow |\text{E}_\text{x}\rangle$ transition of NV1 (blue) is tuned across the $|0\rangle \leftrightarrow |\text{E}_\text{x}\rangle$ transition of NV2 (red). For different V_{app}, absorption scan plots are offset by 0.1 for clarity. (c) Linewidth measurement under electric field tuning. On resonance, the measured linewidths are 85 ± 2 MHz for NV1 (blue) and 217 ± 4 MHz for NV2 (red). The detuning of the optical transitions in two samples is 25 ± 2 MHz. (d) Linewidth measurement for the NV centers used for the HOM measurement. The measured linewidths are 88 ± 3 MHz (green) and 106 ± 4 MHz (orange), and the detuning is 93 ± 10 MHz without electric field tuning.

applied external fields in several other NV centers.

While electric field tuning will be a key feature of future experiments that use resonant excitation (see later), it limits the duty cycle when used in combination with green excitation. Here, the green excitation ionizes charge traps in the diamond lattice [95], and these charge dynamics limit the duty cycle during which we can collect fluorescence at the tuned frequency to half. For this reason, we selected NV centers for the HOM measurement whose transitions, shown in Fig. 4.2(d), are inherently detuned by 93 ± 10 MHz with linewidths of 88 ± 3 MHz and 106 ± 4 MHz, which eliminates the need for electric field tuning and allows us to run the experiment at twice the duty cycle. To confirm that we are addressing single-photon emitters in each SIL, we infer the normalized, second-order autocorrelation function $g^{(2)}_{\mathrm{PSB}}(\tau)$ in a standard Hanbury Brown and Twiss setup by splitting the PSB emission in a 50:50 beamsplitter. We expect $g^{(2)}_{\mathrm{PSB}}(0) = 0$ for an ideal single-photon source, and the single-photon nature of the emission is confirmed in Figs. 4.3(a,b).

4.3 Demonstration of HOM interference from two NV centers

To observe HOM interference we apply CW excitation at 532 nm to the two NV centers whose single emitter autocorrelation functions are shown in Figs. 4.3(a,b). To ensure that the emission from the two NV centers is indistinguishable in frequency, we first spectrally filter the ZPL emission from each NV center and then use polarizers, as described above, to collect only the emission from the selected transition in each NV

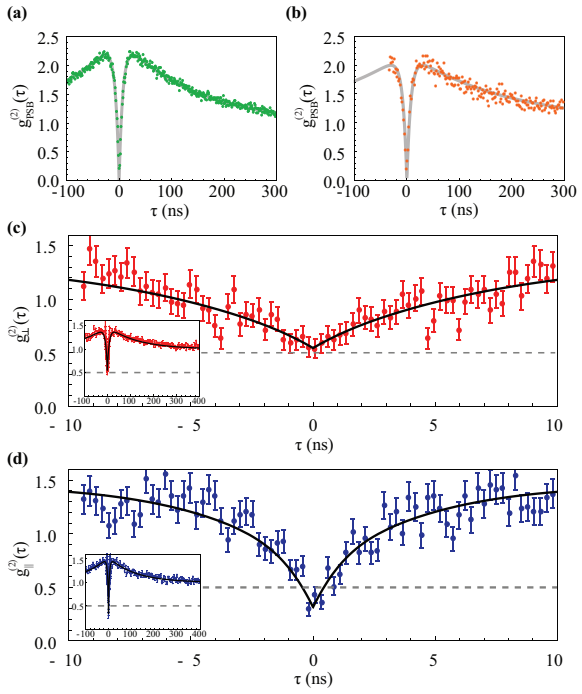

Figure 4.3: (a,b) Single emitter second-order autocorrelation functions, $g^{(2)}_{\mathrm{PSB}}(\tau)$, of the PSB emission, inferred for the two NV centers used for the HOM measurement. (c,d) Demonstration of HOM interference from remote NV centers in the (c) distinguishable case and (d) indistinguishable case. The dashed lines indicate the limit expected from independent distinguishable single photon sources at $\tau = 0$. Solid lines are a fit to the data based on the model described in the text. Error bars are estimated based on shot noise. The data is recorded with 64 ps bins, but for presentation has been binned to 192 ps for $|\tau| < 10$ ns and 3.84 ns bins for $|\tau| > 10$ ns. The data is independently analyzed for both 64 ps bins, and 192 ps bins and the parameter estimates for the fits are in very good agreement.

center. The filtered emission from each NV center is sent to an individual input port of a polarization-maintaining fiber-based beamsplitter. We balance the emission by adjusting the green excitation intensity for each NV center independently to obtain 1100 counts per second (cps) per emitter at each output port of the beamsplitter. An additional half wave plate in one setup is used to adjust the polarization matching of the photons at the beamsplitter. The output ports of the beamsplitter are connected to single photon detectors with timing resolution below 100 ps. The cross-correlation between these detectors is evaluated using a Time-Correlated Single Photon Counting Module with a resolution of 64 ps.

We use the approach described in [119] to analyze the interference data presented in Figs. 4.3(c,d). The expected form of the two-emitter cross-correlation function, $g^{(2)}(\tau)$, is determined by the autocorrelation functions $g^{(2)}_{\mathrm{PSB}}(\tau)$ of the individual emitters, the signal-to-noise ratio, and the degree of distinguishability of photons emitted by the two NV centers. We fix most parameters in our model using independent measurements, as described below, and fit for the visibility of the HOM interference. This visibility, which is extracted from the value of $g^{(2)}(0)$, is a measure of the indistinguishability of the photon pairs. When the photons are distinguishable and the light intensity in both arms is balanced, the correlation measurement will yield $g^{(2)}(0) = 0.5$. Ideally, $g^{(2)}(0) = 0$ for a pair of indistinguishable photons, but the minimal observable $g^{(2)}(0)$ value increases in the presence of experimental noise, as described below. Nonetheless, a measurement of $g^{(2)}(0) < 0.5$ indicates quantum interference between the two single photon sources.

Figures 4.3(c,d) shows $g^{(2)}(0)$ for two different settings of the HWP angle. In

Fig. 4.3(c), the angle is selected such that the emissions from the two NV centers are distinguished by their polarization, yielding $g_{\perp}^{(2)}(0) = 0.52 \pm 0.04$. In Fig. 4.3(d), the photons are indistinguishable when their polarizations are parallel, yielding $g_{||}^{(2)}(0) = 0.34 \pm 0.04$. In terms of the visibility of the HOM interference, defined as $\eta = [g_{\perp}^{(2)}(0) - g_{||}^{(2)}(0)]/g_{\perp}^{(2)}(0)$, we find $\eta = 35 \pm 9\%$. This clearly demonstrate the quantum interference between photons emitted by two NV centers separated by 2 m.

We next turn to the detailed discussion of our experimental observations. We must consider the sources of noise that will cause our result to deviate from the ideal case $g_{||}^{(2)}(0) = 0$. The APD dark counts and fluorescence background from our samples will lead to coincidence events, independent of the emission from the NV centers. Background light and the dark counts of our detectors contribute 80 cps out of the total 1100 cps signal, raising $g_{||}^{(2)}(0)$ to 0.14. Because the NV center spin is not perfectly polarized under green illumination [28], we expect to collect emission from other transitions (e.g. $|A_2\rangle$ to $|m_s = \pm 1\rangle$); since this emission is assumed to be circularly polarized, it is only partially filtered by the polarizer. Emission from other transitions at different frequencies raises the value of $g_{||}^{(2)}(0)$ by 0.07. Finally the polarization-maintaining beamsplitters introduce rotations to the polarization of the emission, which increases the distinguishability of the two photons. This contribution raises the $g_{||}^{(2)}(0)$ value by another 0.07. Considering these factors, we expect experimental imperfections to raise $g_{||}^{(2)}(0)$ value to 0.29, which is in a very good agreement with our experimental observations.

The behavior of the measured $g_{||}^{(2)}(\tau)$ for τ longer than $1/\gamma$, where γ is the inverse lifetime of the emitter, is determined by the autocorrelation functions for the

individual emitters. The behavior of the individual autocorrelation functions for NV centers are determined by the dynamics associated with optical pumping with the 532 nm laser and the decay into and out of the (dark) metastable singlet [57]. The parameters that describe this behavior depend on the optical pumping rate as well as branching ratios of individual NV centers. For the data shown in Figs. 4.3(c,d), this behavior is fit separately for the distinguishable and indistinguishable cases to the same model used to fit the individual autocorrelation functions [57]. The parameters extracted are on the order of those measured for Figs. 4.3(a,b). The small difference between the parameters of Figs. 4.3(a,b) and Figs. 4.3(c,d) can be explained by drifts in laser intensity and focal spot position during the longer integration time used for the datasets shown in Figs. 4.3(c,d).

The HOM interference only occurs within a window around $\tau = 0$ whose width is determined by the bandwidth of the photons emitted from each NV center. In our model, we assume that the emission from the two NV centers is radiatively broadened with bandwidth $\sim \gamma$, and that the center frequencies of the emitted photons are random and different for subsequent emissions. We assume the distribution of the center frequencies is given by the Lorentzian profile that we fit to the absorption spectra shown in Fig. 4.2. Thus the expected average $g_{||}^{(2)}(\tau)$ curve has a $1/e$ fullwidth of 2.4 ns. We find that the estimated width agrees with our measured data.

4.4 Conclusions and outlook

In summary, we have demonstrated the generation of indistinguishable pairs of photons from two spatially separated NV centers. Combined with the recent demon-

stration of entanglement between the electronic spin of an NV center and the polarization of a photon [122], our work paves the way for optically mediated generation of entanglement between remote solid state quantum registers. The techniques demonstrated here have yielded improved collection efficiency, control of the NV centers' optical transition frequencies via electric field tuning, and the ability to operate two independent setups simultaneously over three days of continuous data acquisition. The important figure of merit for an entanglement experiment is the time required to generate an entangled pair with fidelity greater than 50%. Considering the resonant excitation scheme used in [122], and noting that it will likely result in stable, near transform-limited optical linewidths, we find that one entangled spin pair can be created within 12.5 seconds. Improved photon collection techniques that are currently being developed [129] have the potential to increase this generation rate dramatically. Even with the currently estimated rates, though, the exceptionally long nuclear spin memory times of NV centers enable the use of such systems for the realization of solid-state, multi-node quantum networks.

Chapter 5

Laser cooling and real-time measurement of nuclear spin environment of a solid-state qubit

5.1 Introduction

Optical cooling, continuous observation of quantum systems, and feedback control are of fundamental importance for achieving this goal. Coherent population trapping (CPT) is a textbook example of a quantum optical technique that is used to manipulate isolated atomic and molecular systems[6]. Over the past two decades, CPT has been employed for laser cooling of neutral atoms and ions[43], creation of ultracold molecules[44], optical magnetometry[45, 46], and atomic clocks[47], as well as for slowing and stopping light pulses[42]. The electronic spin of the NV center is a promising system for extending these techniques to the solid state. The NV center

has a long-lived spin triplet as its electronic ground state[79], whose $m_s = \pm 1, 0$ sublevels are denoted as $|\pm 1\rangle$ and $|0\rangle$. In pure samples, the electron spin dynamics are governed by interactions with the spin-1 ^{14}N nucleus of the NV center and spin–1/2 ^{13}C nuclei present in 1.1 % natural abundance in the diamond lattice (Fig. 5.1a). Control over nuclear spins[72, 130] is of interest for both fundamental studies and for applications such as nanoscale magnetic sensing [54, 53] and realization of quantum networks[40, 122]. Here we achieve such control via two complimentary methods: effective cooling of nuclear spins through nuclear state selective CPT[48] and conditional preparation based on fast measurements of the nuclear environment and subsequent post-selection[51].

While most prior work involved the use of microwave and RF fields for manipulating both the electronic and nuclear spin states, we utilize all-optical control of the electronic spin[92, 131, 132]. Specifically, we make use of Λ-type level configurations involving the NV center's $|A_1\rangle$ and $|A_2\rangle$ optically excited electronic states and the $|\pm 1\rangle$ ground states (Fig. 5.1a)[122, 83]. At low temperatures (<10 K) and in the limit of zero strain, $|A_1\rangle$ and $|A_2\rangle$ are entangled states of spin and orbital momentum coupled to the $|+1\rangle$ ($|-1\rangle$) state with σ_- ($\sigma+$) circularly polarized light. Correspondingly, excitation with linearly polarized light drives the NV center into a so-called dark superposition state when the two-photon detuning is zero[6]. In the present case the two-photon detuning is determined by the Zeeman splitting between the $|\pm 1\rangle$ states due to the combined effect of the Overhauser field originating from the nuclear spin environment and any externally applied magnetic field[48, 50]. When the external field exactly compensates the Overhauser field, the electronic spin of the

NV center is pumped into the dark state after a few optical cycles and remains in the dark state, resulting in vanishing fluorescence. This is the essence of the dark resonances and CPT.

5.2 Coherent population trapping with NV centers

In our experiments, the $|A_1\rangle$ and $|A_2\rangle$ states are separated by approximately 3 GHz and are addressed individually with a single linearly polarized laser at near zero magnetic field. Since there is a finite branching ratio from the $m_s = \pm 1$ manifold of the electron spin into the $|0\rangle$ state, we use a recycling laser that drives the transition between $|0\rangle$ and the $|E_y\rangle$ excited state, which decays with a small but non-vanishing probability ($\sim 10^{-2}$) back to the $|\pm 1\rangle$ states. Figure 5.1b presents experimental observation of the CPT spectrum as a function of an external magnetic field at three different powers of a laser tuned to the $|\pm 1\rangle \rightarrow |A_2\rangle$ transition. While a broad resonance is observed at high power levels, as the power is reduced, we clearly resolve three features in the spectrum separated by 4.4 MHz, which is two times the hyperfine splitting between three ^{14}N nuclear spin states. This separation corresponds to the magnetic field required to bring the electronic $m_s = \pm 1$ hyperfine states with equal nuclear spin projection ($m_I = \pm 1, 0$) into two-photon resonance.

The dependance of the CPT resonance width upon the laser power, shown in Figure 5.1c, reveals an important role played by repumping on the near-cycling $|0\rangle \leftrightarrow |E_y\rangle$ transition. In contrast to a conventional, closed three-level system, this recycling

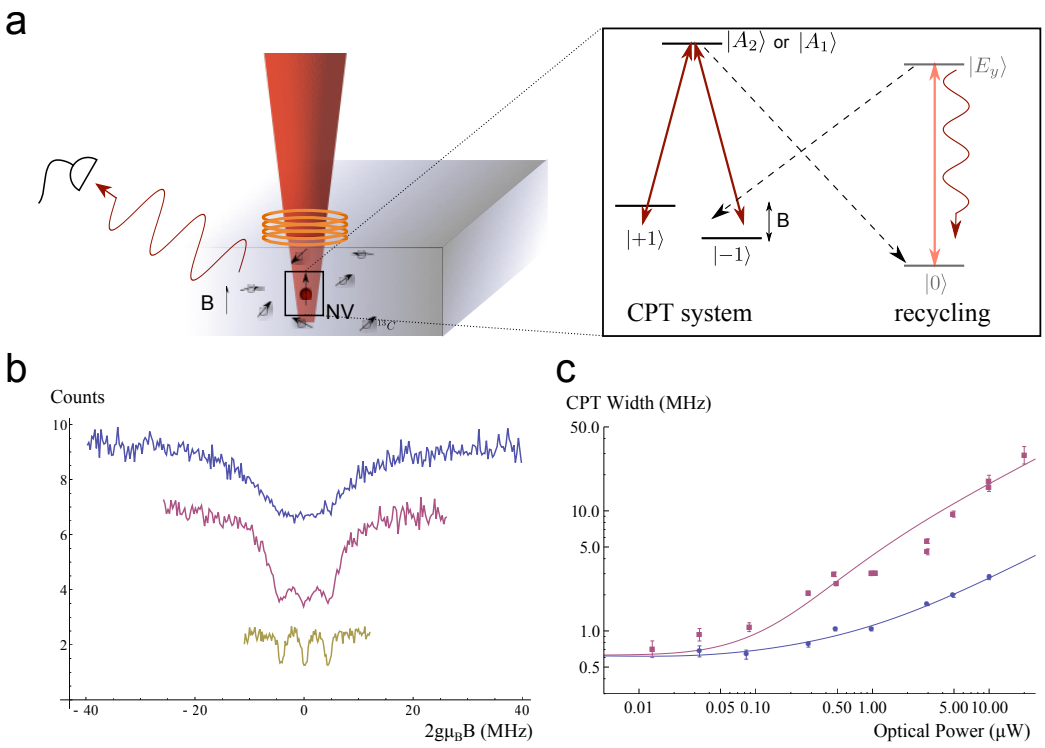

Figure 5.1: Coherent population trapping in NV centers **a.** The Λ-type transitions between the ground states $|\pm 1\rangle$ and excited states $|A_{1,2}\rangle$ of a single NV center are addressed with a CPT laser, while a recycling laser drives the $|0\rangle$ to $|E_y\rangle$ transition. An external magnetic field is applied using a solenoid. **b.** Photon counts from NVa in a 300 μs window are plotted versus the applied field for 10 μW (blue), 3 μW (red), and 0.1 μW (yellow) of laser power addressing the $|A_2\rangle$ state. Blue and red datasets are shifted vertically by 5 and 2 counts for clarity. **c.** Width of individual ^{14}N CPT lines versus CPT laser power when the $|A_1\rangle$ (blue) or $|A_2\rangle$ (red) state is used. Errorbars in all figures show ± 1 s.d. Solid curves represent theoretical model discussed in the main text and Appendix B.

transition can be used to enhance the utility of our CPT system by both decreasing the width of the CPT resonance and increasing the signal to noise ratio. The $|A_1\rangle$ state decays into the $m_s = 0$ ground state through the singlet with a substantial probability of $\sim 40\%$ (see Appendix B). However, the population is returned back into the $m_s = \pm 1$ state from $|E_y\rangle$ only after ~ 100 optical excitation cycles. As a result, away from the two-photon resonance, the NV quickly decays to the $|0\rangle$ state after being excited, where it then scatters many photons through the $|0\rangle \leftrightarrow |E_y\rangle$ cycling transition before returning to the Λ system. If the NV center is not in a dark state, this process effectively increases the number of photons we collect by $2/\eta = \gamma_{s1}/\gamma_{ce}$, where γ_{ce} is the cross transition rate from $|E_y\rangle$ into $|\pm 1\rangle$ and γ_{s1} is the rate from $|A_1\rangle$ to the singlet. The cycling effect also reduces the width of the CPT line since the $|0\rangle \leftrightarrow |E_y\rangle$ transition is quickly saturated away from two-photon resonance, provided that the CPT laser excitation rate exceeds the leakage rate out of recycling transition. Significantly, both of these effects lead to improved sensitivity of dark resonances to small changes in two-photon detuning.

To demonstrate this effect, the widths of dark resonances observed via excitation of $|A_1\rangle$ and $|A_2\rangle$ are compared in Figure 5.1c. Through an independent measurement of the branching ratios (see Appendix B), we determined that $\left|A_{1(2)}\right\rangle$ corresponds to an open (nearly closed) Λ system with $\eta_{A_1} \sim 3.1 \times 10^{-2}$ ($\eta_{A_2} \sim 2.6$). These experimental results are compared with a theoretical model described in Appendix B, which predicts that the resonance linewidth δ_0 is given by $\delta_0 = \sqrt{R_A^2 / \left[1 + \frac{1}{\eta}\left(\frac{R_A}{R_E} + \frac{2R_A}{\gamma}\right)\right]} \sim \sqrt{R_A R_E \eta\gamma/(R_E + \gamma)}$ for small η, where $R_{A(E)}$ corresponds to the optical excitation rate by a laser tuned to the $A(E)$ state and γ is the decay rate of excited states.

The width at low powers is determined by the random magnetic field associated with surrounding ^{13}C nuclear states. When this line broadening mechanism is taken into account (see Appendix B), the experimental results are in excellent agreement with these predictions, plotted as solid lines, showing that a high degree of optical control over the electronic spins of NV center can be achieved.

5.3 Optical cooling and conditional preparation of ^{14}N nuclear spin states

Having resolved the hyperfine coupling between the NV electron and ^{14}N spins, we now demonstrate optical cooling of the nuclear spin states using dark resonances. This method, illustrated in Figure 5.2a, is reminiscent of laser cooling of atomic motion via velocity-selective CPT[43, 48]. A redistribution of the ^{14}N spin state population upon optical excitation takes place because the hyperfine coupling in the excited electronic state of the NV center is enhanced by a factor of $\sim$ 20 compared to the ground state[77]. If the external field is set such that, for example, the $m_I = 0$ hyperfine states are in two photon resonance, only the states with nuclear configuration $m_I = \pm 1$ will be promoted to the excited states, where flip-flops with the electron spin will change the nuclear spin state to $m_I = 0$. When the NV center spontaneously decays into the dark superposition of electronic spin states, optical excitation will cease, resulting in effective polarization (cooling) of nuclear spin into $m_I = 0$ state.

Figure 5.2c presents experimental observation of laser cooling of ^{14}N nuclear spin via CPT. For each point, the pulse sequence shown in Figure 5.2b is applied, where

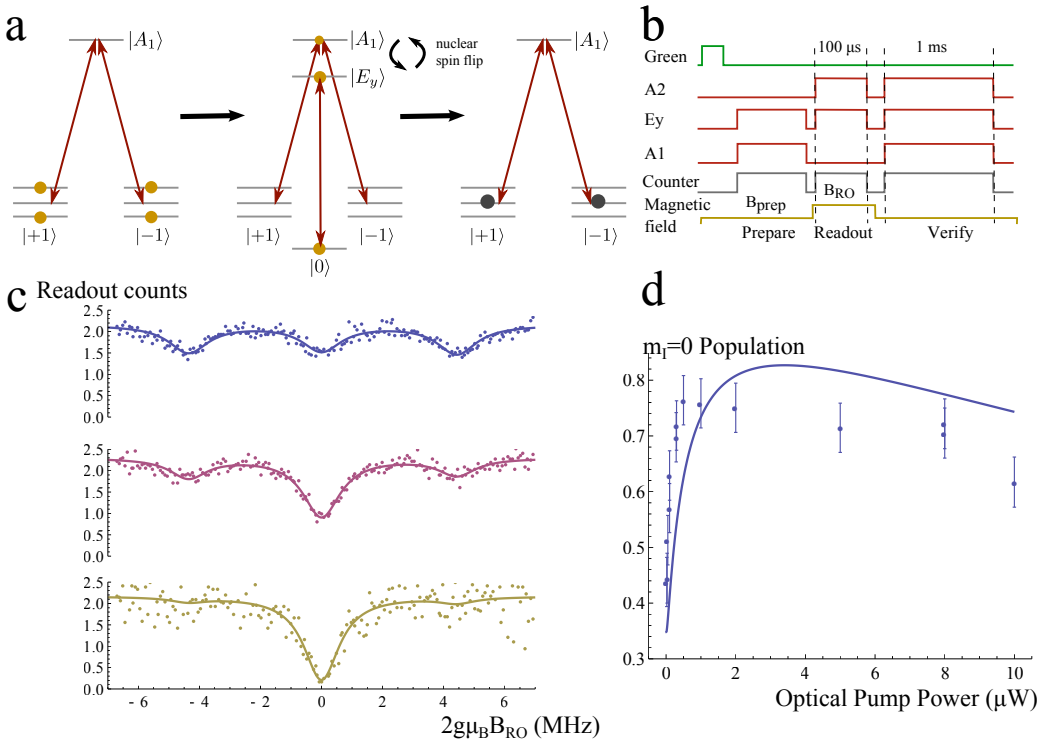

Figure 5.2: Optical control and conditional preparation of the proximal ^{14}N nuclear spin. **a.** Mechanism for optical pumping of ^{14}N states. **b.** Pulse sequence for ^{14}N optical pumping using $|A_1\rangle$ laser and a fixed readout of the prepared state using $|A_2\rangle$ laser. To ensure that the NV was not ionized for all subsequent data runs, we turn on all three lasers at the end of each run so that there is no dark state and only keep data from runs where we obtain a high number of counts during this verification step. **c.** Counts collected with NVa during the readout step versus the readout magnetic field for no preparation step (blue) and preparation with optical pumping using 100 nW of A_1 laser power for 1.9 ms (red). Yellow curve shows the results of ^{14}N polarization via measurement based preparation by selecting the readout events in which the number of counts collected during the last 500 μs of preparation is zero (see Section B.4.2). **d.** Steady-state population in the $m_I = 0$ state after optical pumping for varying powers of A_1 laser, with theoretical model described in Appendix B (solid line).

the magnetic field B_{prep} is kept at 0 during the preparation/optical pumping process, while fluorescence is collected when the field is switched to a particular value of B_{RO}. The increased contrast of the $m_I = 0$ CPT line relative to the other two corresponds to a nuclear spin polarization of $61.5 \pm 4.4\%$. As shown in Figure 5.2d, by optimizing the power of the A_1 laser, we achieve a maximum nuclear polarization of $76.4 \pm 4.4\%$ within a timescale of 353 ± 34 μs. The degree of polarization is likely limited by the escape rate out of the dark state due to off-resonant excitation of the A_2 state and dephasing caused by surrounding ^{13}C nuclei. A simple theoretical model taking into account these two processes and using independently measured parameters (solid line in Fig. 5.2d) reproduces the qualitative features of our experimental results.

We can further improve preparation of the ^{14}N nuclear spin in a desired state via measurement and post-selection, as predicted by theoretical proposals[50, 51, 133]. Specifically, the observation of zero photodetection events during the preparation step at $B_{\text{prep}} = 0$ measures the ^{14}N to be in the $m_I = 0$ state. For instances where such a measurement result is obtained, the nuclear spin populations are subsequently probed and shown in the bottom plot of Figure 5.2c. The resulting ^{14}N polarization of greater than $92 \pm 6\%$ demonstrates that high-fidelity conditional preparation of nuclear spins is possible.

5.4 Observation of instantenous Overhauser field from the ^{13}C spin bath

While the ^{14}N nuclear spin transitions can be spectroscopically resolved and manipulated individually, we next extend our technique to control the many-body environment of the NV center, consisting of ^{13}C nuclei distributed throughout the diamond lattice. The large number of nuclear spin configurations associated with an unpolarized environment results in a random Overhasuer field ($B_{\rm ov}$) with unresolved hyperfine lines. It produces a finite CPT linewidth in measurements that average over all configurations of the ^{13}C spin bath (Figure 5.1b, c).

We now describe how this limitation can be circumvented using fast measurements. The key idea of our approach is to make use of the long correlation time (T_1^{nuc}) associated with evolution of the nuclear bath to observe its instantaneous state and its dynamics. Such a fast measurement is illustrated in Figure 5.3a, where the externally applied field is ramped across a single ^{14}N $m_I = 0$ line while the CPT lasers are on. The yellow curve in Fig. 5.3c shows the lineshape averaged over many experimental runs. At the same time, the intensity plot in Fig. 5.3b shows counts collected in 80 μs time bins during successive individual runs, many of which distinctly show a narrow dark region. Lorentzian fits to selected experimental scans (blue and red curves in Fig. 5.3c) reveal "instantaneous" CPT resonances with linewidths that are over a factor three less than those of the averaged measurement. The motion of the dark line centers (green dots in Figure 5.3b) indicates that the instantaneous field evolves in time.

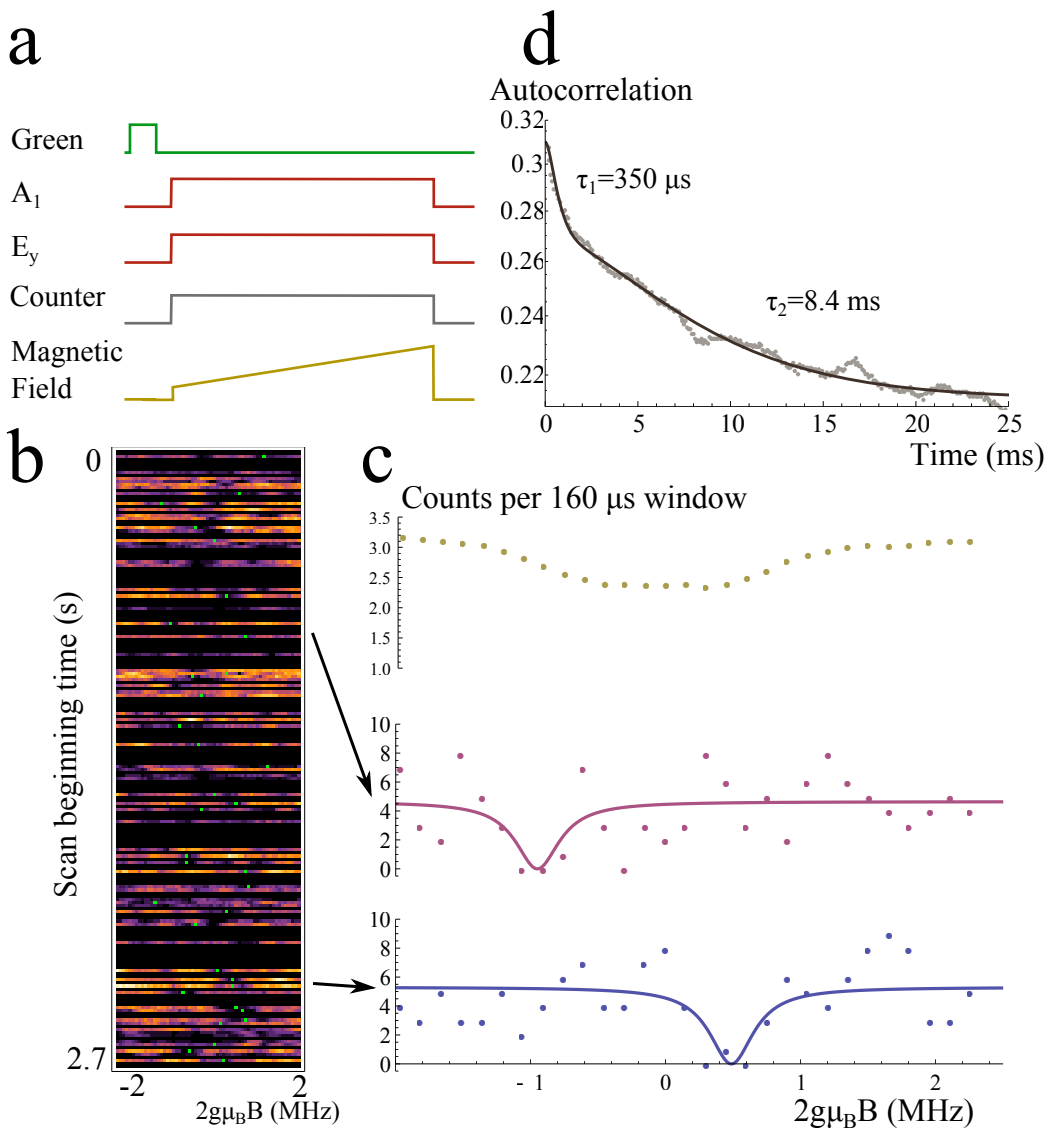

Figure 5.3: Observation of instantaneous Overhauser field from the ^{13}C spin bath. **a.** Pulse sequence for real-time measurement of the ^{13}C nuclear configuration. The applied magnetic field is ramped over a single ^{14}N CPT line over 5 ms while counts are collected in 80 μs bins. **b.** Counts from 200 successive runs are shown on horizontal lines for NVb. Runs where the verification step fails are blacked out. The centers of a constrained Lorentzian fits (Appendix B section 7) to individual runs are indicated with a green dot. **c.** Two such individual runs are shown with their fits (red and blue), along with an average of scans that passed verification (yellow). **d.** Autocorrelation of counts with magnetic field fixed at the $m_I = 1$ ^{14}N line. Fit is to a bi-exponential decay.

In order to provide more quantitative insight into the dynamics of the nuclear environment, we record the fluorescence counts at a fixed value of the external magnetic field with 80 μs time resolution during 50 ms time intervals. The resulting autocorrelation of photon detection events, shown in Fig. 5.3d, clearly reveals two distinct time scales corresponding to $\tau_1 = 350 \pm 30$ μs, consistent with ^{14}N nuclear spin polarization timescale, and $\tau_2 = 8.40 \pm 0.20$ ms. Most significantly, since we can detect dark states of the NV center within 80 μs , these results clearly indicate that reliable measurements of the Overhauser field is possible within its correlation time.

5.5 Measurement-based preparation of ^{13}C spin bath

We now demonstrate how fast measurements can be used to conditionally prepare the ^{13}C environment of the NV center in a desired state with post-selection. We record counts accumulated during both the preparation and readout stages with relatively low power using the sequence shown in Figure 5.4a. Similar to measurement-based preparation of the ^{14}N spin, by conditionally selecting zero photon detection events during preparation step, we can select the states of the ^{13}C environment with vanishing two photon detuning $\delta = 2g\mu_B(B_{\rm prep} + B_{\rm ov}) = 0$, where μ_B is the Bohr magneton. The red curve in Figure 5.4b shows (unconditioned) readout counts recorded following the preparation step, while the blue curve shows the result of measurement-based preparation. The measured width of such a conditionally prepared distribution is significantly smaller than the width corresponding to individual ^{14}N resonances obtained without preparation. We find that while this width depends on $B_{\rm prep}$, the position of the narrow feature follows $B_{\rm prep}$, indicating that we can conditionally prepare the

^{13}C environment via post-selection in a configuration of our choice (Fig. ramp2). The prepared configurations appear to be long-lived both in the dark ($\gg$ 6 ms, Figure B.9) and in the presence of laser light, consistent with autocorrelation measurements ($\tau_2 = 8.4$ ms, Fig. 5.3d).

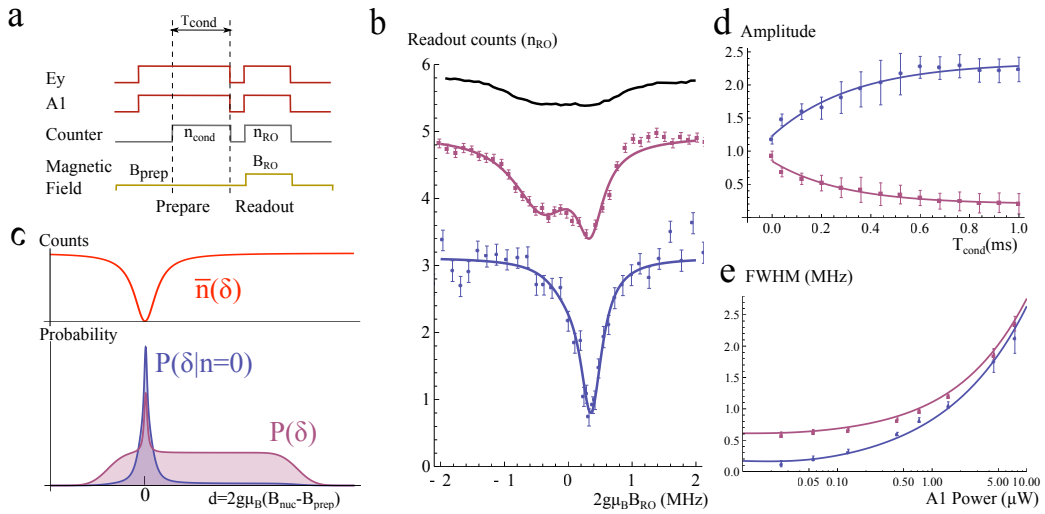

Figure 5.4: Measurement-based preparation of ^{13}C spin bath. **a.** Pulse sequence for preparation and subsequent measurement of the ^{13}C configuration. B_{prep} is set within the central ^{14}N line while B_{RO} is varied to cover all associated ^{13}C states. A preceding green laser pulse and ^{14}N optical pumping step with the A_2 and E_y lasers are not shown. Counts during a conditioning window of length T_{cond} (n_{cond}) at the end of preparation and the readout window (n_{RO}) are recorded for each run. Data presented is an average of many such experimental runs. **b.** n_{RO} for NVb versus B_{RO} is shown in red with double Lorentzian fit. The same dataset analyzed by keeping only events with $n_{\text{cond}} = 0$ is shown in blue. Unprepared ^{13}C distribution from Fig. 5.3 is shown in black for comparison (shifted by 4.3 counts for clarity). **c.** Physics of conditional preparation via measurement. **d.** Amplitude of broad (blue) and narrow (red) distributions versus T_{cond} for NVb. The same dataset was used for each point while the length of the conditioning window was changed in post-processing. **e.** Width of measured ^{13}C distribution with (blue) and without (red) conditional preparation versus A_1 laser power for NVa. Solid lines are theoretical predictions for the readout linewidth δ_0 (blue) and CPT linewidth for the unprepared ^{13}C distribution, same as in Fig. 5.1c (red).

We now discuss the experimental results and explore the limits of our ability to

probe and prepare the ^{13}C environment.

We consider the situation in which the NV center is continuously monitored for a time $T_{\rm cond}$. The average number of photons detected during preparation is given by $\bar{n}(\delta)T_{\rm cond}$, where the photon detection rate $\bar{n}(\delta) = C\delta^2/(\delta_0^2 + \delta^2)$ is related to the instantaneous value of the Overhauser field through the two photon detuning δ (Fig. 4c). The nuclear state probability distribution directly after preparation by conditioning upon obtaining zero counts is $P(\delta|n=0)$, which can be related to the conditional probability of a zero count event $P(n=0|\delta)$ by $P(\delta|n=0) = P(n=0|\delta)\,P(\delta)\,/P(n=0)$, where $P(n), P(\delta)$ are unconditional distributions. For a Poisson distributed random process of photon counts, we find that $P(\delta|\,n=0) \sim \exp(-CT_{\rm cond} \times \delta^2/(\delta_0^2+\delta^2)) \times P(\delta)$. As $T_{\rm cond}$ increases, the range of δ for which we obtain $n=0$ counts due to the existence of a dark state becomes small. At the same time, for large δ, we expect the average number of counts to be high, while the probability of detecting $n=0$ counts due to shot noise is small. This effectively reduces the width of the conditionally prepared nuclear spin distribution.

As illustrated in Fig. 5.4c, conditional measurement prepares an Overhauser field distribution that consists of the broad unconditioned distribution suppressed by $\exp(-CT_{\rm cond})$ and a narrow peak with a width $\delta_c = \sqrt{\ln 2}\delta_0/\sqrt{CT_{\rm cond}}$, where C is the fluorescence rate of the bright state and $T_{\rm cond}$ is the measurement time. The readout step itself has a "resolution" determined by the dark resonance linewidth δ_0. The observed features represent a convolution of the dark resonance probe with the conditionally prepared distribution. For the conditional preparation to be effective, we require that $CT_{cond} > 1$, and therefore $\delta_c < \delta_0$, indicating that the measured

CPT linewidth will be limited by the readout step. Experimentally, we find that our measured lineshapes can be well fitted with the combination of a narrow and a broad Lorentzian distribution whose width and position are mostly independent of photo-detection time T_{cond}. However, as T_{cond} is increased, the relative weight of the narrow distribution increases (Figure 5.4d). This is consistent with the theoretical prediction that the readout-limited narrow resonance width does not depend on T_{cond}, while better discrimination in conditional measurements increases the probability that the nuclear spin state is in the narrow distribution.

Interestingly, we find that even without conditioning (red line Figure 5.4b), a narrow distribution of nuclear spin configurations around B_{prep} is prepared. This modification of the nuclear distribution is a result of CPT-based laser cooling of the ^{13}C bath, consistent with the predictions of Reference [48]. The specific physical mechanism of such cooling likely involves electronic spin dependent evolution of the ^{13}C nuclei, and will be discussed in detail in future studies. We emphasize this observation provides a clear indication that the magnetic environment is affected by the dynamics of the NV, providing direct evidence that the NV spin dynamics is dominated by the Overhauser field rather than external magnetic field fluctuations.

Figure 5.4e shows the dependance of the observed linewidth of the narrow feature on the CPT laser power. At low powers the observed width reaches a minimum value of 104 ± 49 kHz. The limiting width results from the effects of strain splitting of the $|\pm 1\rangle$ states on the readout process at zero magnetic field (see Appendix B for a quantitative discussion of effects of strain)[56]. Due to this splitting, very small magnetic field changes do not shift the energies of $|\pm 1\rangle$ to first order. Therefore our

CPT readout signal becomes insensitive to Zeeman shifts on the order of twice the strain splitting (see Appendix B). In addition, a minimal linewidth of ~ 400 kHz was obtained for measurements performed with a separate NV center (NVb) subject to higher strain.

5.6 Conclusions and outlook

The limit associated with strain splitting can be easily circumvented by using a large external magnetic field to split the $|\pm 1\rangle$ spin states and two laser frequencies to address the NV center in a Raman configuration near zero two-photon detuning. As described in Appendix B, a modest increase in collection efficiency by an order of magnitude[127] would allow us to obtain quantum-limited narrowing of nuclear distribution $\delta_c \sim 1/T_{\mathrm{cond}}$, which, in turn, can be on the order of the inverse lifetime of the given nuclear configuration[48].

The presented experiments open intriguing prospects for using coherent optical techniques to control nuclear spins surrounding quantum emitters. For instance, they can be used to study quantum many-body dynamics of so-called central-spin models in real time, either in isolation or in the presence of dissipation[134]. Specifically, nuclear field diffusion can be explored that, in the presence of CPT lasers, is expected to have very interesting statistical properties reminiscent of Levy flights in VSCPT[135]. Furthermore, the present approach allows for direct application of quantum feedback control to deterministically drive nuclear spins into a desired state. This may be used to prepare non-classical superposition states of the nuclear spins analogous to spin-squeezed states in atomic ensembles[136] and to "engineer" collective dissipation for

nuclear spin ensembles useful for applications in quantum information science, such as long-term storage of quantum states[137]. Finally, our method allows for a new all-optical approach to magnetic sensing[45, 46] that may enable interesting applications in nanoscience[54, 53].

Chapter 6

Conclusion and Outlook

Isolating small quantum systems, and then controllably entangling them with eachother is a challenging goal. Achieving this goal will allow one to realize unique applications such as quantum computation, communication and simulation taking advantage of the distributed, interconnected structure of the resulting quantum networks[39]. Even the prerequisites for this goal, isolation of individual quantum systems, and understanding and engineering their interactions with their environment, is an exciting research area. This thesis summarized a part of the effort on how individual NV center's interactions with light fields can be utilized to isolate, control and then interconnect individual NV centers in diamond.

The results presented in this thesis rely on the understanding of the properties of NV centers and the ability to engineer the host material around the NV center. NV center's optical properties were used to achieve spin-photon entanglement between individual NV centers and single photons (Chapter 3). The optical properties were also used in controlling the nuclear spin environment around the NV center (Chapter

5), which is a step in better understanding and using the interactions of the NV center with its nuclear spin environment. The control over material properties of synthetic diamond, and advances in methods of more efficiently extracting photons from NV centers now allow demonstrations where indistinguishable photons are produced from separate NV centers (Chapter 4 and [128]). These demonstrations pave the way for entangling two separate NV centers that are macroscopically separated via emitted photons. The resulting entangled NV centers can be better controlled, and quantum information can be stored for a longer period of time, using the optical control achievable over the nuclear environment around the NV center.

Useful quantum computation and quantum communication devices require a large number of quantum nodes to be interconnected rapidly and with high fidelity[3]. Scaling the above mentioned demonstrations to a large number of interconnected quantum nodes is still an open challenge.

As an outlook we will consider two basic challenges to achieve this goal of building large, connected quantum networks based on NV centers. The two examples are selected to illustrate challenges for the next generation experiments that will combine results of separate experiments and demonstrations.

We consider an NV center based quantum-network acting as a quantum communication channel, where each node acts as a quantum-repeater[40, 72]. Each node consists of an NV center and its local environment, consisting of a few proximal nuclear spins to the NV center. The few, proximal, nuclear spins that are strongly coupled to the NV center are chosen such that their states can be manipulated via the NV center[72, 74]. These nuclear spins are the qubits where information is stored

and manipulated. The entanglement between separate nodes is created via the photons emitted by the NV centers using heralded entanglement protocols. Hence the NV center acts as the communication qubit in each quantum node, connecting it to other nodes and allowing access to the nuclear spins.

The first challenge involves maintaining the integrity of the information stored in nuclear spins while NV centers are being entangled. The second challenge is ensuring separate nodes can be entangled rapidly before the quantum information stored in the nodes is lost due to decoherence.

In this architecture entanglement between separate nodes need to be established while information stored in the same node remains unaffected. For probabilistic entanglement schemes, such as those using emitted photons, this implies that the entanglement generation scheme (excitation to the excited state) does not perturb the memory available in the node (nuclear spins).

As room temperature[138, 130] and CPT based experiments (Chapter 5) demonstrate optical excitation of an NV center to its excited state affects the state of nuclear spins proximal to the NV center. For room temperature experiments, the depolarization of nuclear spins under optical illumination results from the different hyperfine interactions of the different electronic states that are stochastically populated via the optical excitation[138]. This leads to an effective stochastic magnetic field caused by the electronic spin that depolarizes the nuclear spins. In low temperature experiments selective excitation to individual electronic states are possible. Hence, its possible to better control the magnetic field at the nuclear spins caused by the electronic spin. In fact for the nuclear polarization observed in CPT based experiments are believed

to be caused by the electronic spin dependent dynamics of the proximal ^{13}C nuclear spins. Further studies will be required to determine the exact mechanism that leads to nuclear-spin polarization via optical fields[48, 135] and to find the procedure to minimally disturb the nuclear spins around the NV center. This procedure will increase the possible number of attempts to probabilistically generate entanglement between NV centers before the information stored in the nuclear spins is lost, but the associated timescale is finally limited by the coherence times of the nuclear spins.

Since the entanglement generation rate currently is limited by the number of photons collected from NV centers, increasing the collection efficiency is an essential step to more useful devices. At the moment there is a strong push by many groups to use photonic devices to better harness the light from NV centers (for a recent review see [129]). These devices, in the context of the NV center, are interesting also since they will, for example, produce more efficient single photon sources, more sensitive magnetic field sensors, higher spin-photon entanglement fidelities (Chapter 3), and access to faster nuclear spin dynamics (Chapter 5).

The impressive demonstrations in combining nanophotonic structures with NV centers so far have mostly been carried out with broad emissions from NV centers (e.g. [123, 139, 140, 141, 142]) . The task of controllably changing material environment around the NV center to form the nano-photonic structures while keeping the charge and strain environment free of imperfections which stop individual optical lines from being accessible is a topic of current research. The next few years will be an exciting time when nanophotonic devices will dramatically change the landscape of possible experiments using NV centers, for example achieving strong coupling of NV centers

with localized cavity modes should be possible[143].

NV center's allure has been its ability to combine good spin properties with its optical transitions. This combination makes it an interesting candidate for quantum network applications and an NV center based realization of a quantum network appears to be within reach. However, the NV center is far from an ideal system. For particular applications other defects in diamond might be more suitable. For example for single photon sources e.g. nickel centers[144], or silicon vacancies[145] exhibit both higher Debye-Waller factors (more emission into ZPL) as well as shorter excited state lifetimes. Further studies may eventually allow us to find a system with even better properties for quantum networking applications. The UCSB group has recently applied the basic properties of the NV center in diamond as a search criterion for finding other suitable defects in other host materials[146], with interesting results with di-vacancies in silicon-carbide[147]. We expect that techniques developed in this thesis may be used to control such new systems as well.

Appendix A

Supporting material for Chapter 3

A.1 Calculation of entanglement fidelity

To estimate the entanglement fidelity, we first use the conditional measurement shown in Figure 3.4a,b to determine diagonal elements of the spin-photon density matrix in the $|\sigma_\pm\rangle, |\pm 1\rangle$ basis. Since $\sigma_\pm$ photons are emitted with equal probability (see SI), we find $\rho_{\sigma_+ -1,\sigma_+ -1} = \frac{1}{2} p_{-1|\sigma_+} = \frac{1}{2}(0.96 \pm 0.12)$, $\rho_{\sigma_+ +1,\sigma_+ +1} = \frac{1}{2}(0.07 \pm 0.04)$, $\rho_{\sigma_- -1,\sigma_- -1} = \frac{1}{2}(0.10 \pm 0.05)$, and $\rho_{\sigma_- +1,\sigma_- +1} = \frac{1}{2}(0.87 \pm 0.14)$. To evaluate the off-diagonal elements, we rotate the measurement basis by projecting the photon to the $|H\rangle$ or $|V\rangle$ states and measuring the conditional probability of being in state‘ $|M\rangle$, which is equal to $|\pm\rangle$ for particular choices of α (e.g. $|+\rangle = |M\rangle|_{\alpha=0}$). The required diagonal matrix elements in the $|H\rangle, |V\rangle, |\pm\rangle$ basis are then given by $\rho_{V+,V+} = \frac{1}{2} p_{M|V}(\alpha = 0)$, and similarly for $\rho_{H+,H+}, \rho_{H-,H-}$, and $\rho_{V-,V-}$. We model the experimentally measured conditional probabilities with the forms $p_{M|H} = (b_H + a_H \cos\alpha)/2$ and $p_{M|V} = (b_V - a_V \cos\alpha)/2$, where $b_{H,V}$ are the offsets of the oscillations and

$a_{H,V}$ are their amplitudes. Using a simultaneous fit to the data in Figure 3.4c, d that constrains the frequency to be the Zeeman splitting, we obtain the values $\rho_{V+,V+} - \rho_{V-,V-} = a_V/2 = \frac{1}{2}(0.53 \pm 0.16)$, $\rho_{H-,H-} - \rho_{H+,H+} = a_H/2 = \frac{1}{2}(0.58 \pm 0.10)$ The information obtained is sufficient to provide a lower bound for the entanglement fidelity. Using the analysis in [30]:

$$\begin{aligned} F \;\geq\; & \frac{1}{2}(\rho_{\sigma_+ -1,\sigma_+ -1} + \rho_{\sigma_- +1,\sigma_- +1} - 2\sqrt{\rho_{\sigma_+ +1,\sigma_+ +1}\rho_{\sigma_- -1,\sigma_- -1}} \\ & + \rho_{V+,V+} - \rho_{V-,V-} + \rho_{H-,H-} - \rho_{H+,H+}) \end{aligned}$$

we find $F \geq 0.69 \pm 0.068$. This analysis agrees with the results of an independent maximum likelihood analysis described in the SI, which yields a near Gaussian probability distribution for a lower bound on the fidelity with $F \geq 0.70 \pm 0.070$.

A.2 Supplementary methods

A.2.1 Overview of experimental setup

Our experiments are performed using a natural bulk diamond sample kept below 7 K. A Nikon 0.95 NA microscope objective is used in our confocal setup to address individual NV centers. Resonant excitation of the readout and entanglement generation transitions are done using two external cavity diode lasers. To overcome the main experimental challenge of ensuring sufficient signal to noise of the detected ZPL emission, we eliminate background from laser light reflected off the diamond surface by creating an isolated excitation π pulse using two cascaded waveguide modulators. This excitation pulse is sent through a quarter-wave plate that is fixed during all experimental runs to produce the circular polarization that most efficiently excites the

NV to the $|A_2\rangle$ state. We note that, since our measurements are conditioned on the detection of an emitted photon, optical π pulse imperfections only affect the efficiency of the entanglement generation and not the measured fidelity. In the collection path, the ZPL is sent to a polarization analysis setup consisting of a half-wave plate and a polarizing beamsplitter for photon state selection. It then passes through a narrow frequency filter before being detected by a low dark count APD. We use a waveguide based electro-optical modulator before the APD to further reduce reflections of the excitation pulse and suppress detector afterpulsing. Special care is taken to minimize reflections during the measurement window to around the dark count level of the detector.

Addressing of the $|0\rangle \leftrightarrow |\pm 1\rangle$ microwave transitions is carried out using a 15 μm copper wire attached to the diamond. For simultaneous addressing, two microwave fields generated by mixing the difference frequency of the two transitions with their average frequency are separated using bandpass filters, individually attenuated, and recombined to balance their power. Low shot-to-shot noise in the microwave fields' relative phase is crucial. This is achieved by triggering all timing-sensitive channels from one output event of a controller device that produces the entanglement generation and conditioned readout sequences. Timing information of both ZPL and PSB photons are collected by combining them at the input of a time-tagged-single-photon-counting device.

Given an experiment repetition rate of ~ 100 kHz and an entanglement generation success probability of $p \sim 10^{-6}$, we then detect on average one signal photon every few seconds. Since the microwave π pulses used for population transfer to the

$|0\rangle$ state are nearly perfect and about 100 repetitions are required for reliable spin state determination, roughly 24 hours of data taking were required for each of the four photon polarizations measured. Overall, characterization, calibration, and data acquisition for a given NV center were performed over a roughly two month period. The overall measurement time for each individual NV center is limited by the long term mechanical stability of the setup.

A.2.2 Optical setup

We carry out our experiments in a home-built cryogenic confocal setup. Our bulk diamond sample, a natural type IIb diamond of high purity, is kept below 7 K in a Janis ST-500 Cryostat. Optical access to individual NV centers is facilitated with a Nikon 0.95 NA Plan-Apo microscope objective that is held inside vacuum with a bellow structure that allows the objective to be moved relative to the sample. Our microscope contains two excitation channels and two collection channels. The NV is off-resonantly excited and spin polarized using a doubled YAG laser (532 nm Coherent Compass 315M-100) modulated with an acousto-optical modulator (Isomet 1250C-848). Resonant optical pumping is carried out with two external cavity grating lasers. A New Focus Velocity TLB 6304 laser operating at 637.199 nm and locked to a Fabry-Perot cavity (Atrix Management S A CC - 3.0GHz - 200) is used for the readout transitions (~ 4 μW before objective), while a second laser (Atrix Management S A ECLD-0638-022) operating at 637.189 nm is used for resonant optical pumping of the entanglement generation transition (~ 100 μW before objective). Both lasers are modulated with acousto-optical modulators (Crystal Tech 3080-122). In addition,

a high fidelity excitation pulse (2 ns 3dB width and $>$ 50 dB extinction in 4 ns from peak) is generated from the 637.189 nm laser using two waveguide modulators in cascade (Guided Color Technologies), each controlled by an 800 MHz arbitrary waveform generator (Analogic Polynomial Waveform Synthesizer 2045). Extinction of the excitation pulse is critical because we use the relatively long lifetime of the NV center to seperate the emission from the shorter (2ns) laser reflection photons.

Phonon-sideband emission from the NV is separated by dichroic filters from the 532 nm excitation path (Semrock LPD01-532RS-25) and ZPL path (Semrock Di01-R635-25x35) before being filtered to remove any leakage or dominant raman lines (2x Semrock NF01-633U-25, Semrock LP01-633RS-25). It is then coupled into a single mode fiber and sent to a high quantum efficiency APD (SPCM ARQ-15-FC). The ZPL collection path is separated from the resonant excitation path by a non-polarizing beam splitter, and emission from the NV is sent to a polarization analysis setup consisting of a HWP and a PBS. The emission is filtered by two narrow frequency filters (custom Andover 1 nm bandpass around 638 nm, Semrock FF01-640/14-25) and detected by a low-dark count APD (Micro-Photon-Devices, PDM Series). We use a third waveguide based E-O modulator (EOSpace, driven by Stanford Research Systems DG645 delay generator) before the detector to reduce the number of reflected photons from the excitation pulse and suppress afterpulsing of the detector.

A.2.3 Microwave control

The two microwave transitions are addressed individually by separate oscillators: a HP 8350B sweep oscillator with 83525A RF plugin tuned to 2.9387 GHz and an Ag-

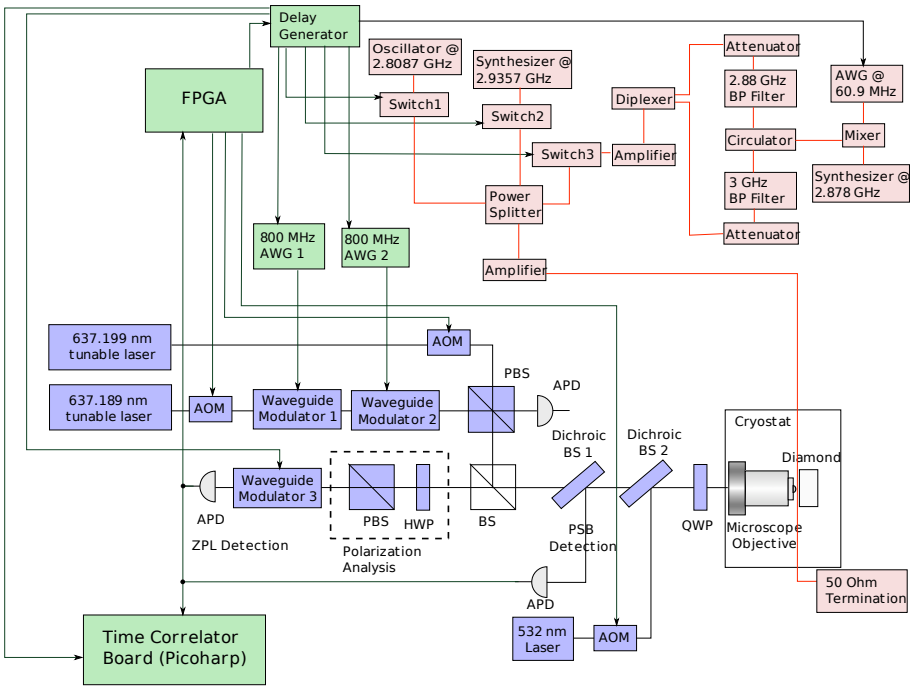

Figure A.1: **Experimental Setup.** The setup is shown in three functional groups. The optical setup is show in blue and gray. In green are the control electronics and the electrical pulses that are generated. A green arrowed line indicates a pulse being generated by the source device and sent to the entity indicated by the arrow. For example the FPGA generates the pulse that drives the AOM for 637.199 nm readout laser. The microwave components and their connections are shown in red.

ilent 83732B synthesizer tuned to 2.8174 GHz. For simultaneous addressing, a 60.85 MHz waveform generated by a high speed Tek 710 AWG is mixed using a Minicircuits ZFM-15 mixer with the RF field generated from the Agilent synthesizer at 2.87875 GHz. To balance the power of the two microwave frequencies of the simultaneous field, they are first separated using two bandpass filters with 120 MHz bandwidth around 2.8 GHz and 3.0 GHz (Reactel 5C7-2800-120S11 and 5C7-3000-120S11). They are then recombined using a diplexer around the same frequencies (Reactel 2DP7-2800/3000-X120S11) after being individually attenuated (Minicircuits ZX76-15R5-PP-S+) and

re-amplified (Minicircuits ZX-60-6013E+). The measured variance in the relative phase between two frequencies of the simultaneous field is below 0.19 radians. Fast microwave switches (Minicircuits ZASWA-2-50DR+, Custom Microwave Components S0947A-C2) are used for time shaping of microwave pulses. All separate channels are combined and sent to a 10 W solid state amplifier (Ophir 530324-002) before the copper wire.

A.2.4 Experiment control and data acquisition

Experimental flow is controlled by a NI-7833R FPGA based intelligent DAQ device programmed to run the entanglement generation sequence and switch to the readout sequence within three clock cycles (75ns) upon the detection of a ZPL photon. Time of arrival information of photons on both PSB and ZPL channels are collected by passively combining the output of the two APDs to the input of a time-tagged-single-photon-counting device (Picoharp 300). The device is configured to record the time of arrival of all detection events relative to a trigger event marking the beginning of the experimental sequence. Further processing of the data is done after each experimental run to determine the number of relevant ZPL and readout events. All channels / events that are timing-sensitive (e.g. trigger to the AWG or trigger to the timing board) are generated from a single output event of the FPGA device that triggers the Stanford DG645 signal generators running in burst mode, which have low channel-to-channel and low trigger-to-output jitter.

An additional multi- function DAQ device from NI is used to find and characterize the NVs. It is also used to record a second electronic copy of the photon arrival event

on the PSB channel to track the position and frequency drift of the NV/ crysotat/laser system while the entanglement experiment is running.

Finally, we point out that the overall time required for finding and characterizing a low-strain NV is several weeks. Combined with the four day-long data acquisition runs for entanglement verification, the amount of data we are able to take for the same NV becomes limited by the long term stability of our setup. Further improving the robustness of the setup and our ability to locate particular NV's over long time periods will be crucial for future experiments.

A.3 Spin readout

In a very similar method to that described in Section 2, we determine the spin of the NV center by resonantly exciting the $|0\rangle \leftrightarrow |E_y\rangle$ transition and collecting emission on the PSB within a 10 μs window. Here, we provide a slightly different presentation of the same data to illucidate the details of the callibration procedure.

To obtain accurate readout levels relevant for calibration of our experimental data, we effectively project the state of the NV center into $|0\rangle$ or $|\pm 1\rangle$ prior to spin measurement by detecting a PSB photon after exciting to the $|E_y\rangle$ or $|A_2\rangle$ state, respectively. Subsequent readout produces a maximum number of 0.11 ± 0.0022 counts/shot when the NV is initially in the $|0\rangle$ state and a minimum number (consistent with background) when it is in the $|\pm 1\rangle$ states. These levels are then used to calculate the populations measured for entanglement verification. Compared to conventional spin measurements in NV centers, this method is less sensitive to effects such as imperfect initial spin polarization, NV photo-ionization, and spectral or spatial instabilities. A

detailed description of the spin readout measurement and calibration is given next.

Spin readout is achieved through resonant laser excitation tuned to the $|0\rangle \leftrightarrow |E_y\rangle$ transition[88]. As the $|0\rangle \leftrightarrow |E_y\rangle$ transition is cycling for low strain and is isolated in frequency from other transitions the fluorescence collected in the presence of the resonant laser field should be proportional to the population in the $|0\rangle$ state. However, the fluorescence levels measured for different spin states may depend on the complex dynamics associated with the singlet state, imperfections of the cycling transition, photoionization, and spatial stability of the measurement setup. In order to accurately calibrate our spin measurements, we use a procedure that involves the conditional preparation of spin states. In the following section, we first describe the conventional spin measurement procedure and then compare it to our conditional readout scheme.

Figure A.3(a) shows microwave Rabi oscillations detected using the conventional resonant readout scheme. Following a polarization step carried out with a green laser, a microwave pulse of varying length and resonant to the $|0\rangle \leftrightarrow |1\rangle$ transition is applied and the resulting state is read out using the resonant excitation. In an ideal preparation and readout scenario, the $|0\rangle$ state would be bright while the $|\pm1\rangle$ states would be completely dark. The high level of fluorescence achieved for the $|0\rangle$ state is limited by the branching ratio between the $|E_y\rangle \rightarrow |0\rangle$ and $|E_y\rangle \rightarrow |\pm1\rangle$ transitions ($\sim$99 % as measured below) and the collection efficiency to about 0.11 counts per shot. Thus multiple repetitions of the experiment are needed to build up enough statistics for an accurate estimation of the initial state. When the NV center is nominally prepared in the $|+1\rangle$ state, we observe counts above the background level, which may be due to imperfect spin polarization or additional fluorescence from the $|+1\rangle$ state.

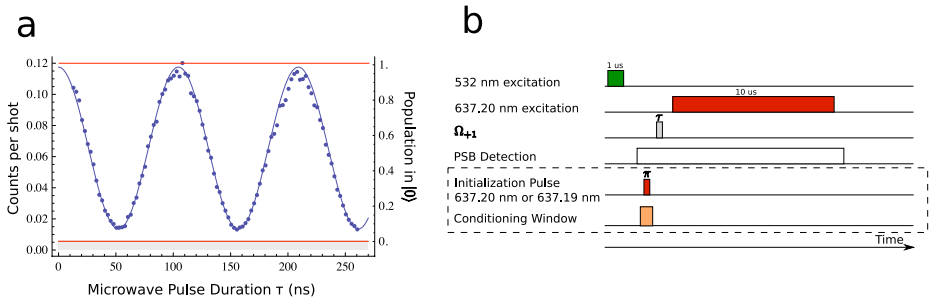

Figure A.2: **Spin readout via resonant excitation a** Microwave Rabi oscillations (in blue) recorded using the pulse sequence given in (b) without conditioning. Left vertical axis shows the average number of counts received for a particular length of microwave pulse duration (τ). Right vertical axis shows the normalized population in the $|0\rangle$ state for the same pulse duration. The red lines are maximum and minimum readout levels obtained using the conditioned readout technique shown in (b) and described in the text. **b** Pulse sequence used for part (a). In the unconditioned case, 532 nm light is turned on for 1 μs to polarize the electronic spin to $|0\rangle$ state. After 6 μs, a microwave pulse resonant to the $|0\rangle \leftrightarrow |+1\rangle$ of varying duration is applied. Finally a 10 μs light pulse resonant to the $|0\rangle \leftrightarrow |E_y\rangle$ transition is turned on 1 μs after the microwave pulse and counts in the PSB are recorded in this interval. Additional pulses used for conditioned readout are boxed, including a resonant optical π pulse tuned to the $|0\rangle \leftrightarrow |E_y\rangle$ or $|\pm\rangle \leftrightarrow |A_2\rangle$ transition. Only events where a PSB photon is received within a 20 ns window around this pulse are kept, thus conditioning the readout procedure on a fluorescent decay from the NV.

To characterize these effects further, we record time traces of the fluorescence during the resonant readout stage where the state is initialized either in $|0\rangle$ or $|1\rangle$ in the same way as the Rabi experiment (Figure A.3(b)). These are then compared to a model of the NV center dynamics similar to the one discussed in [108] and illustrated in Figure A.3(c). The model involves the $|0\rangle$ and $|\pm1\rangle$ ground states, the $|E_y\rangle$ state, and a metastable singlet state $|S\rangle$. The branching ratios from $|E_y\rangle$ state to $|0\rangle$, $|\pm\rangle$, and $|S\rangle$ are related to the decay rates $\gamma_{00} = 1/12$ns, γ_{01}, and γ_{0s}, respectively. γ_{00} is determined by lifetime measurements, and the singlet decay rate to $|0\rangle$ is set to $\gamma_s = \gamma_{00}/33$, as given in [108]. We then simulate the evolution of the system under

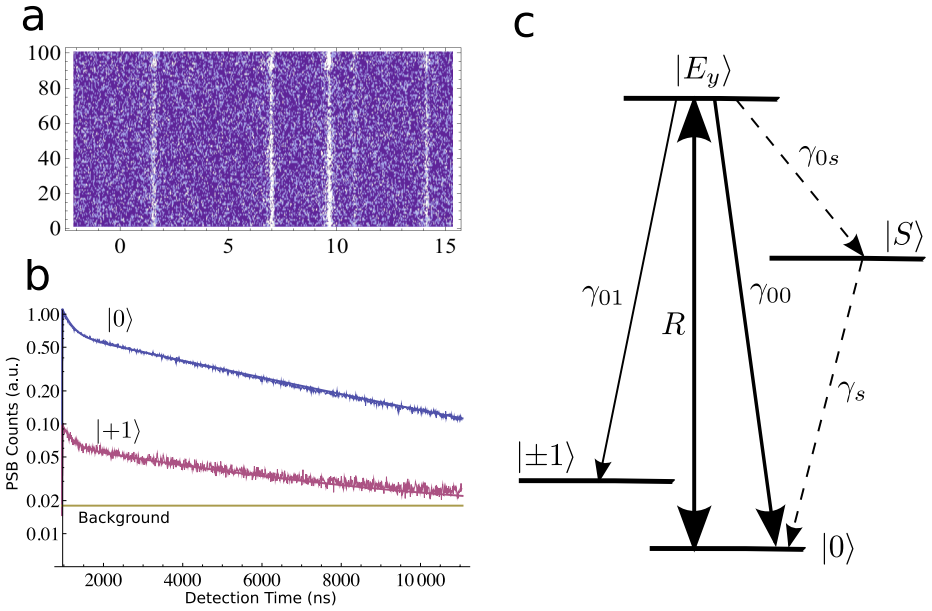

Figure A.3: **Stability and dynamics of optical transitions a** One hundred successive scans of the NV spectrum shown in Figure 3.2(b) of the main text. Each scan taken over ∼10 seconds, demonstrating the spectral stability of the NV center over long time scales. Spectral lines shown here and in Figure 3.2b of the main text have widths larger than 100 MHz due to power broadening. **b** Histograms showing time traces of fluorescence as recorded in the PSB following spin initialization to either the $|0\rangle$ (red) or $|1\rangle$ (blue) state. Solid lines show simulated fluorescence from the NV using the model shown in (c) and described in the text. Two other similar data sets at different laser powers were used to determine the branching ratio of $|E_y\rangle$ to $|\pm1\rangle$ and the spin polarization. **c** Model used to simulate the dynamics of optical transitions leading to fluorescence time traces shown in (b). R gives the optical pumping rate of the readout transition. γ_{00} and γ_{01} are decay rates to the $|0\rangle$ and $|\pm1\rangle$ states, respectively. γ_{0s} and γs are the non-radiative decay rates into and out of the metastable singlet state $|S\rangle$.

a continuous optical pumping of the $|0\rangle \rightarrow |E_y\rangle$ transition at a rate R, starting with some initial spin population for the two cases of initialization in $|0\rangle$ or $|1\rangle$. To estimate the values of γ_{01}, γ_{0s}, R, and the spin polarization, these parameters are varied to fit the simulation to the data by eye. This was done for three different laser powers, and the data and simulation results for the medium power are shown in Figure A.3(b),

which corresponds to conditions under which the Rabi curve in Figure A.3(a) where taken. Using this method, we estimate the branching ratio out of the system of $m_s = 0$ states to be $0.92 \pm 0.16\%$, and the imperfection in spin preparation to be $7.2 \pm 1.8\%$. This imperfection could be either due to incomplete spin polarization or imperfect microwave pulses. The pulse error associated with a square pulse of finite Rabi frequency (around 10 MHz) is estimated to be about 3 %. The error is mostly due to the presence of the hyperfine interaction with the nuclear spin of ^{14}N associated with the NV center[90]. We thus estimate the spin polarization after the green excitation to be $96 \pm 1.9\%$.

To directly calibrate our spin readout results and confirm that it is the imperfect spin preparation stage which reduces the contrast of the Rabi experiment, we perform two experiments in which we polarize the NV center by measurement and perform conditional spin readout. In the first experiment, a π pulse (initialization pulse) resonant to the $|0\rangle \leftrightarrow |E_y\rangle$ transition is applied many lifetimes prior to microwave manipulation. By only analyzing events in which a photon has been detected in the PSB during the initialization pulse, we ensure that a photon has decayed from the $|E_y\rangle$ state prior to microwave manipulation. The state should decay to the $|0\rangle$ state with 99 % probability, and given that the signal / noise of the trigger photon is roughly 280:1, the state should be prepared in $|0\rangle$ with 99 % probability prior to microwave pulses. Subsequent measurement of the spin by a separate laser tuned to the same transition reveals 0.13 ± 0.025 counts /shot if no microwave manipulation is carried out and 0.0092 ± 0.00054 counts/shot if a microwave π pulse is applied resonant to the $|0\rangle \leftrightarrow |+1\rangle$ transition. The ratio of the counts after subtracting the background

of 0.0057 ± 0.0010 counts/shot is accounted for by the expected pulse error. A second experiment was carried out where the initialization pulse was tuned resonant to the $|+1\rangle \leftrightarrow |A_2\rangle$ transition. The detection of a photon in the PSB indicates that the state has been prepared in the $|\pm 1\rangle$ manifold, and a subsequent readout process without any microwave manipulation yields the background level. We then conditionally measure the populations in the $|\pm 1\rangle$ states by individually transferring their population back to $|0\rangle$ state. We find that their population levels are roughly equal (0.059 ± 0.0013 counts/shot and 0.061 ± 0.0014 counts/shot). Assuming that the PSB emission does not change the spin projection, this data indicates that the $|A_2\rangle$ state decays with roughly equal probability to $|\pm 1\rangle$ states.

We note that the readout levels achieved by the conditioned measurement procedure could in principle be different from the values obtained without conditioning. Although the difference is small for the NV center used in the current experiment, we have observed a significant difference for other NV centers. One possible source for this difference is photoionization of the NV^- to NV^0, in which case the center effectively goes dark. The detection of a PSB photon during the conditional calibration procedure described above ensures that the center is in the NV^- state for that particular repetition of the experiment. The readout levels obtained using this procedure are then relevant for normalization of our entanglement verification data, which are similarly conditioned on the detection of a ZPL photon. On the other hand, if no such conditioning was performed, the calibration levels obtained would be reduced by the probability of ionizing the NV, and would not accurately correspond to our entanglement data. In addition, there are many other sources of noise

that would have a similar effect, for example spectral instabilities of the laser - NV center system and mechanical vibrations that quickly misalign the system. These effects are slow compared to the repetition rate of our experiment, but short compared to the total data acquisition time and could generate a difference in the two spin readout methods. The NV center we work with has good long term spectral stability within a linewidth of ∼100 MHz (Figure A.3(a)), and we actively track the position of the NV by maximizing the fluorescence counts during the experiment. However, to completely eliminate the effect of possible instabilities, we normalize our measurements to the conditional calibration values. The population P in state $|0\rangle$ for a given number of counts per repetition (C) is then $P = (C - c_B) / (C_M - c_B)$, where $c_B = 0.0057 \pm 0.0010$ counts/shot and $c_M = 0.11 \pm 0.0022$ counts / shot correspond to the background and maximum calibration values, respectively.

In summary, we find that resonant excitation in combination with conditioning-based spin preparation is an exceptionally useful tool for spin readout of the NV center. Not only can we use it to extract information about populations in relatively few repetitions, but it allows us to fully characterize various procedures related to the spin properties of the NV center, for example spin polarization achieved or pulse errors, with very few assumptions. In addition, the conditioned readout technique may be useful in probing other properties of the NV center such as blinking and spectral stability.

A.4 Verification of polarization selection rules for $|A_2\rangle$ state

Figure 3.2c in Chapter 3 text verifies that transitions from $|\pm 1\rangle$ states to the $|A_2\rangle$ state have mutually orthogonal circular polarizations. Here we explain the observation shown in the figure and describe how we can extract the polarization imperfections of our system.

To obtain Figure 3.2c, the NV center is prepared in the $|+1\rangle$ ($|-1\rangle$) state with a 1 μs polarization step of off-resonant green excitation followed by a microwave π pulse resonant to the $|0\rangle \leftrightarrow |+1\rangle$ ($|0\rangle \leftrightarrow |-1\rangle$) transition. This transfer of population is followed by a short (2 ns) resonant optical excitation pulse tuned to the $|+1\rangle \leftrightarrow |A_2\rangle$ ($|-1\rangle \leftrightarrow |A_2\rangle$) transition. The fluorescence intensity recorded in the PSB in the presence of this excitation pulse is plotted as function of quarter wave plate (QWP) angle. The wave plate rotates the incident linearly polarized light into a well defined superposition of circular polarizations dependent on the angle. The length and intensity of the pulse is chosen such that it is close to an optical π pulse for the appropriate QWP angle that maximizes the fluorescence for the selected transition.

The electric field projections to σ_+ and σ_- after the linearly polarized excitation beam passes the QWP at an angle θ are $\frac{1}{2}\left(i + e^{-2i\theta}\right)$ for σ_+ and $\frac{1}{2}\left(i + e^{2i\theta}\right)$ for σ_-, so that the intensities in σ_+ and σ_- oscillate out of phase as functions of 2θ.

Dynamics of the NV center under excitation by polarized light may be extracted from the simple model shown in Figure A.4. As our excitation beam is tuned to a particular transition, say $|+1\rangle \leftrightarrow |A_2\rangle$, the other transition from $|-1\rangle$ is detuned by

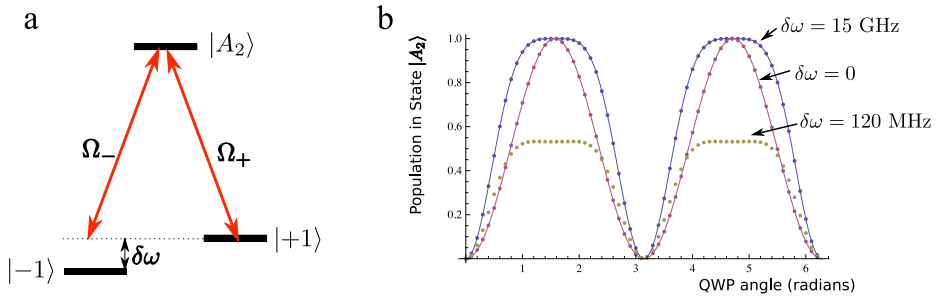

Figure A.4: Model and simulations for verification of circular polarization. **a** Simplified model used to explain the non-sinusoidal behavior. The excited state $|A_2\rangle$ is coupled to the ground states $|\pm1\rangle$ with optical Rabi frequency $\Omega_\pm$. These Rabi frequencies are determined by the particular QWP angle θ. The state prepared with microwave excitation is on-resonance with the optical field while the other is detuned by $\delta\omega$ in the presence of the Zeeman splitting ($2\pi \times 120$ MHz). **b** Calculated excited state populations for $\Omega = \sqrt{\Omega_+^2 + \Omega_-^2} = 2\pi \times 250$ MHz. The pulse is on for 2 ns for the blue and red dots and 3.5 ns for the yellow dots. The detuning is assumed to be 0 for the red dots, 15 GHz for the blue dots and 120 MHz for the yellow dots. Solid lines are plots of expressions for the population in the two limits explained in the text.

the Zeeman splitting $\delta\omega$. The optical Rabi frequencies associated with each transition are QWP angle dependent: $\Omega_+ = \frac{\Omega}{2}\left(i + e^{-2i\theta}\right)$ and $\Omega_- = \frac{\Omega}{2}\left(i + e^{2i\theta}\right)$. We neglect spontaneous decay for simplicity since the optical excitation is relatively short. Our measured signal then corresponds to the population in the $|A_2\rangle$ state after 2 ns ($t = \pi/\Omega$) of evolution under optical excitation from the initial $|+1\rangle$ or $|-1\rangle$ state.

We first consider the limit $\Omega \gg \delta\omega$, where the natural basis is the "bright" and "dark" states defined by $|b\rangle = \frac{\Omega_+|+1\rangle + \Omega_-|-1\rangle}{\Omega}$ and $|d\rangle = \frac{\Omega_+|+1\rangle - \Omega_-|-1\rangle}{\Omega}$. The applied excitation always acts as an optical π pulse that transfers the population from $|b\rangle$ to $|A_2\rangle$. As the QWP rotates, our signal varies with the overlap between the prepared state $|\pm1\rangle$ and the bright state: $|\langle \pm1 | b\rangle|^2 = \frac{1 \pm \sin 2\theta}{2}$. The expected angular dependence is sinusoidal, as demonstrated in Figure A.4

In the opposite limit where $\Omega \ll \delta\omega$, the detuned state is mostly off resonant, and the natural basis is again $|+1\rangle$ and $|-1\rangle$. In this case we may neglect the off resonant level and consider two-level Rabi oscillations between the prepared state and $|A_2\rangle$. The population in the excited state for this case is given by $\sin^2(\Omega_{\pm}t/2) = \sin^2\left(\frac{\pi\sqrt{(1\pm\sin 2\theta)}}{2\sqrt{2}}\right)$. As illustrated in Figure A.4, the population curve has a flattened top compared to a simple sinusoid.

For the NV center considered in the main text, $\Omega \sim 2\pi \times 250$ MHz and $\delta\omega \sim 2\pi \times 122$ MHz. We are thus in the intermediate regime between the two limits. As the QWP is rotated, both the Rabi frequency and the overlap with the bright state change, leading to more complex behavior. The yellow dots in Figure A.4b shows that if t is picked to be slightly longer than a π pulse, the $|A_2\rangle$ population is nearly independent of angle near circular polarization. As the angle deviates from the $\theta = \pi/2$, the Rabi frequency decreases so that the population transferred to the $|A_2\rangle$ state increases. On the other hand, the overlap of the prepared state with the bright state decreases. The combination of these two effects give rise to an extended flat-top behavior.

In addition, Figure 3.2c in the main text shows that the $|+1\rangle$ and $|-1\rangle$ cases give rise to differently shaped curves. We attribute this to different overlap of the confocal spot with the NV for the two measurements, which also explains the slightly different collection efficiencies assumed for the two cases to fit the observed data. The fits used in the figure also include decay from the excited state, which decreases the population transfered to the excited state, but has no other significant effect.

The finite contrast observed in Figure 3.2c could be due to imperfect selection

rules between the $|A_2\rangle$ and ground states or imperfect circular polarization of the optical excitation. With Figure 3.2c alone it is not possible to distinguish between the two cases. Given the above discussion of the excited states, we estimate the mixing between the $|A_2\rangle$ states and other excited states to be about 1 %. From these considerations we deduce that that the selection rules are nearly perfect as described before, but that the imperfect optical system creates a slightly elliptical electric field vector $0.94\,|\sigma_+\rangle + 0.34\,|\sigma_-\rangle$. This ellipticity is expected to decrease the observed fidelity by 12 %.

A.5 Effects of magnetic environment, detunings, and echo

The entangled state given in Eq. 1 of the main text is suceptable to fluctuations from the magnetic enviroment. In this section we show that these fluctations and unaccounted detunings between the microwave fields and NV center transitions would lead to a decreased contrast of the observed oscillations. We then describe the echo technique used to improve the contrast.

We note that these imperfections, in the current context, mainly affect measurements in the H, V basis. Their effect on the $\sigma_\pm$ basis is limited to inefficiencies in population transfer to $|0\rangle$ state and are thus accounted for by pulse errors, which are treated seperately.

A.5.1 Effect of Finite Detuning

We generalize the description given in the main text by introducing the rotating frame associated with the microwave fields:

$$\left|\pm\tilde{1}\right\rangle_t = e^{i\phi_\pm} e^{-i(\omega_\pm \mp \Delta)t} \left|\pm 1\right\rangle ,$$

where we have added a particular detuning Δ that covers the effect of hyperfine coupling to ^{14}N nuclear spin and AC Stark shifts from non-resonant microwave fields. For the NV center used in this study there are no nearby ^{13}C nuclear spins, hence their effect may be neglected. We estimate the static detuning of our microwave field from the relavent NV transtion frequencies to be less then 500 kHz. The two microwave frequencies are well separated by $\delta \sim 120$ MHz, so the presence of the non-resonant field mainly creates an AC Stark shift. For our Rabi frequency of 8 MHz the shift is estimated to be $\Omega^2/\delta \sim 0.5$ MHz. For the idling times considered (~ 500 ns), the effect of the ^{13}C nuclear bath is relatively small.

Under these assumptions, the state right before detection of the photon may then be written as:

$$\left|\Psi(t_d)\right\rangle = \frac{1}{\sqrt{2}} \left(e^{-i\phi_+} e^{i(\omega_+ - \Delta)t_d} \left|\sigma_+\right\rangle \left|-\tilde{1}\right\rangle_{t_d} + e^{-i\phi_-} e^{i(\omega_- + \Delta)t_d} \left|\sigma_-\right\rangle \left|+\tilde{1}\right\rangle_{t_d} \right).$$

Following the detection and idling time t_i, the state becomes:

$$\left|\Psi(t_d)\right\rangle_{t_i} = \frac{1}{\sqrt{2}} \left(e^{-i\phi_+} e^{i(\omega_+ - \Delta)t_d - \Delta t_i} \left|-\tilde{1}\right\rangle_{t_i} \pm e^{-i\phi_-} e^{i(\omega_- + \Delta)t_d + \Delta t_i} \left|+\tilde{1}\right\rangle_{t_i} \right)$$

where $+$ $(-)$ corresponds to detection of a photon in H (V) states. The idling time effects the signal we observe through (re-defining α from the main text):

$$\alpha = (\omega_+ - \omega_- - 2\Delta)t_d + 2\Delta t_i - \Delta\phi$$

For example, the presence of ^{14}N nuclear spin introduces a fixed detuning that is static for the duration of an experimental run, but from run to run changes between $\Delta = 0, \pm 2.2$ MHz [90]. For t_i of order 200 ns the detuning may decrease the observed contrast significantly. While this effect can be reduced by simply waiting for an appropriate rephasing time for the ^{14}N, there is still residual decoherence due to the ^{13}C spin bath. To best eliminate all these effects and extend the memory time of the spin state, we add an echo sequence prior to spin measurement.

A.5.2 Spin Echo Sequence

The echo is easiest to describe in the $|M\rangle = \left(\left|+\tilde{1}\right\rangle + \left|-\tilde{1}\right\rangle\right)/\sqrt{2}$ and $|D\rangle = \left(\left|+\tilde{1}\right\rangle - \left|-\tilde{1}\right\rangle\right)/\sqrt{2}$ basis. We apply a $t_i - 2\pi - t_i$ sequence with microwave pulses that drive the $|M\rangle \leftrightarrow |0\rangle$ transition. This sequence is in spirit similar to the Bang-Bang decoupling technique[148]. For an arbitrary superposition $|\psi\rangle$ of the orthogonal states $|M\rangle$ and $|D\rangle$, evolution of time t_i under the detuning of the form given above leads to coherent oscillations between the states $|D\rangle$ and $|M\rangle$ and results in the state $e^{-i2\Delta t_i \sigma_x}|\psi\rangle$, where σ_i is the appropriate Pauli matrix in the $|M\rangle$, $|D\rangle$ basis. If the magnetic field fluctuates from shot to shot this leads to decoherence. A fast 2π pulse effectively switches the sign of the $|M\rangle$ state ($\sigma_z e^{-i2\Delta t_i \sigma_x}|\psi\rangle$). The subsequent evolution then creates the state $e^{-i2\Delta t_i \sigma_x}\sigma_z e^{-i2\Delta t_i \sigma_x}|\psi\rangle = \sigma_z|\psi\rangle$, which differs from the original state only by a relative phase that is independent of Δt_i.

In the context of section A.5.1, the procedure above results in the following state after the echo sequence in the $\left|\pm\tilde{1}\right\rangle$ basis: $\frac{1}{\sqrt{2}}\left(e^{-i\phi_+}e^{i(\omega_+ - \Delta)t_d}\left|-\tilde{1}\right\rangle \pm e^{i\phi_-}e^{i(\omega_- + \Delta)t_d}\left|-\tilde{1}\right\rangle\right)$. Hence our signal is only affected by the random arrival time of the photon t_d and not

the idling time. For detunings on the order of 5 MHz, the frequency shift is about 4 % of the center frequency of the oscillations (120 MHz) and may be neglected within our current signal to noise.

We note that for a finite length of the 2π pulse (around 110 ns), the echo is expected to be imperfect, as the magnetic field continues to rotate the states in the $|M\rangle$, $|D\rangle$ basis while the pulse is being applied. By timing the echo sequence correctly, we can compensate for this imperfection.

To find the optimal timing of t_i for our experiment, we carry out a simple echo experiment illustrated in Figure A.5. Given Figure A.5b we pick $t_i = 170$ ns for optimum compensation such that an almost perfect echo is performed.

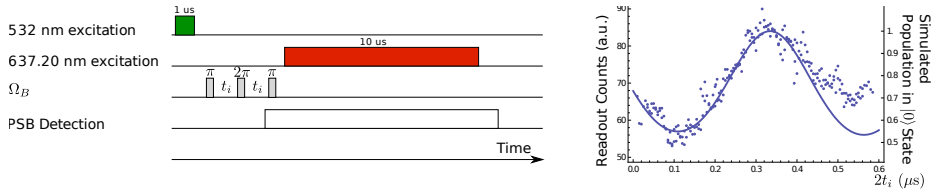

Figure A.5: Echo technique used. **a**. Pulse sequence implemented to test the echo technique. The system is initialized to the $|0\rangle$ state followed by 5 μs of waiting time. A π pulse is applied to create a bright superposition $|M\rangle$ of $|\pm 1\rangle$ states. The state is allowed to evolve for time t_i before a 2π refocusing pulse is applied, after which the state evolves for time t_i again. A π pulse then maps the state back to $|0\rangle$ and is followed by a resonant readout pulse. **b**. Result of the sequence described in part (a). Solid line is a theory fit where only the effect of ^{14}N has been taken into account.

A.6 Fidelity estimates

We would like to determine the lower bound for the entanglement fidelity[30]:

$$F \geq (F_1 + F_2)/2 \tag{A.1}$$

where

$$F_1 = \rho_{\sigma_+ -1,\sigma_+ -1} + \rho_{\sigma_- +1,\sigma_- +1} - 2\sqrt{\rho_{\sigma_+ +1,\sigma_+ +1}\rho_{\sigma_- -1,\sigma_- -1}} \quad (A.2)$$

$$F_2 = \rho_{H+,H+} - \rho_{H-,H-} + \rho_{V-,V-} - \rho_{V+,V+}. \quad (A.3)$$

We obtain $F_1 = 0.83 \pm 0.10$ by measuring the quantities $\rho_{\sigma_+ -1,\sigma_+ -1}$, $\rho_{\sigma_- +1,\sigma_- +1}$, $\rho_{\sigma_+ +1,\sigma_+ +1}$, and $\rho_{\sigma_- -1,\sigma_- -1}$ in the original basis of the photon and spin. F_2 is related to the oscillation amplitudes $a_H/2 = \rho_{H-,H-} - \rho_{H+,H+}$ and $a_V/2 = \rho_{V+,V+} - \rho_{V-,V-}$, measured in the rotated basis.

A.6.1 Time bin optimization

One approach to obtaining the amplitudes a_H and a_V is by directly fitting to the oscillations in the conditional probability, as shown in Figure 3.4c of the main text. The resolution of our time-tagged-single-photon-counting device is 4 ps. However, due to our low count rates, only a fraction of the 4 ps time bins register a photon in the signal region during the entire experimental run. Therefore, to obtain the conditional probability, we group the ZPL counts and their corresponding readout results into larger time bins. One commonly used method is to optimize the goodness of the fit of a particular model to the data by varying size of the bins so that the error of the fit is minimized[149] . However, such a method involves computationally intensive procedures. Therefore we have used a simplified version of this method, motivated by the fact that our count rates decrease exponentially as a function of t_d. In essence, the time bins are determined one at a time starting from the beginning of the decay by minimizing the fit error while varying each successive time bin between 900 ps and 2 ns, which is longer than the timing resolution of our photon detectors

($\sim$ 300 ps) and shorter than the period of the expected oscillations. Since the count rate is highest at the beginning of the decay and should therefore be amenable to the smallest time bins, we start by fixing the first three time bins to 900 ps. We then add the next time bin, vary its length, and perform a fit to the data in these first four bins. The length of the fourth bin is then chosen to minimize the mean squared error of the fit. This optimization process is repeated for each successive time bin until 15 ns of data are used. Such an optimization of the bin sizes is done separately for the H and V polarizations.

We emphasize that the time bins are chosen to optimize the error of the resulting fits, not the amplitude of the fitted oscillations. As shown in Figure 3.4c, the time-binned data exhibit clear oscillations and allows us to extract a fidelity above the classical limit using the fit.

A.6.2 Maximum Likelihood Estimate

Any time binning method, while necessary to present the data in a reasonable fashion, introduces errors by changing the timing information of the raw data. In order to ensure that such errors do not lead to an incorrect estimate of the fidelity, we also extract the fidelity directly from the raw data using a maximum likelihood method. In addition, we calculate the probability distribution for the fidelity, which not only indicates a high probability of entanglement demonstration, but, by virtue of being nearly a perfect Gaussian, justifies minimization of the mean squared error used in the optimization procedure above.

We first derive the formula for the joint probability distribution function of detect-

ing a photon at time t and measuring the spin state $|M\rangle$. Due to the single exponential decay of the optical excited state, the probability distribution for detection of a $|H\rangle$ or $|V\rangle$ photon at time t is

$$p_{H,V}(t) = \frac{1}{\tau} e^{-t/\tau}, \tag{A.4}$$

where $\tau = 12$ ns is the lifetime of the excited states. For a perfect spin-photon entangled state, upon detection of a $|H\rangle$ or $|V\rangle$ photon at time t, the conditional probability of measuring the spin state $|M\rangle$ is $p_{M|H,V}(t) = \frac{1}{2}(1 \pm \cos\alpha(t))$ with $\alpha(t) = (\omega_+ - \omega_-)\, t + (\phi_+ - \phi_-)$. For an imperfect spin photon entangled state, the conditional probability has a reduced oscillation amplitude:

$$p_{M|H,V}(t) = \frac{1}{2}(1 \pm a_{H,V} \cos\alpha(t)). \tag{A.5}$$

Thus, the joint probability is

$$\begin{aligned} p_{M;H,V}(t) &= p_{M|H,V}(t)\, p_{H,V}(t) && \text{(A.6)} \\ &= \frac{1}{2\tau} e^{-t/\tau} \left(1 \pm a_{H,V} \cos\alpha(t)\right). && \text{(A.7)} \end{aligned}$$

Motivated by these considerations we aim to model the experimental data using the following fitting functions:

$$\begin{aligned} f_H(t) &= \frac{c_H}{2} \left(1 + a_H \cos\left(2\pi t/T + \phi\right)\right) e^{-t/\tau} + b_0, && \text{(A.8)} \\ f_V(t) &= \frac{c_V}{2} \left(1 - a_V \cos\left(2\pi t/T + \phi\right)\right) e^{-t/\tau} + b_0, && \text{(A.9)} \end{aligned}$$

with fitting parameters $\{c_H, c_V, a_H, a_V, T, \phi, b_0\}$. Here c_H and c_V are proportional to duration of the experiment and b_0 is the background.

We denote the number of conditional readout events within each $\Delta t = 4$ ps detection time bin $[t, t + \Delta t]$ as $n_{H,t}$ and $n_{V,t}$ for the two photon polarizations, and obtain

the data sets $\{n_{H,t}\}$ and $\{n_{V,t}\}$ with $t = t_0, t_0+\Delta t, t+2\Delta t, \cdots$. For a given set of data and underlying probability model, a maximum likelihood estimate (MLE) picks the values of the model parameters that maximize the *likelihood function* for the data, compared to other choices of parameters. Given no prior knowledge of the fitting parameters, we may assume an uniform distribution for the fitting parameters. Then the likelihood function will be proportional to the probability distribution function. In the following, we use the MLE to fit the theoretical model with experimental data and obtain the oscillation amplitudes a_H and a_V.

The expected average number of events for the time bin $[t, t + \Delta t]$ are given by equations A.8 & A.9 above. However, the number of recorded events for each time bin has fluctuations characterized by the Poisson distribution

$$p_\lambda(n) = \frac{\lambda^n}{n!} e^{-\lambda}, \tag{A.10}$$

where λ is the average number of events. Thus, the *likelihood* for recording $n_{H,t}$ events of detecting an $|H\rangle$ photon at time t and measuring the NV center in spin state $|M\rangle$ is

$$\begin{aligned} L_H(n_{H,t}, t) &= p_\lambda(n_{H,t})\,|_{\lambda=f_H(t)} && \text{(A.11)} \\ &= \tfrac{f_H(t)^{n_{H,t}}}{n_{H,t}!} e^{-f_H(t)}. && \text{(A.12)} \end{aligned}$$

The likelihood for getting the list $\{n_{H,t}\}$ is

$$L_H(\{n_{H,t}\}) = \prod_t L_H(n_{H,t}, t). \tag{A.13}$$

Similarly, the likelihood for the list $\{n_{V,t}\}$ is

$$L_V(\{n_{V,t}\}) = \prod_t L_V(n_{V,t}, t), \tag{A.14}$$

where

$$L_V\left(n_{V,t},t\right)=\frac{f_V\left(t\right)^{n_{V,t}}}{n_{V,t}!}e^{-f_V(t)}. \tag{A.15}$$

We numerically maximize the following likelihood function for both lists $\{n_{H,t}\}$ and $\{n_{V,t}\}$:

$$L\left(\{n_{H,t}\},\{n_{V,t}\}\right)=L_H\left(\{n_{H,t}\}\right)L_V\left(\{n_{V,t}\}\right). \tag{A.16}$$

We use the generic gradient ascend algorithm to maximize the likelihood function with the optimal choice of parameters as listed in Table A.1. We verify that it is also a global maximum by sampling throughout the entire parameter space numerically.

Parameter	a_H	a_V	c_H	c_V	T (ns)	ϕ	b_0
value	0.65	0.55	0.083	0.090	8.2	-4.04	0.000

Table A.1: Optimal choice of parameters from the MLE.

In Figure A.6.2a, we plot the contour of likelihood as a function of a_H and a_V. Since we have no prior knowledge about the parameters a_H and a_V, we can use an uniform prior probability distribution for a_H and a_V. Then the 2D likelihood plot is proportional to the 2D probability distribution P_{a_H,a_V} joint with the observed data.

The marginal probability distribution $P_{a_H+a_V}$ associated with a_H+a_V is the projection of the full distribution to the $+45°$ direction. The marginal probability distribution can be obtained by integrating the 2D probability P_{a_H,a_V} along the $-45°$ direction:

$$P_{a_H+a_V}\left(u\right)\propto\int dvP_{a_H,a_V}\left(\frac{u+v}{2},\frac{u-v}{2}\right). \tag{A.17}$$

Because $F_2=\left(a_H+a_V\right)/2$, we obtain the probability distribution for F_2:

$$P_{F_2}\left(x_1\right)\propto P_{a_H+a_V}\left(2x_1\right). \tag{A.18}$$

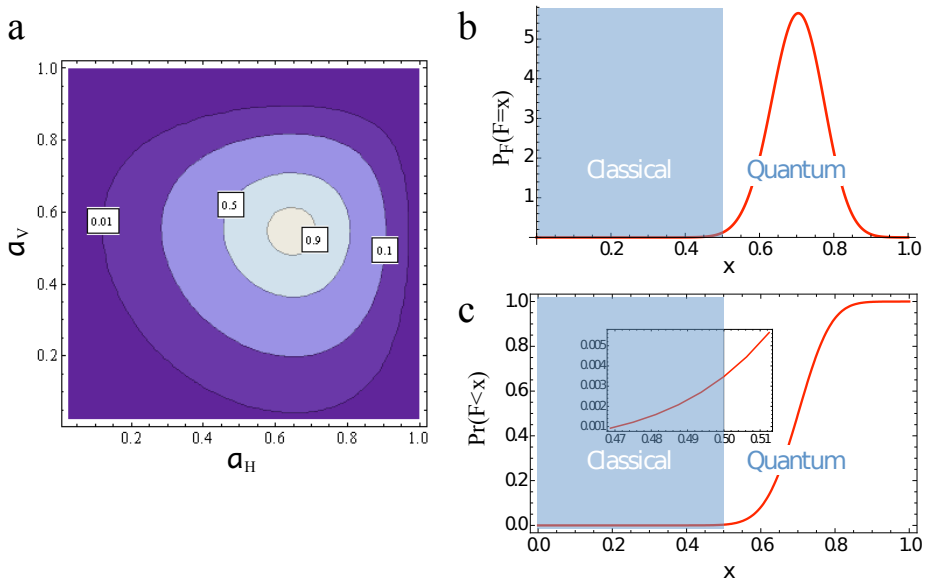

Figure A.6: Results of maximum likelihood estimate. **a.** Contour plot of likelihood as a function of a_H and a_V. The contour lines represent relative likelihood of 90%, 50%, 10%, 1% from inside out. With no prior knowledge of a_H and a_V, the likelihood is proportional to the probability distribution. **b.** The probability distribution for the lower bound on the entanglement fidelity F. **c.** The cumulative probability distribution for the entanglement fidelity F. Inset: A zoomed plot around $F = 0.5$, showing the cumulative probability is only 0.35%.

The probability distribution for the lower bound on the fidelity is a convolution of $P_{F_1}(x)$ and $P_{F_2}(x)$:

$$P_F(F = x) = \int_{-\infty}^{+\infty} dx_1 P_{F_1}(x_1) P_{F_2}(x - x_1), \tag{A.19}$$

where P_{F_1} is assumed to be a Gaussian probability distribution for F_1 with mean 0.83 and standard deviation 0.10. We find that the distribution $P_F(x)$ in Figure A.6.2b is nearly Gaussian and obtain an entanglement fidelity of $F \geq 0.70 \pm 0.070$. The cumulative probability distribution

$$\Pr(F < x) = \int_{-\infty}^{x} dx' P_F(x') \tag{A.20}$$

is shown in Figure A.6.2c and indicates that the probability that the entanglement fidelity is above the quantum threshold of 0.5 is

$$\Pr\left(F > 0.5\right) = 99.7\%. \tag{A.21}$$

These results confirm that our experiment provides a reliable observation of spin-photon entanglement.

Appendix B

Supporting material for Chapter 5

B.1 Experimental details

B.1.1 Sample description

The diamond sample used was a natural, high purity, type IIa diamond with a $\langle 111 \rangle$ cut kept at $\sim$ 7 K. Within this sample, we used three separate NV centers for the data presented in Chapter 5 and this appendix. A first NV center (NVa) is subject to a relatively low strain and has a narrow distribution of ^{13}C states. A second, higher strain NV center (NVb) has a broader distribution of ^{13}C states. All experiments on optical cooling and conditional preparation were repeated with both of these NV centers with consistent results. Figures 5.1, 5.2 and 5.4e and Fig. B.3 present measurements for NVa. The remaining figures in Chapter 5 and this appendix excluding Fig. B.5 present measurements on NVb. An additional NV (NVc) was used for ESR measurements in section 5 of this appendix, which was used to calibrate the

ground state strain for other NV centers by assuming that it is proportional to the strain measured in the excited state[56].

B.1.2 Experimental setup

Our experimental setup is similar to that described earlier [122], with several modifications. First, the three excitation lasers addressing the $|A_1\rangle, |A_2\rangle$, and $|E_y\rangle$ states are kept within a "rough" beatnote lock (3 dB width $\sim$ 5 MHz) relative to each other. The master laser, driving the $|A_1\rangle$ transition, is allowed to "float" freely. Its frequency relative to the NV is monitored through fluorescence counts and adjusted manually every few minutes. The beatnote lock is achieved by feeding the beatnote of the relevant pair of lasers to a commercial PLL board (Analog Devices ADF4007) which converts the beatnote to an error signal. This signal is fed into a commercial FPGA based reconfigurable data acquisition board (National Instruments NI-7833R). The FPGA is programmed to act as a PI controller, and its outputs are fed into the current and cavity inputs of the lasers.

To apply an external magnetic field along the $\langle 111 \rangle$ direction a solenoid was placed outside our cryostat. The cryostat significantly alters the magnetic field at the location of the NV from the applied field. We compensate for this effect of the solenoid – cryostat system by characterizing its frequency response using the NV electron spin as a local magnetometer. We then apply the magnetic field waveform that compensates for the linear response of the setup, so that the desired time varying magnetic field is generated at the NV.

B.1.3 Effects of ionization and other forms of spectral drift

We have already touched on the effects of ionization in Chapter 2. Here we provide the details of the experimental sequence used to obtain the data presented in Chapter 2.

Under continuous resonant excitation the NV center ionizes with a timescale that depends on the laser power [92]. For example, with 50 nW of power on the A_1 laser and 1μW of power on the E_y laser, we measure an ionization timescale of $\sim$ 29 ms (Fig. B.1). The ionization feature is present regardless of whether the data is taken within or outside a CPT dip. This effect complicates comparison of data taken with different laser power or durations, decreases the observed contrast of CPT resonances, prevents the accurate extraction of other timescales, etc. To eliminate the influence of this effect, we perform all of our measurements except those shown in Fig. 1 with a step at the end of each run of the sequence to verify that the NV has not ionized. To do this we turn on the A_1, A_2 and E_y lasers simultaneously for $\sim$ 1 ms. With all three lasers present there is no dark state, and the NV should produce a large number of counts if it is not ionized, and zero photons if it is. We then discard data from runs that do not pass a threshold for the number of collected verification photons. The effect of this post-selection process is shown in Fig. B.1. We note that this process not only selects for unionized cases, but also for accurate positioning of the NV and tuning of the laser frequency. This could lead to the slight rise in counts seen in the post-selected cases, where the NV is relatively dark at the beginning and becomes brighter by the time of the verification step.

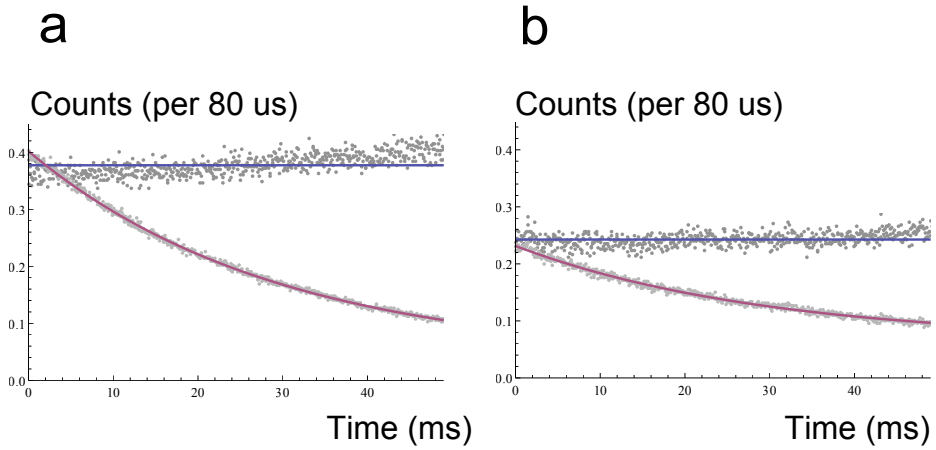

Figure B.1: Average count rates under continuous A_1 and E_y excitation at two different fixed magnetic field with (blue) and without (red) post-selection for ionization. **(a)** Out of CPT resonance, decay timescale is 29.1 ± 0.3 ms without verification. **(b)** In CPT resonance, decay timescale is 29.4 ± 0.6 ms without verification.

B.2 Multilevel description of the NV center

In order to understand the dynamics of our system including the effects of the recycling transition, we model its behavior using a full master equation approach. For simplicity, we neglect the $|E_x\rangle$ and $|E_{1,2}\rangle$ states as they are detuned from all driving fields. The resulting level structure and transitions are shown in Figure B.2.

In addition to all processes shown in the diagram, we include pure dephasing in the excited state at a rate Γ. For resonant excitation of, say, the $|A_1\rangle$ state, the off-resonant excitation of the $|A_2\rangle$ state does not play a significant role most of the time as it is far detuned. We will neglect the effects of far detuned states for the current discussion. We will find, though, that for understanding the ^{14}N polarization behavior these off-resonant excitations play a crucial role and its effects will be included in Section 4 describing the ^{14}N polarization. As described in section B.5, we

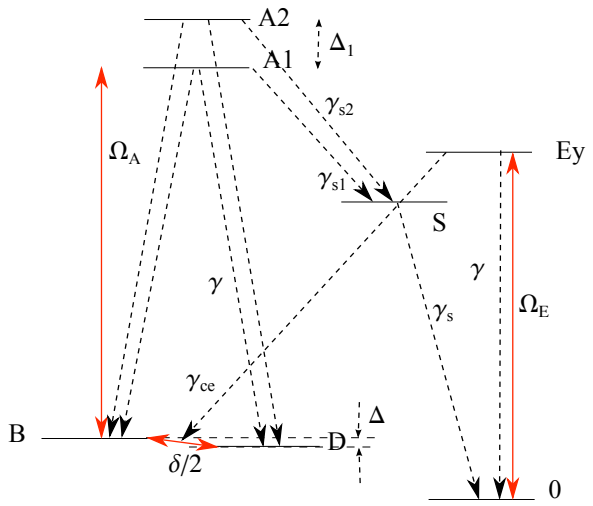

Figure B.2: Simplified level structure of NV center. $|B\rangle$ and $|D\rangle$ are the bright and dark states for a laser Ω_A coupled resonantly to either the $|A_1\rangle$ or $|A_2\rangle$ state. δ is the Zeeman splitting between $|\pm 1\rangle$ states, such that $\delta/2$ is the effective Rabi frequency between between $|B\rangle$ and $|D\rangle$. Δ is the strain splitting in the ground state, and Δ_1 is the energy splitting between $|A_1\rangle$ and $|A_2\rangle$ states. The $|E_y\rangle$ state is addressed by a laser Ω_E and decays into the $|\pm 1\rangle$ states with a total rate γ_{ce}, while the direct decay rate back to the $|0\rangle$ state is γ. The $|A_1\rangle$ ($|A_2\rangle$) state decays to the singlet $|S\rangle$ with rate γ_{s1} (γ_{s2}), which then decays to $|0\rangle$ with rate γ_s.

will assume an appropriate alignment of the $A_{1,2}$ laser polarization relative to the strain axis. We construct equations describing the evolution of the density matrix elements $d\vec{\rho}/dt = M\vec{\rho}$, where M is the evolution matrix including the Liouvillian operators for various decay and dephasing processes (defined in Figure B.2) as well as Hamiltonian operators. Below we describe results showing the steady state of the system of equations.

Since the $|A_1\rangle$ state corresponds to an open Λ system with $\gamma_{ce} \ll \gamma_{s1}$, we expect essentially all of the excited state population to be in (and all the fluorescence to be from) the E_y state. We can obtain an analytical solution for this population in the following form:

$$P_{E_y} = \rho_{E_y,\,E_y} = \frac{c_0\delta^2}{c_1\delta^4 + c_2\delta^2 + c_3} \tag{B.1}$$

where

$$\begin{aligned}
c_0 &= 2\gamma_s\gamma_{s1}(\gamma + 2\Gamma)\Omega_A^2\Omega_E^2, \\
c_1 &= \gamma\gamma_{ce}\gamma_s\Omega_E^2, \\
c_2 &= \frac{1}{2}\gamma\gamma_s\gamma_{s1}(\gamma + 2\Gamma)^2\Omega_A^2 + \gamma\gamma_s\gamma_{ce}(\gamma + 2\Gamma)^2\Omega_E^2 + 2\gamma\gamma_s\gamma_{ce}\Delta^2\Omega_E^2 + \\
&\quad 2[4\gamma_s\gamma_{ce}\Gamma + \gamma_{ce}(\gamma_s + \gamma_{s1})(\gamma + 2\Gamma) + 2\gamma_s\gamma_{s1}(\gamma + 2\Gamma)]\Omega_A^2\Omega_E^2 \\
c_3 &= \gamma\gamma_s\gamma_{ce}[(\gamma + 2\Gamma)^2\Delta^2\Omega_E^2 + \Delta^4\Omega_E^2 + 4\Delta^2\Omega_A^2\Omega_E^2 + 4\Omega_A^4\Omega_E^2]
\end{aligned}$$

Assuming δ, Δ, and $\Omega_A \ll \gamma + 2\Gamma$, we can drop the second and third terms in c_3, the third term in c_2, and ignore the fourth order term in δ. In addition, since $\gamma_{ce} \ll \gamma_{s1}$, the last term in c_2 is approximately just $4\gamma_s\gamma_{s1}(\gamma + 2\Gamma)\Omega_A^2\Omega_E^2$. As a result we find

$$P_{E_y} = A\frac{\delta^2}{\delta^2 + \delta_0^2} \tag{B.2}$$

where the amplitude is given by

$$A = \frac{1}{2 + \frac{\gamma(\gamma+2\Gamma)}{4\Omega_E^2} + \frac{\gamma(\gamma+2\Gamma)}{4\Omega_A^2}\frac{2\gamma_{ce}}{\gamma_{s1}}} = \frac{1}{2 + \frac{\gamma}{R_{Ey}} + \eta\frac{\gamma}{R_{A1}}} \tag{B.3}$$

and the width (HWHM) is given by

$$\delta_0^2 = \frac{\Delta^2 + \frac{4\Omega_A^4}{(\gamma+2\Gamma)^2}}{1 + \frac{\gamma_{s1}\Omega_A^2}{2\gamma_{ce}\Omega_E^2} + \frac{4\gamma_{s1}\Omega_A^2}{\gamma_{ce}\gamma(\gamma+2\Gamma)}} = \frac{\Delta^2 + (R_{A1}/2)^2}{1 + \frac{1}{\eta}(\frac{R_{A1}}{R_{Ey}} + \frac{2R_{A1}}{\gamma})} \tag{B.4}$$

Here $R_{Ey} = \frac{4\Omega_E^2}{\gamma+2\Gamma}$, $R_{A1} = \frac{4\Omega_A^2}{\gamma+2\Gamma}$ are the optical pumping rates for lasers tuned to $|A_1\rangle$ and $|E_y\rangle$, and $\eta = \frac{2\gamma_{ce}}{\gamma_{s1}}$.

For the case of the $|A_2\rangle$ state, equation B.4 is inaccurate because γ_{ce} is on the same order as γ_{s1}. In this case the main difference is that we cannot simplify the last term of c_2, and we use instead the full expression for the width given by

$$\delta_0^2 = \frac{\Delta^2 + (R_{A2}/2)^2}{1 + \frac{R_{A2}}{\eta R_{Ey}} + (\frac{2\Gamma}{\gamma+2\Gamma} + \frac{\gamma_s+\gamma_{s2}}{2\gamma_s} + \frac{2}{\eta})\frac{R_{A2}}{\gamma}} \tag{B.5}$$

In addition to δ_0 we can now express other relevant experimental parameters in terms of results of the above model. The following set of equations lists the commonly used parameters in the Chapter 5 and this appendix relevant for A_1 CPT excitation:

$$C = A\epsilon\gamma = \frac{R_A\epsilon/\eta}{\frac{1}{\eta}\left(\frac{2R_A}{\gamma} + \frac{R_A}{R_E}\right) + 1} \tag{B.6}$$

$$\delta_0 = \sqrt{\frac{\Delta^2 + (R_A/2)^2}{1 + \frac{1}{\eta}\left(\frac{R_A}{R_E} + \frac{2R_A}{\gamma}\right)}} \tag{B.7}$$

$$\delta_c = \sqrt{\ln 2}\sqrt{\frac{\delta_0^2}{CT_{\text{cond}}}} = \sqrt{\ln 2}\sqrt{\frac{\eta}{\epsilon}\frac{\Delta^2 + (R_A/2)^2}{R_A T_{\text{cond}}}} \tag{B.8}$$

where ϵ is the collection efficiency roughly 5×10^{-4} for our setup.

We note that δ_0 approaches Δ as R_A goes to 0 and has a minimum minimum at $R_A = \frac{-R_E\gamma\eta + \sqrt{4(2R_E+\gamma)^2\Delta^2 + R_E^2\gamma^2 + \eta^2}}{2R_E+\gamma}$. For a certain range of experiment parameters the minimum value of δ_0 can be significantly less than Δ.

For example, to compare these results with the CPT width using the $|A_1\rangle$ state shown in Figure 5.1, we convolve the Lorentzian CPT lineshape with a Gaussian ^{13}C distribution with FWHM given by w_0. The resulting Voigt profile [150] has a FWHM of $w' \approx 0.5346(2\delta_0) + \sqrt{w_0^2 + 0.2166(2\delta_0)^2}$. Similarly, the CPT width using using the $|A_2\rangle$ was determined using Eq. B.5. Note that the only fitting parameters used for both sets of data are w_0 and the conversion factor between optical power and optical pumping rate. We determine all relevant decay rates through an independent measurement described in the next section.

B.3 Measurement of branching ratios

As shown in the previous section, the behavior of our CPT system depends on the branching ratios between various states of the NV center. We have examined a technique to measure the branching ratios for an NV center in Chapter 2. We reproduce the figure from Chapter 2 here for completeness, and note that it was measured with NVa, and quote the branching ratios extracted.

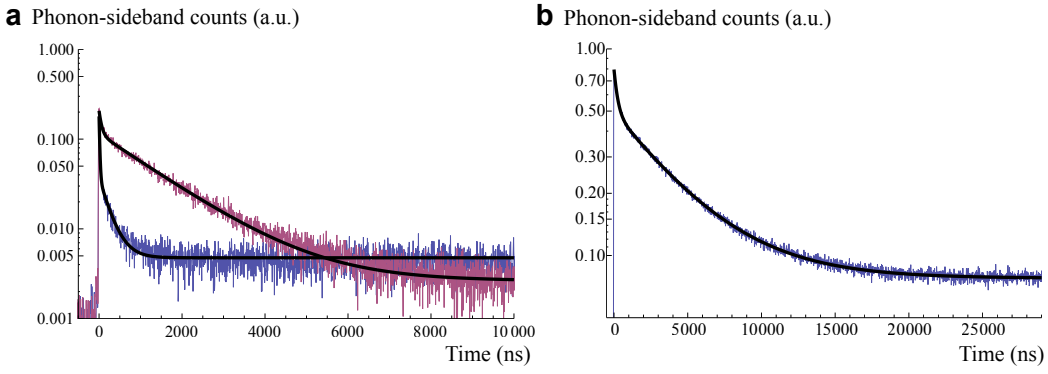

Figure B.3: Fluorescence decay of **(a)** $|A_1\rangle$ (blue), $|A_2\rangle$ (red), and **(b)** $|E_y\rangle$ states with fits to double exponential decays (black lines).

For the $|A_1\rangle$ and $|A_2\rangle$ states, we find the decay rates into $|0\rangle$ to be $\gamma_{s1} \sim 1.6\gamma$ and $\gamma_{s2} \sim 130\gamma$, where γ is the direct decay rate back into the ground state. For the $|E_y\rangle$ state, we find that $\gamma/\gamma_{ce} \sim 105$.

B.4 ^{14}N polarization via optical pumping and measurement based preparation

B.4.1 Optical Pumping

We now use our description of the open CPT system to model optical cooling of the ^{14}N nuclear states. The nuclear spin dynamics of interest are governed by the flip-flop interaction between the nuclear and the electronic spin in the electronic excited state [77, 151]. We note that this rate is slow compared to electronic dynamics, therefore we will assume the electronic state reaches steady state instantaneously within the nuclear diffusion time. For our model we will take the transition rates between different nuclear spin states to be proportional to the steady state excited state population of the electron spin for the corresponding Overhauser field created by the ^{14}N and the externally applied field. In accordance with our experiment (Fig. 2 of main text), we will set the applied magnetic field to the center of the three ^{14}N CPT resonances such that the $m_I = 0$ state forms the dark (or trapping) state. The excitation rate out of the dark state is expected to be small compared to the rate in from other nuclear states. The final polarization that can be reached will be determined by the steady-state solution to the nuclear state populations.

First, note that we work with R_{Ey} near saturation, so equation B.2 can be sim-

plified as

$$P_{E_y}(\delta) = \frac{\delta^2}{(2+\frac{\eta\gamma}{R_{A1}})(\delta^2+\frac{\Delta^2+(R_{A1}/2)^2}{(1+\frac{2R}{\eta\gamma})})} = \frac{R'(\delta)}{2R'(\delta)+\eta\gamma} \tag{B.9}$$

where $R'(\delta) = \delta^2 R_{A1}/(\delta^2+\Delta^2+R_{A1}^2/4)$ is the effective rate out of the dark state and into $|A_1\rangle$.

When the ^{14}N spin is in the $m_I = \pm 1$ states, the nuclear spin flip-flop rate, or the rate into $m_I = 0$, is given by $R_{in} = A_{ex} P_{E_y}(\delta_N)$, where A_{ex} is the hyperfine coupling in the excited state, and δ_N=4.4 MHz is the hyperfine splitting in the ground state. On the other hand, there are two contributions to the rate out of the $m_I = 0$ state. The first is due to $\delta_{T_2^*}$, which we define as the average two photon detuning due to interactions with the ^{13}C bath. The second process is off-resonant excitation of the $|A_2\rangle$ state at a rate ξR_{A1}, where $\xi = (\gamma/2+\Gamma)^2/\Delta_1^2$ with Δ_1 being the detuning between $|A_1\rangle$ and $|A_2\rangle$. For the NV center used in our optical pumping experiments, $\gamma/2+\Gamma \sim 100$ MHz and $\Delta_1 \sim 3$ GHz. For small R_{A1}, this off-resonant process contributes as an additional incoherent decay rate out of the dark state given by $\xi R_{A1}/2$, since the $|A_2\rangle$ state decays with probability 1/2 into the bright state, where it is then excited with rate R_{A1}. Note that we are neglecting direct decay out of $|A_2\rangle$ into the $m_s = 0$ states, since $\eta_{A2} \gg \eta_{A1}$. As a result, the modified rate into $|A_1\rangle$ from the dark state for the $m_I = 0$ state is $R'(\delta_{T_2^*}) + \xi R_{A1}/2$, and the rate out of the $m_I = 0$ state is given by

$$R_{out} = A_{ex} \frac{R'(\delta_{T_2^*}) + \xi R_{A1}/2}{2(R'(\delta_{T_2^*}) + \xi R_{A1}/2) + \eta\gamma} \tag{B.10}$$

Finally, the steady state population in $m_I = 0$ is given by $P_0 = R_{in}/(2R_{out} + R_{in})$. We show this result with the experimental data in Figure 5.2d where no fitting parameter has been used.

B.4.2 Details of measurement based preparation

The dynamics associated with the ^{14}N pumping mechanism determines the pulse sequence used for measurement based preparation of the ^{14}N state. Measurement based preparation is carried out via post-selection of events in which zero counts are detected during preparation photon counting time window (τ_{prep} in Fig B.4a). We note that we want to maximize the polarization that is achieved and minimize the experimental run-time needed to verify the obtained polarization.

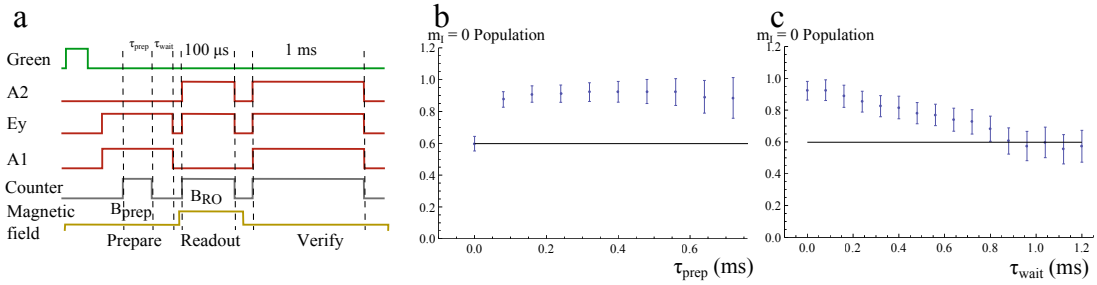

Figure B.4: Measurement based preparation of ^{14}N spin. **(a)** Pulse sequence used in the Chapter 5 where duration of the photon counting window used for preparation (τ_{prep}) and time between the preparation counting window and the end of the preparation laser pulse (τ_{wait}) are indicated. **(b)** Change in prepared population as a function of τ_{prep} for the data presented in Figure 5.2c (red and yellow), $\tau_{\text{wait}} = 0$. Black line indicates the polarization achieved with optical pumping, and no measurement based polarization. All data presented in this figure post-selects for events where zero counts are detected during τ_{prep}. **(c)** Population of $m_I = 0$ as a function of τ_{wait} for $\tau_{\text{prep}} = 480\,\mu$s. Again black line indicates polarization achieved with only with optical pumping.

In presence of photon detection shot noise, increasing the duration of the preparation time window increases the confidence in our estimate of the ^{14}N state and therefore improves the measured spin polarization (see also discussion for ^{13}C environment in methods summary). At the same time for measurement based preparation to be successful, the nuclear state should remain in the dark state during the preparation

window. When the NV is optically excited the ^{14}N is being driven to a steady state with finite polarization. As a result the success probability of post-selection decreases if the preparation time window becomes too long. Both of these effects are illustrated in Figure B.4 b: as the conditioning time increases (τ_{prep}), the observed polarization increases while the decrease in success probability results in larger errorbars. We experimentally found that the 500 μs window used in the Chapter 5 gives the maximum polarization while still maintaining an acceptable signal to noise.

To determine the result of measurement based preparation we record the counts in a time interval at the end of the preparation step. This ensures that the preceding optical cooling does not affect the prepared state and also increases the success probability for finding the ^{14}N in the desired state. By using counts from the last 500 μs of the preparation laser pulse, measurement based preparation of the ^{14}N state yields higher polarization compared to the optical cooling method. This is because we can detect the ^{14}N state faster than the timescale for its evolution under optical excitation ($\tau_1 \sim 350\mu$s). This is further illustrated by Figure B.4c. It shows that optical excitation after initializing the state with measurement based preparation decreases the achieved polarization, and brings it to its steady state value.

B.5 Strain dependence of CPT width

In the absence of a DC magnetic field, the ground state spin properties of the NV center is significantly altered by strain or electric fields around the NV [152, 56]. For example, the zero magnetic field ESR spectrum around $m_I = 0$ shown in Figure B.5 clearly shows a doublet where a single peak with a width of $1/T_2^*$ would be expected.

This observed effect has been explained by the presence of strain terms in the ground state Hamiltonian (following the notation in [56]):

$$H_{\rm gs} = \left(hD_{\rm gs} + d_{\rm gs}^{\parallel}\Pi_z\right) S_z^2 + g\mu_b S_z B_z + d_{gs}^{\perp}\left[\Pi_x\left(S_xS_y + S_yS_x\right) + \Pi_y\left(S_x^2 - S_y^2\right)\right]$$

where $d_{gs}^{\perp}/h = 17 \pm 3$ Hz cm V $^{-1}$ Π_x and Π_y are the components of the strain/electric field vector perpendicular to the NV axis along the molecular axes of the N-V center [152], S_i are the corresponding spin 1 angular momentum operators and h is the Planck's constant, $hD_{\rm gs}$ is the 2.878 GHz zero field splitting and an external magnetic field in the z direction has been assumed, where z direction is parallel to the NV axis. The z component of strain changes the zero field splitting of the NV center and is inconsequential to this work. With $\frac{\Delta}{2} = \sqrt{\Pi_x^2 + \Pi_y^2}d_{gs}^{\perp}$ and $\frac{\Delta}{2}\cos\theta = \Pi_x d_{gs}^{\perp}$ and $\frac{\Delta}{2}\sin\theta = \Pi_y d_{gs}^{\perp}$, we can re-write the effective Hamiltonian for the $|\pm 1\rangle$ states in a very simple form:

$$H_{\rm eff} = \frac{1}{2}\left(\delta\,|+1\rangle\langle+1| - \delta\,|-1\rangle\langle-1| - \Delta i e^{+i\theta}\,|+1\rangle\langle-1| + \Delta i e^{-i\theta}\,|-1\rangle\langle+1|\right)$$

where δ is the two photon detuning as in Section B.2 ($\delta = 2g\mu_b B_z$). For $\delta = 0$, strain fixes the eigenstates to particular superpositions of $|+1\rangle$ and $|-1\rangle$ states, and these eigenstates are split in energy by Δ. As Figure B.5 indicates $\Delta = 170$ kHz for an excited state splitting of 6 GHz (corresponding to NVc). We use this value to calibrate the ground state strain splitting for other NVs[56]. We measured an $|E_x\rangle$ - $|E_y\rangle$ splitting of 3.5 GHz for NVa and 7.5 GHz for NVb corresponding to ground state strain splittings of 100 kHz and 210 kHz respectively.

Since a careful analysis has already been carried out in Section B.2 describing the effects of other levels, here we will concentrate on quantifying the effects of strain on

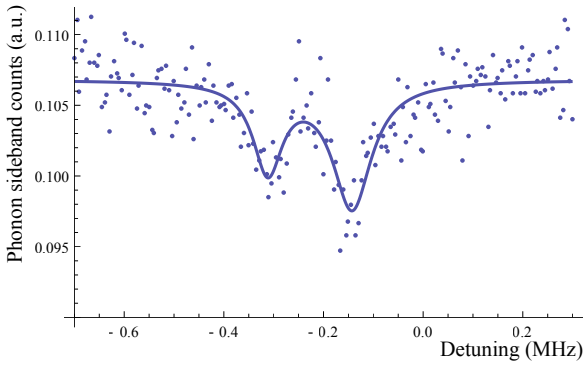

Figure B.5: Measured ESR spectrum for $B \sim 0$ for an NV with an excited state E_x and E_y splitting around 6 GHz. Spectra is measured by first pumping all of the population to the $|0\rangle$ state and then applying a resonant weak microwave pulse of duration 35 μs whose frequency is tuned. The population in the $|0\rangle$ state is measured afterwards using the $|0\rangle$ to $|E_y\rangle$ transition and integrating the counts for a 10 μs window. The zero of the scan range corresponds to 2.878 GHz. The two peaks (fitted with Lorentzians) are separated by 170 $\pm$ 6 kHz and their FWHM widths are 70 $\pm$ 14 kHz (center around -312 kHz) and 94 $\pm$ 14 kHz (center around -142 kHz)

the CPT experiment using a simple model based on the above effective Hamiltonian. The CPT phenomenon can easily be explained in the context of the bright and dark states, so we will use them as the basis states in our model. We optically pump the system into the dark state let it evolve according to the ground state Hamiltonian for time T, followed by a measurement of the population in the bright state. The linear polarization of the CPT laser used for this measurement determines the angle ϕ as the phase between the two circularly polarized components. This phase in turn sets the particular superpositions that form the dark state $|D\rangle = \frac{1}{\sqrt{2}}\left(e^{i\phi}|+1\rangle - e^{-i\phi}|-1\rangle\right)$ and bright state $|B\rangle = \frac{1}{\sqrt{2}}\left(e^{i\phi}|+1\rangle + e^{-i\phi}|-1\rangle\right)$.

Within this model the population in the bright state can be easily calculated:

$$\left|\left\langle B|e^{-iTH_{\text{eff}}}|D\right\rangle_T\right|^2 = \frac{1}{2}\frac{\delta^2 + \Delta^2\cos^2(\theta+2\phi)}{\frac{R^2}{4}+\Delta^2+\delta^2}$$

Where $\langle \cdots \rangle_T$ refers to the average over the classical random variable T[1]. This indicates that the HWHM of the CPT dip is determined by $\sqrt{R^2/4 + \Delta^2}$, as discussed in the Chapter 5. The contrast of the CPT dip is determined by the polarization dependent quantity $\frac{\Delta^2 \cos^2(\theta+2\phi)}{\frac{R^2}{4}+\Delta^2}$. For $R \gg 2\Delta$ good contrast is expected regardless of the polarization of light. For $R \ll 2\Delta$, the polarization of light relative to the strain axis determines the visibility of the CPT dip. This fact is very easy to interpret in two limits. First if $\theta + 2\phi = 0$, no CPT dip is visible at low pumping rates. This special case corresponds to the bright / dark states defined by the light field being equal superpositions of the eigenstates defined by strain. Any prepared dark state quickly precesses in to an equal superposition of dark / bright states before the measurement by the optical field; under these conditions (regardless of the applied magnetic field), no CPT dip is visible. The other extremal case, when $\theta + 2\phi = \pi/2$, corresponds to the bright/states matching the eigenstates defined by strain and therefore having an energy splitting of Δ. In this case a dark state clearly exists for $\delta \ll \Delta$ as there is negligible precession rate out of the dark state.

We re-emphasize that all of the CPT datasets shown have been taken with an optimal linear polarization that maximizes the CPT contrast observed at low powers. Thus in Section B.2 it is assumed that the bright/dark states defined by the light field matches the eigenstates defined by strain.

[1]The average time T is linked to optical pumping rate by: $\langle T \rangle_T = 1/R$, where T is assumed to be an exponentially distributed random variable.

B.6 Autocorrelation measurements and spectral density of signal

Here we present an additional analysis of the autocorrelation results shown in the Chapter 5. To confirm that the observed timescales are indeed due to nuclear dynamics, we performed a control experiment where the fixed magnetic detuning is tuned 4 MHz away from the $m_I = +1$ state. As Figure B.6a illustrates, there is a clear difference in the amplitudes of the features observed between the case when the fixed magnetic field is located at a CPT dip or away from a CPT dip. However the timescales extracted using fits to double exponential decays are quite similar: 350 ± 30 μs and 8400 ± 200 μs for the dataset in a CPT dip and 760 ± 200 μs and 10700 ± 800 μs for the datasets where B is tuned away from the CPT dip. To be able to compare the two datasets easily we have normalized both autocorrelation spectra such that the 0 time delay points are at 1. The 0 time delay point is not shown in the plots because they are purely due to the shot-noise in our detector and the low mean count rate per bin 80 μs[2].

The oscillations observed in the autocorrelation data can be ascribed to harmonics of 60 Hz that is caused by experimental noise. To clearly demonstrate this we show the power spectrum of the two datasets for which the autocorrelations have been

[2]Our signal can be approximated by a random variable that gives us the counts obtained per bin c_n where n is the index of the bin. If shot noise is the only process that determines c_n, then c_n become independent Poissonian random variables with a mean λ determined by the time-bin size, collection efficiency, and the mean excited state population. The zero delay autocorrelation value is given by $\langle \sum_n c_n c_n \rangle = \sum_n \langle c_n^2 \rangle = \sum_n \left(\lambda^2 + \lambda\right)$ while for any other delay j the autocorrelation is given by $\langle \sum_n c_n c_{n-j} \rangle = \sum_n \langle c_n \rangle \langle c_{n-j} \rangle = \sum_n \lambda^2$. Since our count rate is relatively low such that $\lambda \leq 1$, the zero-delay point in autocorrelation is significantly higher compared to the rest of the values.

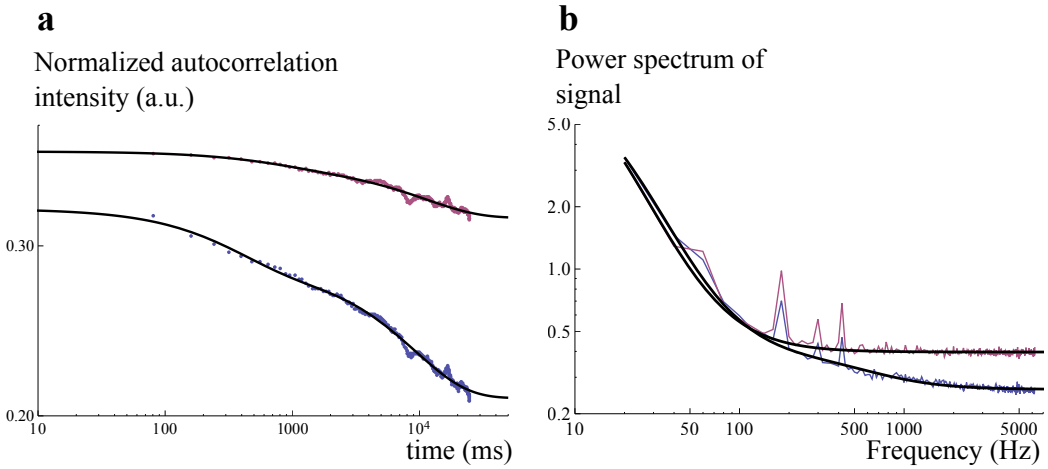

Figure B.6: Spectral and statistical properties of the observed CPT signal at a constant external magnetic field. **(a)** Autocorrelation of the intensity for two constant magnetic fields in a log-log scale when the external magnetic field is tuned away from CPT resonance (red) and when the external field is tuned to be 0.3 MHz away from the center of the $m_I = +1$ resonance (blue), as explained in Chapter 5. **(b)** Power spectrum of the same signal in a log-log scale clearly showing the harmonics of 60 Hz lines and the difference of the off-resonance (red) and on-resonance (blue) for both low frequencies and for high frequencies.

shown. As Figure B.6b illustrates, there are clear peaks at odd harmonics of the AC line frequency of 60 Hz (180 Hz, 300 Hz, 420 Hz), and these features are present for both datasets regardless of whether or not the external magnetic field is tuned to be within a CPT dip. This clearly shows that the observed 60 Hz is not magnetic in character, hence our results are not affected by the magnetic environment of the room (which is dominated by 60 Hz noise).

We note that the power-spectrum within the CPT resonance is well described by a sum of two lorentzians (with timescales given by 258 $\pm$ 12 μs and 9800 $\pm$ 150 μs). Since the power spectrum of the noise and autocorrelation functions are linked by Fourier transform, this justifies the use of double exponential decays as a model for

the autocorrelation function.

The two timescales associated with the CPT dip are tentatively ascribed to processes associated with the nuclear spin environment. The fast time-scale corresponds well with the ^{14}N diffusion timescale (see section 3), and we assign the slower timescale to light induced changes in the carbon nuclear environment. The presence of the two timescales in both datasets, although with very different amplitudes, may be qualitatively explained by the slight sensitivity of our CPT signal to magnetic field fluctuations even away from the CPT resonance.

Even though the 8 ms timescale is long compared to most of our experiments, this value determines the timescale in which a prepared distribution of the Overhauser field remains unchanged under optical illumination and hence is an important factor in determining the utility of the narrowed distribution (see section 10 for an application to magnetic field sensing). We have carried out experiments to verify that this slow timescale is due to reconfiguration of the ^{13}C environment. The results are presented in the next section, where we outline measurements in which the magnetic field is changed quickly under continuous optical illumination.

B.7 Nuclear configuration measurements using fast magnetic field ramps

We examine here in more detail the experiments presented in Figure 5.3b and c where the magnetic field was swept across one of the ^{14}N resonances within a relatively short time period. We now show the complete experimental sequence where

a (forward) rising sweep proceeds the falling sweep that has already been discussed in the Chapter 5. Using both directions of the magnetic field scan, we can extract additional information about the dynamics of the ^{13}C spin bath.

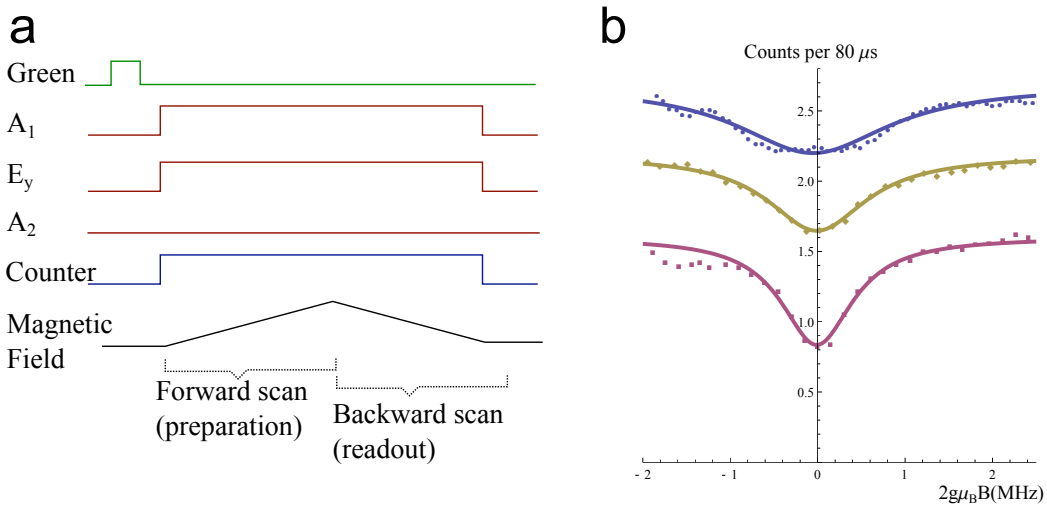

Figure B.7: Observation of the instantaneous configuration of the ^{13}C spin bath. **(a)** Complete pulse sequence for real-time measurement of the ^{13}C nuclear configuration. Counts are recorded in 80 μs time bins. **(b)** Blue: Average of ∼15000 forward scans that passed verification, showing full width of ^{14}N line given by $1/T_2^*$. Red: Average of the same forward scans after shifting each individual run by the center position of their fitted CPT lines. Yellow: Average of the backward scans after shifting each run by the fitted CPT line position of its corresponding forward scan. Blue, and yellow curves have been shifted up for clarity by 1 and 0.5 counts respectively.

First, we can compare the values of our estimate of the Overhauser field between the forward and the backward scans. Figure B.7 shows in blue the average counts obtained during the forward scan. We perform Lorentzian fits to individual forward scans, and consider the fit successful if the parameters for the fitted distribution falls within the averaged CPT line. Specifically if the fitted width is between 20 kHz (frequency sampling interval), and 2 MHz (overall width of the unconditioned CPT width), and the center of the width is within 1.4 MHz of the center of the

unconditioned with the fit considered to be succesfull. The red curve is obtained by shifting (or re-centering) individual forward scans by its corresponding fitted center of the CPT dip if the fit succeeds. Clearly the red curve is a factor of $\sim$2 narrower compared to the average scan. We can further verify that the environment remains in this measured configuration by shifting the backward scan based on the value of the Overhauser field estimated using the preceding forward scan. This then produces the yellow curve which is again a factor of $\sim$1.4 narrower compared to the un-shifted curve. This shows that we are indeed observing instantaneous configurations of the magnetic field environment with a lifetime greater than the single-direction ramp time of 5 ms.

The results of the preceding analysis motivates a method of measuring the timescale of ^{13}C spin bath dynamics by changing the the time of the field ramps and looking at correlations between the position of the CPT resonance on the forward and backward scans. To prepare a particular nuclear spin configuration during the forward scan, we select runs in which the number of counts is zero for two successive time bins corresponding to a particular value of the magnetic field B_0. For the graphs and discussion shown in this section we pick B_0 so the state is prepared at the center of the ^{13}C distribution. The resulting distribution of counts is shown in Figure B.8a. Plotting the averaged counts during the backward scan for these selected runs reveals a narrowed distribution around B_0. By repeating this measurement for increasing ramp times, we see that the features in the post-selected data begins to broaden, indicating decreasing correlations between the Overhauser field during the forward and backward scans as they become further separated in time. We find that the timescale

of this ^{13}C spin bath reconfiguration to be on the order of five milliseconds, consistent with the results of the autocorrelation data in the previous section.

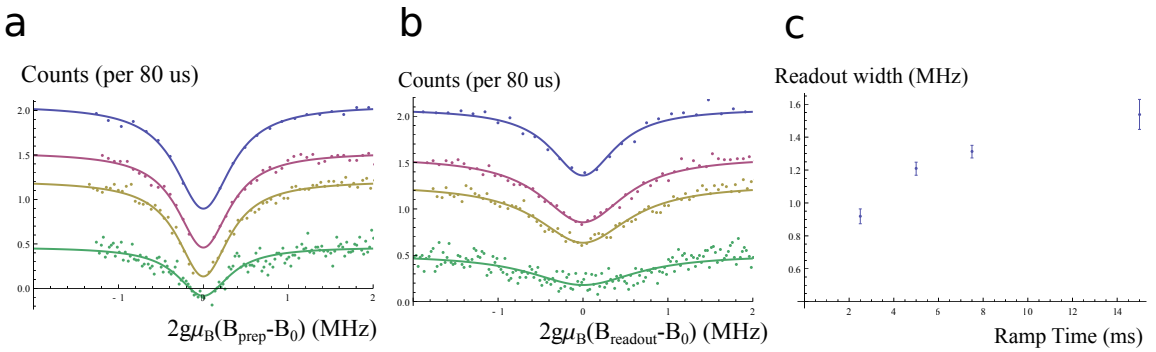

Figure B.8: Analysis of forward and backward scans using the forward scan as preparation and backward scan as readout. **(a)** Distribution of counts in the forward scan if we post-select those runs who have two successive 0 counts around $B_{prep} = B_0$. The selected points (artificially zero) have been dropped from the figure. The times for each ramp direction are 2.5 ms (blue), 5 ms (red), 7.5 ms (yellow) and 15 ms (green). The widths of the fits are roughly the same for all timescales. Blue, red, yellow and green curves have been shifted vertically by 0.2, -0.05, -0.3, -0.55 counts respectively for clarity. **(b)** The corresponding plot of the selected backward scans with the same vertical shifts as in (a). **(c)** Extracted width as a function of the ramp time.

B.8 B_{prep} dependence of the observed width

In this section we will demonstrate that a narrow conditional distribution can be prepared for any value of the two photon detuning that remains within the ^{13}C distribution. However we show that the minimal value of the narrowed width occurs away from the center of the distribution.

To explore this effect we carry out a similar experiment to the one described in Figure 5.4 of the Chapter 5 (and the pulse-sequence reproduced in Figure B.10), where we now vary the external magnetic field B_{prep} during the preparation step

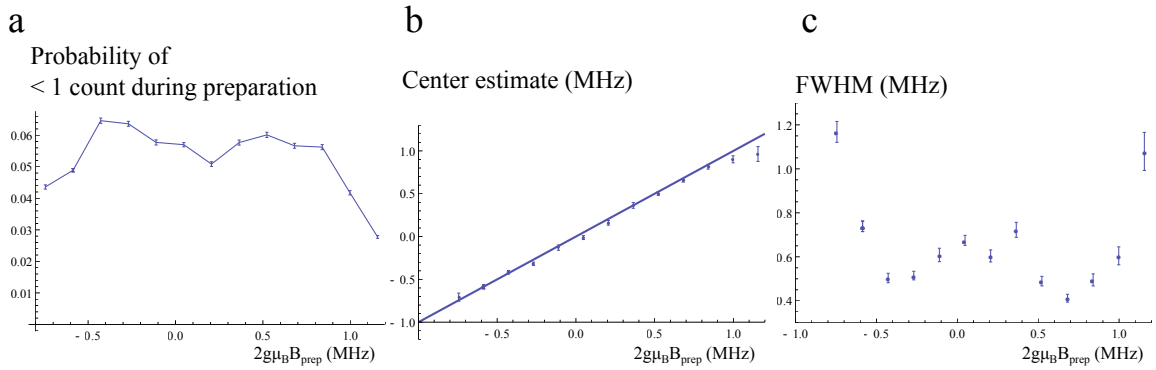

Figure B.9: Dependence of the conditional CPT dip as a function of B_{prep} for NVb. **(a)** Change in the probability of detecting less than 1 count as a function of B_{prep}. **(b)** Center estimate of the conditional distribution as obtained from a single Lorentzian fit. **(c)** Estimate of the width of the conditional distribution as a obtained from a single Lorentzian fit.

and obtain narrowing data for different B_{prep}. The data showing the properties of the narrowed CPT dip is summarized in Figure B.10 for NVb. While B_{prep} remains within the ^{13}C distribution, we are able to prepare a relatively narrow CPT dip. As Figure B.10b illustrates, the center of the narrowed CPT dip follows B_{prep} exactly. As one moves further away from the center of the ^{13}C distribution the probability of being able to prepare the narrowed CPT dip changes. Specifically, far away from the center of the distribution the probability decreases significantly (this is partially illustrated in Figure B.10a), but never decreases to zero. The width of the narrowed distribution also changes as B_{prep} moves away from the center of the ^{13}C distribution. In fact the narrowest feature is found away from the center. Similar results were obtained for another center (NVa).

In our discussions so far we have treated the nuclear environment as a collective system which can be characterized by a density of states. The fact that the center

estimate of the narrowed distribution follows B_{prep} value supports this argument. The variation of the narrowed width as well as the probability of successful state preparation as a function of B_{prep} indicates that a varying density of states may be playing a role in these experiments.

Qualitatively we expect the lifetime of the nuclear environment to be proportional to the density of available states that yield that particular magnetic field value. As the number of ways of escaping from the particular configuration is given by the possible ways in which the nuclear spins can flip-flop between each-other the higher density configurations should have a higher rate of escape. The associated density distribution for the nuclear state of the carbon bath is expected to be peaked at the center, hence we expect the smallest lifetime to be given at the center. With a small lifetime, the prepared state can possibly change before or during the readout stage, yielding a width that is wider compared to the case where the magnetic environment does not change. Even though the lifetime should get longer as we one moves towards the edge of the B distribution, the probability of finding the system in those configurations is also lower. In the presence of false events that produce 0 counts during preparation, the lower probability of finding the environment in the desired state would imply that one should obtain the unprepared distribution for these cases and the width should increase. Based on these qualitative arguments we expect the width to be given by the shape observed in Figure B.10c. We note that this argument could be further studied using the experiment described in Section B.6. Further exploration is needed to determine the exact mechanism of diffusion between different nuclear spin states and its effect on nuclear state preparation.

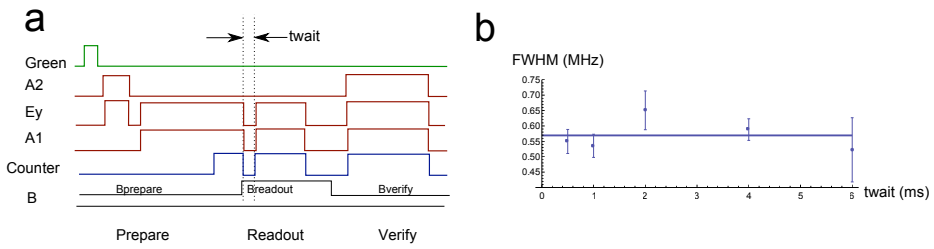

Figure B.10: Change of the conditional CPT width as a function of dark wait time. **(a)** Pulse sequence describing the experiment. The wait time (between the preparation step and the readout step) is varied and a different CPT spectrum is obtained for each point similar to Figure 5.4 in the Chapter 5. Verification step is shown for completeness. **(b)** A plot of the extracted width as a function of the wait time t_{wait} showing no significant change up to 6 ms.

B.9 Lifetime in the absence of optical fields

In our discussions of nuclear dynamics we have neglected any evolution in the absence of optical light fields. We now present data that suggests that lifetime associated with prepared Overhauser field distribution in the dark is much longer than 6 ms.

To probe the effects of evolution in the dark, we repeat the experiment illustrated in Figure 5.4 where we now change the wait time t_{wait} between the preparation and readout. A change in the nuclear environment within this time would affect a change in the width of the CPT signal that we observe in the readout step.

Figure B.10 illustrates the widths of the readout observed as a function of the wait time t_{wait}. No noticeable change in the width occurs within 6 ms of t_{wait}, indicating that if any change occurs within this time its effect on the Overhauser field distribution is negligible for the results that we are reporting.

B.10 Discussion

In this section we apply results of the model developed in Section B.2 to estimate the limits of measurement-based narrowing of Overhauser distribution and discuss possible application of these techniques for magnetometry. In the following $R_E \gg \gamma$ is assumed.

To explore the limits on narrowing given by δ_c we will consider two separate cases. In the first case, applicable to current experimental realization, we assume that preparation is limited by finite strain. The minimum δ_c is achieved by setting $R_A = 4\Delta$ (equation B.8). For this optimal value we find that

$$\delta_c = \sqrt{\frac{2 \ln 2\Delta\eta/\epsilon}{T_{\text{cond}}}}. \tag{B.11}$$

For the current experimental parameters, and $T_{\text{cond}} \sim 8$ ms, we estimate that Overhauser distribution as narrow as 23 kHz and 40 kHz could be prepared for NVa and NVb, respectively. Note that preparation of such a narrow distribution can not verified directly via dark-resonance measurement near zero magnetic field since the readout linewidth itself is limited by strain.

The limit associated with strain could be circumvented by using two-frequency dark resonance excitation in a Raman configuration at high magnetic field ($g_B B \gg \Delta$). In the case of slowly evolving nuclei, R_A and T_{cond} are then the only parameters that define the width of prepared distribution δ_c. To decrease the CPT linewidth, R_A can be made very small, at the cost of reduced number of counts. To ensure that a sufficient number of counts is obtained to differentiate the dark state we require that $CT_{\text{cond}} > 1$, which gives a minimal R_A. Using this minimal R_A, and assuming that

$T_{\rm cond}\gamma\epsilon \gg 2$, we find

$$\delta_c^{min} \simeq \frac{\sqrt{\ln 2}\eta/\epsilon}{2T_{\rm cond}}. \tag{B.12}$$

This analysis thus indicates the present method should allow us to reach Heisenberg limited narrowing $\delta_c^{min} \simeq \frac{1}{T_{\rm cond}}$ with a modest improvement in collection efficiency (from current $\epsilon = 5 \times 10^{-4}$ to $\epsilon = 10^{-2}$). This appears to be well within the reach of current experiments using e.g. solid immersion lenses (SILs) [127]. Note that $T_{\rm cond}$, and correspondingly the narrowing, is eventually limited by the lifetime of prepared nuclear configuration T_1^{nuc} [48].

Finally, we outline how the techniques described in this work can be used for sensing external magnetic fields. As compared with conventional methods involving microwave manipulation and readout with an off-resonant green laser [55], our method can improve the magnetic sensitivity in a number of ways. First of all, we note that use of the presented CPT-based method with a recycling transition results in an improved readout mechanism (gain in sensitivity $\times 6$), along with a gain in sensitivity by employing both $|+1\rangle$ and $|-1\rangle$ states for magnetic field detection (gain in sensitivity $\times\sqrt{2}$). Note that, by improving the collection efficiency by a factor of 10, the increase in the number of counts could boost the sensitivity by an additional factor of three.

Further improvement can obtained via conditional preparation of nuclear environment demonstrated here. Specifically, reduction of the uncertainty in the Overhauser field by setting it to a well-defined value via e.g. feedback control significantly improves the sensitivity to low-frequency magnetic fields. For example, if one operates at high bias fields such that the method is limited by the dynamical evolution of the

nuclear environment, the resultant resonance narrowing could be as much as 1 ms/1μs $\sim 10^3$. When combined with improved readout, the sensitivity to low frequency (DC) magnetic fields could then be potentially improved from about μT Hz$^{-1/2}$ [55] to nT Hz$^{-1/2}$.

Bibliography

[1] J.C. Bergquist, S. R. Jefferts, and D. J. Wineland. Time measurement at the millennium. *Physics Today*, 54:37–42, 2001.

[2] D. N. Matsukevich, P. Maunz, D. L. Moehring, S. Olmschenk, and C. Monroe. Bell inequality violation with two remote atomic qubits. *Phys. Rev. Lett.*, 100:150404, 2008.

[3] M. A. Nielsen and I. L. Chuang. *Quantum Computation and Quantum Information*. Cambridge University Press, 2000.

[4] Serge Haroche and Jean-Michel Raimond. *Exploring the Quantum: Atoms, Cavities, and Photons*. Oxford University Press, 2006.

[5] Claude Cohen-Tannoudji, Jacques Dupont-Roc, and Gilbert Grynberg. *Atom-Photon Interactions: Basic Processes and Applications*. Wiley and Sons, 1998.

[6] Marlan O. Scully and M. Suhail Zubairy. *Quantum Optics*. Cambridge University Press, 1997.

[7] C.E. Wieman, D.E. Pritchard, and D.J. Wineland. Atom cooling, trapping, and quantum manipulation. *Rev. Mod. Phys.*, 71:S253–S262, 1999.

[8] C. Langer, R. Ozeri, J. D. Jost, J. Chiaverini, B. DeMarco, A. Ben-Kish, R. B. Blakestad, J. Britton, D. B. Hume, W. M. Itano, D. Leibfried, R. Reichle, T. Rosenband, T. Schaetz, P. O. Schmidt, and D. J. Wineland. Long-lived qubit memory using atomic ions. *Phys. Rev. Lett.*, 95:060502, 2005.

[9] William D. Phillips. Nobel lecture: Laser cooling and trapping of neutral atoms. *Rev. Mod. Phys*, 70:721741, 1998.

[10] Steven Chu. Nobel lecture: The manipulation of neutral particles. *Rev. Mod. Phys*, 70:685–706, 1998.

[11] Claude N. Cohen-Tannoudji. Nobel lecture: Manipulating atoms with photons. *Rev. Mod. Phys*, 70:707719, 1998.

[12] M.J. Biercuk, J. Britton, H. Uys, A. VanDevender, and J.J. Bollinger. Yocto-newton force detection sensitivity using trapped ions. *Nature Nanotechnology*, 5:646–650, 2010.

[13] C. W. Chou, D. B. Hume, T. Rosenband, and D. J. Wineland. Optical clocks and relativity. *Science*, 5999:1630–1633, 2010.

[14] L.-M. Duan and C. Monroe. Quantum networks with trapped ions. *Rev. Mod. Phys*, 82:1209, 2010.

[15] D. J. Wineland and D. Leibfried. Quantum information processing and metrology with trapped ions. *Laser Phys. Lett.*, 8:175, 2011.

[16] C.A. Sackett, D. Kielpinski, B.E. King, C. Langer, V. Meyer, C.J. Myatt, M. Rowe, Q.A. Turchette, W.M. Itano, D.J. Wineland, and C. Monroe. Experimental entanglement of four particles. *Nature*, 404:256, 2000.

[17] Thomas Monz, Philipp Schindler, Julio T. Barreiro, Michael Chwalla, Daniel Nigg, William A. Coish, Maximilian Harlander, Wolfgang Haensel, Markus Hennrich, and Rainer Blatt. 14-qubit entanglement: creation and coherence. *Phys. Rev. Lett.*, 106:130506, 2011.

[18] L.-M. Duan, B. B. Blinov, D. L. Moehring, and C. Monroe. Scalable trapped ion quantum computation with a probabilistic ion-photon mapping. *Quant. Inf. Comp.*, 4:165, 2004.

[19] D. L. Moehring, P. Maunz, S. Olmschenk, K. C. Younge, D. N. Matsukevich, L.-M. Duan, and C. Monroe. Entanglement of single-atom quantum bits at a distance. *Nature*, 449:68, 2007.

[20] S. Olmschenk, D. N. Matsukevich, P. Maunz, D. Hayes, L.-M. Duan, and C. Monroe. Quantum teleportation between distant matter qubits. *Science*, 323:486, 2009.

[21] A. Safavi-Naini, P. Rabl, P. F. Weck, and H. R. Sadeghpour. Microscopic model of electric-field-noise heating in ion traps. *Phys. Rev. A*, 84:023412, Aug 2011.

[22] Y. Nakamura, Yu. A. Pashkin, and J. S. Tsai. Coherent control of macroscopic quantum states in a single-cooper-pair box. *Nature*, 398:786–788, 1999.

[23] J. A. Schreier, A. A. Houck, Jens Koch, D. I. Schuster, B. R. Johnson, J. M. Chow, J. M. Gambetta, J. Majer, L. Frunzio, M. H. Devoret, S. M. Girvin, , and R. J. Schoelkopf. Suppressing charge noise decoherence in superconducting charge qubits. *Phys. Rev. B*, 77:180502(R), 2008.

[24] Hanhee Paik, D. I. Schuster, Lev S. Bishop, G. Kirchmair, G. Catelani, A. P. Sears, B. R. Johnson, M. J. Reagor, L. Frunzio, L. Glazman, S. M. Girvin, M. H. Devoret, and R. J. Schoelkopf. Observation of high coherence in josephson junction qubits measured in a three-dimensional circuit qed architecture. *arXiv*, quant-ph:1105.4652v4, 2011.

[25] K. De Greve, S. M. Clark, D. Sleiter, K. Sanaka, T. D. Ladd, M. Panfilova, A. Pawlis, K. Lischka, and Y. Yamamoto. Photon antibunching and magnetospectroscopy of a single fluorine donor in znse. *Appl. Phys. Lett.*, 97:241913, 2010.

[26] D. A. Redman, S. Brown, R. H. Sands, and S. C. Rand. Spin dynamics and electronic states of n-v centers in diamond by epr and four-wave-mixing spectroscopy. *Phys. Rev. Lett.*, 67:3420–3423, 1991.

[27] G. Balasubramanian, P. Neumann, D. Twitchen, M. Markham, R. Kolesov, and *et al.* Ultralong spin coherence time in isotopically engineered diamond. *Nature Materials*, 8:383, 2009.

[28] Neil Manson, Lachlan Rogers, Marcus Doherty, and Lloyd Hollenberg. Optically induced spin polarisation of the nv- centre in diamond: role of electron-vibration interaction. *arXiv:1011.2840v1*, 2011.

[29] A. Aspect, P. Grangier, and G. Roger. Experimental realization of einstein-podolsky-rosen-bohm gedankenexperiment: A new violation of bell's inequalities. *Phys. Rev. Lett.*, 49:91, 1982.

[30] B. B. Blinov, D. L. Moehring, L. M Duan, and C. Monroe. Observation of entanglement between a single trapped atom and a single photon. *Nature*, 428:153, 2004.

[31] J. Volz, M. Weber, D. Schlenk, W. Rosenfeld, J. Vrana, K. Saucke, C. Kurtsiefer, and H. Weinfurter. Observation of entanglement of a single photon with a trapped atom. *Phys. Rev. Lett.*, 96:030404, 2006.

[32] T. Wilk, S. C. Webster, and G. Rempe A. Kuhn. Single-atom single-photon quantum interface. *Science*, 317:488–490, 2007.

[33] Z.-S Yuan, Chen Y.-S, B. Zhao, S. Chen, and J. Schmiedmayer. Experimental demonstration of a bdcz quantum repeater node. *Nature*, 454:1098, 2008.

[34] D. Matsukevich, T. Chaneliere, M. Bhattacharya, S.-Y Lan, S. Jenkins, and et al. Entanglement of a photon and a collective atomic excitation. *Phys. Rev. Lett*, 95:040405, 2005.

[35] J. F. Sherson, H. Krauter, R. K. Olsson, B. Julsgaard, K. Hammerer, and et al. Quantum teleportation between light and matter. *Nature*, 443:557, 2006.

[36] C. Cabrillo, J. I. Cirac, P. Garcia-Fernandez, and P. Zoller. Creation of entangled states of distant atoms by interference. *Phys. Rev. A.*, 59:1025, 1999.

[37] C. W. Chou, H. de Riedmatten, D. Felinto andS. V. Polyakov, S. J. van Enk, and *et al.* Measurement-induced entanglement for excitation stored in remote atomic ensembles. *Nature*, 438:828, 2005.

[38] M. O. Scully and K. Druhl. Quantum eraser: A proposed photon correlation experiment concerning observation and "delayed choice" in quantum mechanics. *Phys. Rev. A.*, 25:2208, 1982.

[39] H. J. Kimble. The quantum internet. *Nature*, 453:1023, 2008.

[40] L. Childress, J. M. Taylor, A. S. Sørensen, and M. D. Lukin. Fault-tolerant quantum communication based on solid-state photon emitters. *Phys. Rev. Lett.*, 96(7):070504, Feb 2006.

[41] CK Hong, ZY Ou, and L. Mandel. Measurement of subpicosecond time intervals between two photons by interference. *Phys. Rev. Lett.*, 59(18):2044–2046, 1987.

[42] M. Fleischhauer, A. Imamoglu, and J. P. Marangos. Electromagnetically induced transparency: Optics in coherent media. *Rev. Mod. Phys.*, 77:633, 2005.

[43] A. Aspect, E. Arimondo, R. Kaiser, N. Vansteenkiste, and C. Cohen-Tannoudji. Laser cooling below the one-photon recoil energy by velocity-selective coherent population trapping. *Phys. Rev. Lett.*, 61(7):826–829, Aug 1988.

[44] K.-K. Ni, S. Ospelkaus, M. H. G. de Miranda, A. Pe'er, B. Neyenhuis, J. J. Zirbel, S. Kotochigova, P. S. Julienne, D. S. Jin, and J. Ye. A high phase-space-density gas of polar molecules. *Science*, 322(5899):231–235, 2008.

[45] Marlan O. Scully and Michael Fleischhauer. High-sensitivity magnetometer based on index-enhanced media. *Phys. Rev. Lett.*, 69(9):1360–1363, Aug 1992.

[46] Dmitry Budker and Michael Romalis. Optical magnetometry. *Nature Physics*, 3:227–234, 2007.

[47] J. Vanier. Atomic clocks based on coherent population trapping: a review. *Applied Physics B: Lasers and Optics*, 81:421–442, 2005.

[48] M. Issler, E. M. Kessler, G. Giedke, S. Yelin, I. Cirac, M. D. Lukin, and A. Imamoglu. Nuclear spin cooling using overhauser-field selective coherent population trapping. *Phys. Rev. Lett.*, 105(26):267202, Dec 2010.

[49] Xiadong Xu, Wang Yao, Bo Sun, Duncan G. Steel, Allan S. Bracker, Daniel Gammon, and L. J. Sham. Optically controlled locking of the nuclear field via coherent dark-state spectroscopy. *Nature*, 459:1105–1109, 2009.

[50] Dimitrije Stepanenko, Guido Burkard, Geza Giedke, and Atac Imamoglu. Enhancement of electron spin coherence by optical preparation of nuclear spins. *Phys. Rev. Lett.*, 96(13):136401, Apr 2006.

[51] G. Giedke, J. M. Taylor, D. D'Alessandro, M. D. Lukin, and A. Imamoglu. Quantum measurement of a mesoscopic spin ensemble. *Phys. Rev. A*, 74(3):032316, Sep 2006.

[52] Norman Y. Yao, Liang Jiang, Alexey V. Gorshkov, Peter C. Maurer, Geza Giedke, J. Igancio Cirac, and Mikhail D. Lukin. Scalable architecture for a room temperature solid-state quantum information processor. *arXiv:1012.2864v1*, 2010.

[53] G. Balasubramanian, I. Y. Chan, R. Kolesov, M. Al-Hmoud, J. Tisler, Ch. Shin, Ch. Kim, A. Wjcik, P. R. Hemmer, A. Krueger, T. Hanke, A. Leitenstorfer, R. Bratschitsch, F. Jelezko, and J. Wrachtrup. Nanoscale imaging magnetometery with diamond spins under ambient conditions. *Nature*, 455:648–651, 2008.

[54] Jero Maze, Paul L. Stanwix, J. S. Hodges, S. Hong, J. M. Taylor, P. Cappellaro, L. Jiang, M. V. Gurudev Dutt, E. Togan, A. S. Zibrov, A. Yacoby, R. L. Walsworth, and M. D. Lukin. Nanoscale magnetic sensing with an individual electronic spin in diamond. *Nature*, 455:644–647, 2008.

[55] J. M. Taylor, P. Cappelaro, L. Childress, L. Jiang, D. Budker, P. R. Hemmer, A. Yacoby, R. Walsworht, and M. D. Lukin. High-sensitivity diamond magnetometer with nanoscale resolution. *Nat. Phys.*, 4:810–816, 2008.

[56] F. Dolde, H. Fedder, M. W. Doherty, T. Nobauer, F. Rempp, G. Balasubramanian, T. Wolf, F. Reinhard, L. C. L. Hollenberg, F. Jelezko, and J. Wrachtrup. Electric-field sensing using single diamond spins. *Nature Physics*, 7:459–463, 2011.

[57] Christian Kurtsiefer, Sonja Mayer, Patrick Zarda, and Harald Weinfurter. Stable solid-state source of single photons. *Phys. Rev. Lett.*, 85:290–293, Jul 2000.

[58] Yi-Ren Chang and et al. Mass production and dynamic imaging of fluorescent nanodiamonds. *Nature Nanotechnology*, 3:284–288, 2008.

[59] Wikipedia. Diamond — Wikipedia, the free encyclopedia, 2011. [Online; accessed 23-November-2011].

[60] Element6. Synthetic cvd diamond, 2011. [Online; accessed 23-November-2011].

[61] Julia Tisler, Gopalakrishnan Balasubramanian, Boris Naydenov, Roman Kolesov, Bernhard Grotz, Rolf Reuter, Jean-Paul Boudou, Patrick A. Curmi, Mohamed Sennour, Alain Thorel, Michael Borsch, Kurt Aulenbacher, Rainer Erdmann, Philip R. Hemmer, Fedor Jelezko, and Jorg Wrachtrup. Fluorescence and spin properties of defects in single digit nanodiamonds. *ACS Nano*, 3(7):1959–1965, 2009.

[62] A. M. Zaitsev. *Optical Properties of Diamond: A Data Handbook*. Springer, 2010.

[63] A. Gruber, A. Drbenstedt, C. Tietz, L. Fleury, J. Wrachtrup, and C. von Borczyskowski. Scanning confocal optical microscopy and magnetic resonance on single defect centers. *Science*, 276(5321):2012–2014, 1997.

[64] O. Faklaris, D. Garrot, V. Joshi, J. P. Boudou, T. Sauvage, P. Curmi, and F. Treussart. Comparison of photoluminescence properties of semiconductor quantum dots and non-blinking diamond nanoparticles and observation of the diffusion of diamond nanoparticles in cells. *J. Europ. Opt. Soc. Rap. Public.*, 4:09035, 2009.

[65] Quantum Communcations Victoria. Products, 2011. [Online; accessed 23-November-2011].

[66] Orestis Faklaris, Vandana Joshi, Theano Irinopoulou, Patrick Tauc, Mohamed Sennour, Hugues Girard, Celine Gesset, Jean-Charles Arnault, Alain Thorel, Jean-Paul Boudou, Patrick A. Curmi, and Francois Treussart. Photoluminescent diamond nanoparticles for cell labeling: Study of the uptake mechanism in mammalian cells. *ACS Nano*, 3(12):3955–3962, 2009. PMID: 19863087.

[67] Nitin Mohan, Chao-Sheng Chen, Hsiao-Han Hsieh, Yi-Chun Wu, and Huan-Cheng Chang. In vivo imaging and toxicity assessments of fluorescent nanodiamonds in caenorhabditis elegans. *Nano Letters*, 10(9):3692–3699, 2010.

[68] F. Jelezko, T. Gaebel, I. Popa, A. Gruber, and J. Wrachtrup. Observation of coherent oscillations in a single electron spin. *Phys. Rev. Lett.*, 92:076401, Feb 2004.

[69] P. L. Stanwix, L. M. Pham, J. R. Maze, D. Le Sage, T. K. Yeung, P. Cappellaro, P. R. Hemmer, A. Yacoby, M. D. Lukin, and R. L. Walsworth. Coherence of nitrogen-vacancy electronic spin ensembles in diamond. *Phys. Rev. B*, 82:201201, Nov 2010.

[70] Benjamin Smeltzer, Lilian Childress, and Adam Gali. 13 c hyperfine interactions in the nitrogen-vacancy centre in diamond. *New Journal of Physics*, 13(2):025021, 2011.

[71] A. Gali, M. Fyta, and E. Kaxiras. Ab initio supercell calculations on nitrogen-vacancy center in diamond: Electronic structure and hyperfine tensors. *Phys. Rev. B*, 77:155206, 2008.

[72] M. V. G. Dutt, L. Childress, L. Jiang, E. Togan, J. Maze, F. Jelezko, A. S. Zibrov, P. R. Hemmer, and M. D. Lukin. Quantum register based on individual electronic and nuclear spin qubits in diamond. *Science*, 316:1312–1316, 2007.

[73] G. D. Fuchs, G. Burkard, P. V. Klimov, and D. D. Awschalom. A quantum memory intrinsic to single nitrogenvacancy centres in diamond. *Nature Physics*, 7:789793, 2011.

[74] P. Neumann, N. Mizuochi, F. Rempp, P. Hemmer, H. Watanabe, S. Yamasaki, V. Jacques, T. Gaebel, F. Jelezko, and J. Wrachtrup. Multipartate entanglement among single spins in diamond. *Science*, 320:1326–1329, 2008.

[75] Lucio Robledo, Lilian Childress, Hannes Bernien, Bas Hensen, Paul F. A. Alkemade, and Ronald Hanson. High-fidelity projective read-out of a solid-state spin quantum register. *Nature*, 477:574–578, 2011.

[76] P Neumann, R Kolesov, V Jacques, J Beck, J Tisler, A Batalov, L Rogers, N B Manson, G Balasubramanian, F Jelezko, and J Wrachtrup. Excited-state spectroscopy of single nv defects in diamond using optically detected magnetic resonance. *New Journal of Physics*, 11(1):013017, 2009.

[77] G. D. Fuchs, V. V. Dobrovitski, R. Hanson, A. Batra, C. D. Weis, T. Schenkel, and D. D. Awschalom. Excited-state spectroscopy using single spin manipulation in diamond. *Phys. Rev. Lett.*, 101(11):117601, Sep 2008.

[78] G. Davies and M. F. Hamer. Optical studies of the 1.945 ev vibronic band in diamond. *Proc. R. Soc. Lond. A*, 348(1653):285–298, 1976.

[79] N. B. Manson, J. P. Harrison, and M. J. Sellars. Nitrogen-vacancy center in diamond: Model of the electronic structure and associated dynamics. *Phys. Rev. B*, 74(10):104303, Sep 2006.

[80] Kai-Mei C. Fu, Charles Santori, Paul E. Barclay, Lachlan J. Rogers, Neil B. Manson, and Raymond G. Beausoleil. Observation of the dynamic jahn-teller effect in the excited states of nitrogen-vacancy centers in diamond. *Phys. Rev. Lett.*, 103:256404, Dec 2009.

[81] F. Jelezko, I. Popa, A. Gruber, C. Tietz, J. Wrachtrup, A. Nizovtsev, and S. Kilin. Single spin states in a defect center resolved by optical spectroscopy. *Applied Physics Letters*, 81(12):2160–2162, 2002.

[82] A. Batalov, V. Jacques, F. Kaiesr, P. Siyushev, P. Neumann, L. J. Rogers, R. L. McMurtrie, N. B. Manson, F. Jelezko, and J. Wrachtrup. Low temperature studies of the excited-state structure of negatively charged nitrogen-vacancy color centers in diamond. *Phys. Rev. Lett.*, 102:195506, 2009.

[83] J R Maze, A Gali, E Togan, Y Chu, A Trifonov, E Kaxiras, and M D Lukin. Properties of nitrogen-vacancy centers in diamond: the group theoretic approach. *New Journal of Physics*, 13(2):025025, 2011.

[84] J. Loubser and J. Van Wyk. Electron spin resonance in the study of diamond. *Rep. Prog. Phys.*, 91:1201, 1978.

[85] J. Goss, R. Jones, S. Breuer, P. Briddon, and S. Oberg. The twelve-line 1.682 ev luminescence center in diamond and the vacancy-silicon complex. *Phys. Rev. Lett.*, 77:3041, 1996.

[86] A. Lenef and S. Rand. Electronic structure of the nv center in diamond: Theory. *Phys. Rev. B*, 53:13441, 1996.

[87] L. Rogers, R. McMurtrie, M. Sellars, and N. B. Manson. Time-averaging within the excited state of the nitrogen-vacancy centre in diamond. *New Journal of Physics*, 11:063007, 2009.

[88] A. Batalov, V. Jacques, F. Kaiser, P. Siyushev, P. Neumann, L. J. Rogers, R. L. McMurtrie, N. B. Manson, F. Jelezko, and J. Wrachtrup. Low temperature studies of the excited-state structure of negatively charged nitrogen-vacancy color centers in diamond. *Phys. Rev. Lett.*, 102:195506, May 2009.

[89] F. Kaiser, V. Jacques, A. Batalov, P. Siyushev, F. Jelezko, and *et al.* Polarization properties of single photons emitted by nitrogen-vacancy defect in diamond at low temperature. *Arxiv*, pages quant–ph:0906.3426, 2009.

[90] F. Jelezko and J. Wrachtrup. Quantum information processing in diamond. *J. Phys.: Condens. Matter*, 18:S807–824, 2006.

[91] A. Batalov, C. Zierl, T. Gaebel, P. Neumann, I.-Y. Chan, G. Balasubramanian, P. R. Hemmer, F. Jelezko, and J. Wrachtrup. Temporal coherence of photons emitted by single nitrogen-vacancy defect centers in diamond using optical rabi-oscillations. *Phys. Rev. Lett.*, 100:077401, 2008.

[92] Lucio Robledo, Hannes Bernien, Ilse van Weperen, and Ronald Hanson. Control and coherence of the optical transition of single nitrogen vacancy centers in diamond. *Phys. Rev. Lett.*, 105:177403, Oct 2010.

[93] Ph. Tamarat, T. Gaebel, J. R. Rabeau, M. Khan, A. D. Greentree, H. Wilson, L. C. L. Hollenberg, S. Prawer, P. Hemmer, F. Jelezko, and J. Wrachtrup. Stark shift control of single optical centers in diamond. *Phys. Rev. Lett.*, 97:083002, 2006.

[94] P. Tamarat, N. B. Manson, J. P. Harrison, R. K. McMurtie, A. Nizovtsev, and *et al.* Spin-flip and spin-conserving optical transitions of the nitrogen-vacancy centre in diamond. *New J. Phys*, 10:045004, 2008.

[95] LC Bassett, FJ Heremans, CG Yale, BB Buckley, and DD Awschalom. Electrical tuning of single nitrogen vacancy center optical transitions enhanced by photoinduced fields. *arXiv:1104.3878v1*, 2011.

[96] F. J. Heremans, G. D. Fuchs, C. F. Wang, R. Hanson, and D. D. Awschalom. Generation and transport of photoexcited electrons in single-crystal diamond. *Applied Physics Letters*, 94(15):152102, 2009.

[97] F. Jelezko, A. Volkmer, I. Popa, K. K. Rebane, and J. Wrachtrup. Coherence length of photons from a single quantum system. *Phys. Rev. A*, 67:041802(R), 2003.

[98] T. Gaebel, M. Domhan, C. Wittmann, I. Popa, F. Jelezko, J. Rabeau, A. Greentree, S. Prawer, E. Trajkov, P.R. Hemmer, and J. Wrachtrup. Photochromism in single nitrogen-vacancy defect in diamond. *Applied Physics B: Lasers and Optics*, 82:243–246, 2006. 10.1007/s00340-005-2056-2.

[99] N. B. Manson and J. P. Harrison. Photo-ionization of the nitrogen-vacancy center in diamond. *Diamond and Related Materials*, 14:1705–1710, 2005.

[100] Adam Gali. Theory of the neutral nitrogen-vacancy center in diamond and its application to the realization of a qubit. *Phys. Rev. B*, 79:235210, Jun 2009.

[101] G. Waldherr, J. Beck, M. Steiner, P. Neumann, A. Gali, Th. Frauenheim, F. Jelezko, and J. Wrachtrup. Dark states of single nitrogen-vacancy centers in diamond unraveled by single shot nmr. *Phys. Rev. Lett.*, 106:157601, Apr 2011.

[102] Kyu Young Han, Seong Keun Kim, Christian Eggeling, and Stefan W. Hell. Metastable dark states enable ground state depletion microscopy of nitrogen vacancy centers in diamond with diffraction-unlimited resolution. *Nano Letters*, 10(8):3199–3203, 2010.

[103] L.-M Duan and C. Monroe. Robust quantum information processing with atoms, photons, and atomic ensembles. *Advances in Atomic, Molecular, and Optical Physics*, 55:419–464, 2008.

[104] M. Ansmann, H. Wang, R. C. Bialczak, M. Hofheinz, and E. Lucero *et al.* Violation of bell's inequality in josephson phase qubits. *Nature*, 461:504–506, 2009.

[105] L. DiCarlo, J. M. Chow, J. M. Gambettaand L. S. Bishop, B. R. Johnson, and *et al.* Demonstration of two-qubit algorithms with a superconducting quantum processor. *Nature*, 46:240–244, 2009.

[106] H. de Riedmatten, M. Afzelius, M. U. Staudt, C. Simon, and N. Gisin. A solid-state light-matter interface at the single-photon level. *Nature*, 456:773, 2008.

[107] G. D. Fuchs, V. V. Dobrovitski, D. M. Toyli, F. J. Heremans, and D. D. Awschalom. Gigahertz dynamics of a strongly driven single quantum spin. *Science*, 326:1520, 2009.

[108] N. Manson, J. Harrison, and M. Sellars. Nitrogen-vacancy center in diamond: Model of the electronic structure and associated dynamics. *Phys. Rev. B*, 74:104303, 2006.

[109] C. Santori, Ph. Tamarat, P. Neumann, J. Wrachtrup, D. Fattal, and *et al.* Coherent population trapping of single spins in diamond under optical excitation. *Phys Rev. Lett.*, 97:247401, 2006.

[110] A. Faraon D. Englund, I. Fushman, N. Stoltz, P. Petroff, and *et al.* Controlling cavity reflectivity with a single quantum dot. *Nature*, 450:857–61, 2007.

[111] S. Schietinger, T. Schroder, and O. Benson. One-by-one coupling of single defect centers in nanodiamonds to high-q modes of an optical microresonator. *Nano Letters*, 8:3911, 2008.

[112] C. F. Wang, R. Hanson, D. D. Awschalom, E. L. Hu, T. Feygelson, and *et al.* Fabrication and characterization of two-dimensional photonic crystal microcavities in nanocrystalline diamond. *Appl. Phys. Lett.*, 91:201112, 2007.

[113] Z. Y. Jeff Ou. *Multi-Photon Quantum Interference*. Springer, 2007.

[114] C. Santori, D. Fattal, J. Vučković, G.S. Solomon, and Y. Yamamoto. Indistinguishable photons from a single-photon device. *Nature (London)*, 419(6907):594–597, 2002.

[115] T. Legero, T. Wilk, M. Hennrich, G. Rempe, and A. Kuhn. Quantum beat of two single photons. *Phys. Rev. Lett.*, 93(7):70503, 2004.

[116] A. Kiraz, M. Ehrl, T. Hellerer, ÖE Müstecaplıoğlu, C. Bräuchle, and A. Zumbusch. Indistinguishable photons from a single molecule. *Phys. Rev. Lett.*, 94(22):223602, 2005.

[117] J Beugnon, MPA Jones, J Dingjan, B Darquie, G Messin, A Browaeys, and P Grangier. Quantum interference between two single photons emitted by independently trapped atoms. *Nature (London)*, 440(7085):779–782, APR 6 2006.

[118] P. Maunz, D. L. Moehring, S. Olmschenk, K. C. Younge, D. N. Matsukevich, and C. Monroe. Quantum interference of photon pairs from two remote trapped atomic ions. *Nat. Phys.*, 3(8):538–541, August 2007.

[119] R. Lettow, Y. L. A. Rezus, A. Renn, G. Zumofen, E. Ikonen, S. Götzinger, and V. Sandoghdar. Quantum interference of tunably indistinguishable photons from remote organic molecules. *Phys. Rev. Lett.*, 104(12):123605–, March 2010.

[120] Edward B. Flagg, Andreas Muller, Sergey V. Polyakov, Alex Ling, Alan Migdall, and Glenn S. Solomon. Interference of single photons from two separate semiconductor quantum dots. *Phys. Rev. Lett.*, 104(13):137401–, April 2010.

[121] R.B. Patel, A.J. Bennett, I. Farrer, C.A. Nicoll, D.A. Ritchie, and A.J. Shields. Two-photon interference of the emission from electrically tunable remote quantum dots. *Nature Photon.*, 4(9):632–635, 2010.

[122] E. Togan, Y. Chu, A. S. Trifonov, L. Jiang, J. Maze, L. Childress, M. V. G. Dutt, A. S. Sorensen, P. R. Hemmer, A. S. Zibrov, and M. D. Lukin. Quantum entanglement between an optical photon and a solid-state spin qubit. *Nature*, 466:730–734, 2010.

[123] T.M. Babinec, B.J.M. Hausmann, M. Khan, Y. Zhang, J.R. Maze, P.R. Hemmer, and M. Lončar. A diamond nanowire single-photon source. *Nat. Nanotechnol.*, 5(3):195–199, 2010.

[124] A. Faraon, P.E. Barclay, C. Santori, K.M.C. Fu, and R.G. Beausoleil. Resonant enhancement of the zero-phonon emission from a colour centre in a diamond cavity. *Nature Photon.*, 5(5):301–305, 2011.

[125] Dirk Englund, Brendan Shields, Kelley Rivoire, Fariba Hatami, Jelena Vučković, Hongkun Park, and Mikhail D. Lukin. Deterministic coupling of a single nitrogen vacancy center to a photonic crystal cavity. *Nano. Lett.*, 10(10):3922–3926, September 2010.

[126] Roman Kolesov, Bernhard Grotz, Gopalakrishnan Balasubramanian, Rainer J. Stohr, Aurelien A. L. Nicolet, Philip R. Hemmer, Fedor Jelezko, and Jorg Wrachtrup. Wave-particle duality of single surface plasmon polaritons. *Nat. Phys.*, 5(7):470–474, July 2009.

[127] P. Siyushev, F. Kaiser, V. Jacques, I. Gerhardt, S. Bischof, H. Fedder, J. Dodson, M. Markham, D. Twitchen, F. Jelezko, and J. Wrachtrup. Monolithic diamond optics for single photon detection. *Appl. Phys. Lett.*, 97:241902, 2010.

[128] Hannes Bernien, Lilian Childress, Lucio Robledo, Matthew Markham, Daniel Twitchen, and Ronald Hanson. Two-photon quantum interference from separate nitrogen vacancy centers in diamond. *arXiv:110.3329v1*, 2011.

[129] Igor Aharonovich, Andrew D. Greentree, and Steven Prawer. Diamond photonics. *Nat. Photon.*, 5(7):397–405, July 2011.

[130] P. Neumann, J. Beck, M. Steiner, F. Rempp, H. Fedder, P. R. Hemmer, J. Wrachtrup, and F. Jelezko. Single-shot readout of a single nuclear spin. *Science*, 329:542, 2010.

[131] Charles Santori, Philippe Tamarat, Philipp Neumann, Jörg Wrachtrup, David Fattal, Raymond G. Beausoleil, James Rabeau, Paolo Olivero, Andrew D. Greentree, Steven Prawer, Fedor Jelezko, and Philip Hemmer. Coherent population trapping of single spins in diamond under optical excitation. *Phys. Rev. Lett.*, 97(24):247401, Dec 2006.

[132] B. B. Buckley, G. D. Fuchs, L. C. Bassett, and D. D. Awschalom. Spin-light coherence for single-spin measurement and control in diamond. *Science*, 330(6008):1212–1215, 2010.

[133] D. Klauser, W. A. Coish, and Daniel Loss. Nuclear spin state narrowing via gate-controlled rabi oscillations in a double quantum dot. *Phys. Rev. B*, 73(20):205302, May 2006.

[134] Gang Chen, Doron L. Bergman, and Leon Balents. Semiclassical dynamics and long-time asymptotics of the central-spin problem in a quantum dot. *Phys. Rev. B*, 76(4):045312, Jul 2007.

[135] Francois Bardou, Jen-Philippe Bouchaud, Alain Aspect, and Claude Cohen-Tannoudji. *Levy statistics and laser cooling: How rare events bring atoms to rest*. Cambridge University Press, 2002.

[136] M. S. Rudner, L. M. K. Vandersypen, V. Vuletic, and L. S. Levitov. Generating entanglement and squeezed states of nuclear spins in quantum dots. *arXiv:1101.3370v2*, 2011.

[137] F. Verstraete, M. M. Wolf, and J. I. Cirac. Quantum computation and quantum-state engineering driven by dissipation. *Nature Physics.*, 5:633 – 636, 2009.

[138] L. Jiang, M. V. Gurudev Dutt, E. Togan, L. Childress, P. Cappellaro, J. M. Taylor, and M. D. Lukin. Coherence of an optically illuminated single nuclear spin qubit. *Phys. Rev. Lett.*, 100:073001, Feb 2008.

[139] Jennifer T. Choy, Birgit J. M. Hausmann, Thomas M. Babinec, Irfan Bulu, Mughees Khan, Patrick Maletinsky, Amir Yacoby, and Marko Lonar. Enhanced single-photon emission from a diamondsilver aperture. *Nature Photonics*, page doi:10.1038/nphoton.2011.249, 2011.

[140] Paul E. Barclay, Kai-Mei C. Fu, Charles Santori, Andrei Faraon, and Raymond G. Beausoleil. Hybrid nanocavity resonant enhancement of color center emission in diamond. *Phys. Rev. X*, 1:011007, Sep 2011.

[141] T. van der Sar, J. Hagemeier, W. Pfaff, E. C. Heeres, S. M. Thon, H. Kim, P. M. Petroff, T. H. Oosterkamp, D. Bouwmeester, and R. Hanson. Deterministic nanoassembly of a coupled quantum emitter–photonic crystal cavity system. *Applied Physics Letters*, 98(19):193103, 2011.

[142] Janik Wolters, Andreas W. Schell, Günter Kewes, Nils Nüsse, Max Schoengen, Henning Döscher, Thomas Hannappel, Bernd Löchel, Michael Barth, and Oliver Benson. Enhancement of the zero phonon line emission from a single nitrogen vacancy center in a nanodiamond via coupling to a photonic crystal cavity. *Applied Physics Letters*, 97(14):141108, 2010.

[143] Murray W. McCutcheon and Marko Loncar. Design of a silicon nitride photonic crystal nanocavity with a quality factor of one million for coupling to a diamond nanocrystal. *Opt. Express*, 16(23):19136–19145, Nov 2008.

[144] P Siyushev, V Jacques, I Aharonovich, F Kaiser, T Mller, L Lombez, M Atatre, S Castelletto, S Prawer, F Jelezko, and J Wrachtrup. Low-temperature optical characterization of a near-infrared single-photon emitter in nanodiamonds. *New Journal of Physics*, 11(11):113029, 2009.

[145] Elke Neu, David Steinmetz, Janine Riedrich-Mller, Stefan Gsell, Martin Fischer, Matthias Schreck, and Christoph Becher. Single photon emission from silicon-vacancy colour centres in chemical vapour deposition nano-diamonds on iridium. *New Journal of Physics*, 13(2):025012, 2011.

[146] J. R. Weber, W. F. Koehl, J. B. Varley, A. Janotti, B. B. Buckley, C. G. Van de Walle, and D. D. Awschalom. Quantum computing with defects. *Proceedings of the National Academy of Sciences*, 107(19):8513–8518, 2010.

[147] W. F. Koehl, B. B. Buckley, F. J. Heremans, G. Calusine, and D. D. Awschalom. Room temperature coherent control of defect spin qubits in silicon carbide. *Nature*, 479:84, 2011.

[148] J. J. L. Morton, A. M. Tyryshkin, A. Ardavan, S. C. Benjamin, K. Porfyrakis, and et al. Bang-bang control of fullerene qubits using ultrafast phase gates. *Nature Physics*, 2:40, 2006.

[149] Y. Kanazawa. An optimal variable cell histogram based on the sample spacings. *The Annals of Statistics*, 20:291–304, 1992.

[150] J.J. Olivero and R.L. Longbothum. Empirical fits to the voigt line width: A brief review. *J. Quant. Spectrosc. Radiat. Transfer*, 17:233–236, 1977.

[151] V. Jacques, P. Neumann, J. Beck, M. Markham, D. Twitchen, J. Meijer, F. Keiser, G. Balasubramanian, F. Jelezko, and J. Wrachtrup. Dynamic polarization of single nuclear spins by optical pumping of nitrogen-vacancy color centers in diamond at room temperature. *Phys. Rev. Lett.*, 102:057403, 2009.

[152] E. Vanoort and M. Glasbeek. Electric-field-induced modulation of spin echoes of n-v centers in diamond. *Chem. Phys. Lett.*, 168:529–532, 1990.